Gulf General Atomic
Incorporated

GA-9907

ELECTRON SHIELDING STUDIES

Experimental Program

TECHNICAL SUMMARY REPORT

August 1, 1968 through December 31, 1969

Prepared under
Contract NAS 8-11304
for the
National Aeronautics and Space Administration
George C. Marshall Space Flight Center
Huntsville, Alabama

January 23, 1970

Gulf General Atomic
Incorporated
P.O. Box 608, San Diego, California 92112

GA-9907

ELECTRON SHIELDING STUDIES

Experimental Program

TECHNICAL SUMMARY REPORT

August 1, 1968 through December 31, 1969

Work done by:

D. G. Costello
H. Weber
J. A. Lonergan

Report written by:

D. G. Costello
H. Weber
J. A. Lonergan

During the period of this report the following "reportable items," as defined by Article XII "Reporting of New Technology," evolved:

NONE

Prepared under
Contract NAS 8-11304
for the
National Aeronautics and Space Administration
George C. Marshall Space Flight Center
Huntsville, Alabama

Gulf General Atomic Project 447.1000 January 23, 1970

CONTENTS

ILLUSTRATIONS

ILLUSTRATIONS (Continued)

ILLUSTRATIONS (Continued)

ILLUSTRATIONS (Continued)

ILLUSTRATIONS (Continued)

1. INTRODUCTION

This final report describes the experimental portion of the work performed under Contract NAS8-11304 with the NASA George C. Marshall Space Flight Center in Huntsville, Alabama. The work reported herein was done during the period August 1, 1968 through December 31, 1969. In addition to presenting new information, previously reported results are consolidated here.

This report describes experiments in which the energy spectra of electrons transmitted through slabs of the tin were measured as a function of angle with respect to the incident beam. The incident electron energies were 4.0 and 8.0 MeV; data were obtained for both normal and oblique angles of incidence. The measured results are compared with calculations generated by the ETRAN 15 Monte Carlo program.[1] In addition, a formula has been empirically derived from the data obtained during this experimental program which gives the energy and angular distributions for electrons emerging from a slab of material as a function of incident electron energy.

In the present work, absolute bremsstrahlung energy spectra have been measured as a function of angle from targets of tin of sufficient thickness for the electrons to lose all or a large fraction of their energy in the material. This bremsstrahlung yield is of interest to many areas of applied physics, especially to the area of shielding. Incident electrons of 4.0 and 8.0 MeV were directed normal to the target. The results of these measurements are compared to ETRAN 15 calculations, as well as to the calculations of Dickinson and Lent.[2]

Bremsstrahlung yield measurements have also been made on thin targets of silver and gold; these measurements are compared with those predicted from various bremsstrahlung cross section formulae.

2. EXPERIMENTAL PROCEDURES

2.1 ELECTRON TRANSMISSION MEASUREMENTS

The spectra of electrons transmitted through slabs of tin were measured with electron beams at 4 and 8 MeV. The incident beam energy is established by magnetic analysis in the accelerator area. The beam was bent 36°, passed through a set of slits and bent through another 36° before passing through the target collimators. The slits were adjusted so that the energy spread of the beam was 2 percent. The calibration procedure is described elsewhere.[3]

The experimental setup which was used is shown in Fig. 1. An incident beam of electrons was collimated and directed at a target located at the center of the scattering chamber. The collimator consists of a 1/4-inch hole in a 2-inch-thick graphite block. A lead spray shield with a 3/8-inch-diameter opening was placed behind the collimator to stop electrons scattered by the collimator and to reduce the number of bremsstrahlung photons produced at the collimator that strike the target. As will be discussed later, it was necessary to remove this collimation system during the bremsstrahlung measurements because of a large background.

The electrons that were transmitted through the target were precollimated at a variable angle (θ) to the incident beam with a graphite collimator at the edge of the chamber. The electrons that passed through the opening in a gamma shield were again collimated by 1/4-inch-thick lead plate with a 1/4-inch-diameter opening in front of the electron spectrometer.

Not shown in the figure is the shielding around the detector that reduces background from scattered radiation. Since the final lead

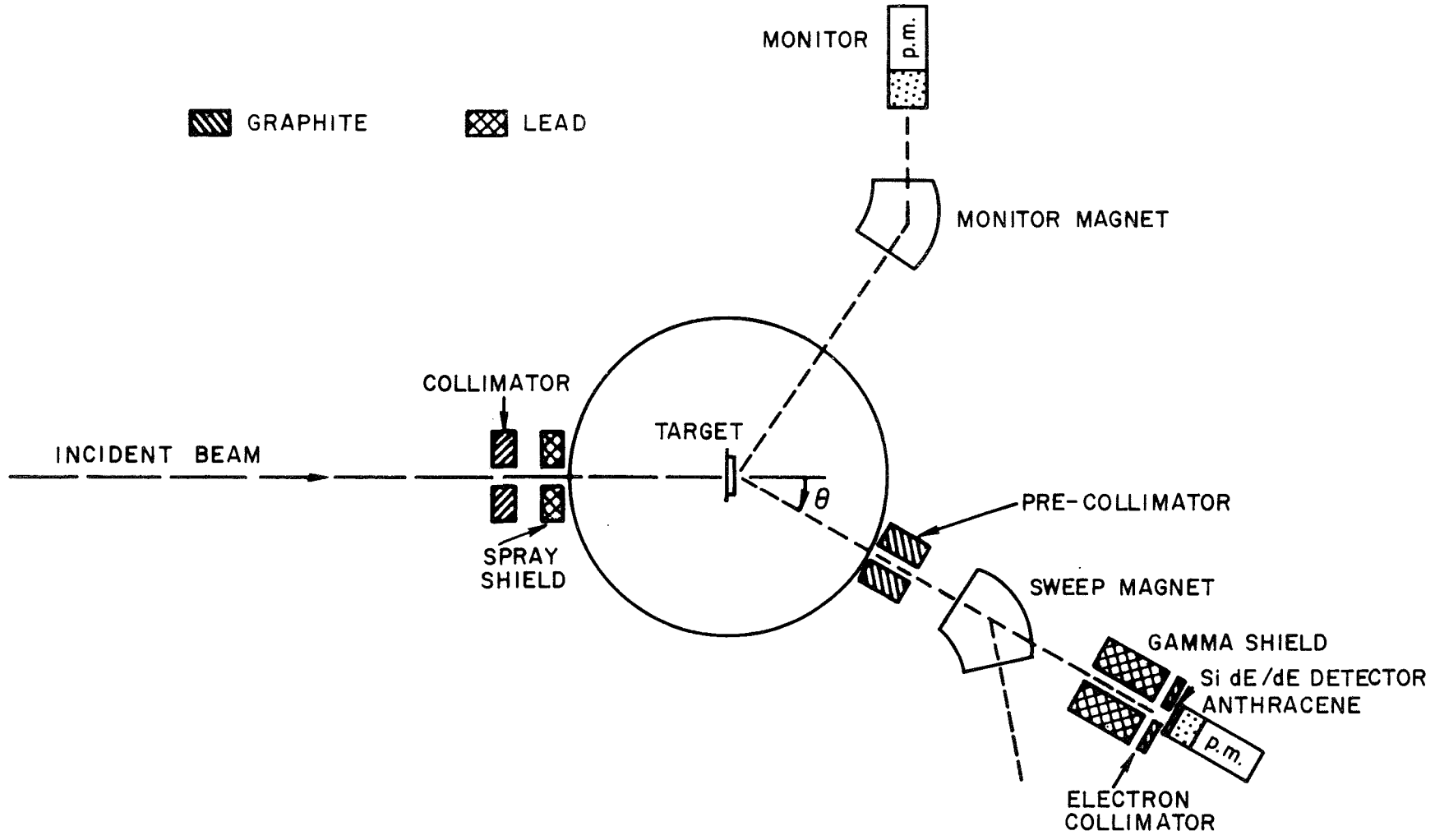

Fig. 1. Experimental arrangement for the electron transmission measurements

collimator defines the scattered beam, the precollimator was used only to reduce the number of uncounted electrons which scattered near the detector where they could produce background in the lead shielding. A sweep magnet was placed between the precollimator and the gamma shield, and was used to sweep out the scattered electron beam when determining the background from photons and from electrons produced by photons at the lead collimator. This background was of the order of a few percent of the data and could be accurately subtracted. On the other side of the incident beam are shown the monitor magnet and detector. This system is fixed in position at 40° and is used as a beam intensity monitor. The count rate recorded by this detector was proportional to the total number of electrons striking the target and could thus be used to normalize the spectra of transmitted electrons measured at the various angles (θ).

A major problem in measuring electron spectra in these experiments is that of distinguishing between electrons and background bremsstrahlung radiation. The latter has about the same intensity as the electron radiation. Since all scintillators suitable for measurement of electron spectra are sensitive to gamma radiation, a silicon transmission detector was used as part of the electron spectrometer to discriminate against gamma radiation. It was placed immediately in front of an anthracene crystal. The silicon detector is not very sensitive to photons, in fact less than one percent of the photons produced in a typical spectral measurement will interact with the silicon detector. Electrons, however, will produce a response in the detector with essentially 100 percent efficiency. By requiring that the silicon transmission detector and the anthracene give pulses in coincidence, electrons can be distinguished from photons with high reliability.

The silicon thickness of the dE/dX detector is 300 microns thick with a surface area of 50 mm^2. This thickness was chosen as a compromise among competing requirements: (1) the need to have pulse heights

from electrons that are sufficiently high to be separated from the noise, (2) the need to keep the energy loss small compared to the total energy so that the calibration correction will be small, and (3) the need to make the detector as transparent as possible to gamma radiation. The detector and the preamplifier, both of which were operated at room temperature, had a peak-to-peak noise between 30 and 40 keV, depending on the temperature. Thus electrons which lose more than approximately 40 keV will produce a measured pulse in the silicon detector. Stopping power calculations[4] indicate electrons in the energy range between 0.7 and 7 MeV will lose between 70 and 80 keV in a silicon wafer 300 microns thick. Chappell, et al.,[5] have measured the response of silicon to electrons. Their data indicate that electrons are likely to lose more energy than the stopping power indicates, rather than less. This fact has also been demonstrated in the transmission spectra measured in this program.[6] By accepting all pulses corresponding to energy losses greater than 40 keV, virtually all the electrons passing through the detector are counted without counting noise. The exact efficiency of the detector was not important in these experiments since it appears as a factor in the normalization constant discussed in Section 3.1. The energy dependence of the efficiency is small since the stopping power in silicon changes by only about 10 percent over the energy range of interest. By setting the acceptance level well below the calculated energy loss the effect of the stopping power variation with energy was less than one percent. The probability that a gamma ray with an energy between 0.7 and 7.0 MeV will interact with silicon is less than one percent and only a fraction of those that interact will result in a pulse of sufficient amplitude to be detected.

The electrons that passed through the silicon detector deposited all their energy in the anthracene crystal (less the $\approx$ 70 keV energy lost in the silicon detector) located directly behind the silicon wafer. The pulses from the photomultiplier viewing the anthracene crystal were

proportional to the energy of the electrons and therefore gave a pulse height representation of the energy spectrum. The response of the anthracene is very nearly Gaussian with a FWHM of 8 percent. The fact that electrons first lose energy in the silicon detector results in an energy scale shift such that zero pulse height corresponds to the average energy loss in the silicon detector. Further, straggling in the transmission detector gives rise to a broadening of the detector response system about the anthracene response. The total response of the system was determined by scattering the incident beam from a thin foil. The scattered electrons are nearly monoenergetic with a one percent energy spread. The response of the total system is Gaussian with a FWHM of about 9 percent.

Energy calibration of the anthracene was accomplished by scattering the incident beam from a thin foil and determining the pulse height corresponding to the peaks. The electron-nuclear scattering provided a peak at the incident energy and the electron-electron scattering provided a peak at a lower energy that depended on the scattering angle. The shape of the energy versus detector pulse-height dependence has been determined with a magnetic spectrometer for the particular photomultiplier voltage used. The energy response is linear and the intercept correction is very small.

In the experimental area the pulses from the silicon detector were fed into a charge sensitive preamplifier, the output of this unit was amplified before being sent to the data room to minimize the effect of rf noise pickup from the accelerator. The pulses from the anthracene detector were sufficiently large to be transmitted to the data room without preamplification. The standard electronic modules in the data room accomplished three primary functions: (1) they established coincidence between the silicon transmission detector and the anthracene detector, (2) they established coincidences between the accelerator injector pulses and events in either anthracene detector, and (3) they pulse-height analyzed

and stored the information from the anthracene detectors. The need for coincidence between the silicon and anthracene detectors has already been discussed. Coincidence with the accelerator injector was required to reduce background from non-beam associated sources. Scalars and a rate-meter were included in the setup so that the data collection rate could be monitored and the beam current adjusted to minimize pile-up. The current was always adjusted such that the fastest counting detector counted no more than one event for every 30 pulses. Thus the pile-up was kept below 1.5 percent of the data. The count rate of the anthracene was measured before coincidence was established with the silicon detectors; this was necessary since the bremsstrahlung count rate was about the same as the electron count rate whereas the pile-up rate depends on the total count rate in any one detector.

2.2 THICK TARGET BREMSSTRAHLUNG MEASUREMENTS

2.2.1 Measurements and Detectors

Targets of tin with thicknesses near the range of electrons were placed in the electron beam; the resulting bremsstrahlung energy spectrum was then measured at several angles (viz. 0°, 10°, 20°, 30°, 40°, 50°, 60°, 70°). The electron beam energy was either 4.0 or 8.0 MeV. The tin targets were 3.29 g/cm^2 thick for the measurements at 4.0 MeV; this corresponds to 1.15 times the range in the continuous slowing-down approximation (c.s.d.a.). At 8.0 MeV the target was 5.84 g/cm^2 thick, which corresponds to 1.15 times the c.s.d.a. range. The same target chamber and beam transport system used in the electron transmission measurements and described in Section 2.1 was used for the bremsstrahlung measurements for the angular range 10° through 70°. Thick target bremsstrahlung measurements were also made at 0° for 4 and 8 MeV for the above targets. The zero degree measurements required extensive

modifications to the beam transmission system, described in the next section, to reduce the high background associated with the old system.

Energy spectra were measured by using a large anticoincidence, Na(Tl)I scintillation spectrometer. The advantage of this spectrometer over other types is its high efficiency and simple response to gamma radiation, which facilitates unfolding gamma-ray spectra from measured pulse height distributions. Figure 2 shows the detector. The detector is made up of three crystals each encapsulated and light-sealed from the other. The three crystals are: (1) a main or center crystal, 4 inches in diameter and 9 inches long, (2) a side or annular crystal with an outside diameter of 8 inches, and also 9 inches long, and (3) a front crystal 8 inches in diameter and 3 inches thick, with a 1-inch-diameter hole through the center. The center crystal is viewed by a single 3-inch-diameter photomultiplier tube (Dumont 6363), the side crystal is viewed by five 2-inch-diameter tubes (RCA 6242-A), and the front crystal by four 2-inch-diameter tubes (RCA 6242-A). The anodes of the side crystals tubes are connected together. All tubes have individual high voltage adjustments for gain balancing. The output signals from the front and side crystals are summed in a common preamplifier; gain adjustments are provided on the preamplifier so that the two signals can be balanced.

After being collimated the incident radiation passes through the hole in the front crystal and strikes the main crystal. The collimator used for the bremsstrahlung measurements consists of a 1/2-inch hole in an 8-inch-thick lead block. The desired response of the main crystal is total absorption of the incident radiation, giving a single peak (broadened by the unavoidable instrumental resolution) for a monoenergetic gamma ray. Photoelectric absorption gives rise to such a peak; however, absorption by Compton and pair production processes can allow a portion of the energy to escape from the main crystal. The escaping Compton-scattered radiation from the crystal gives rise to a Compton tail on the

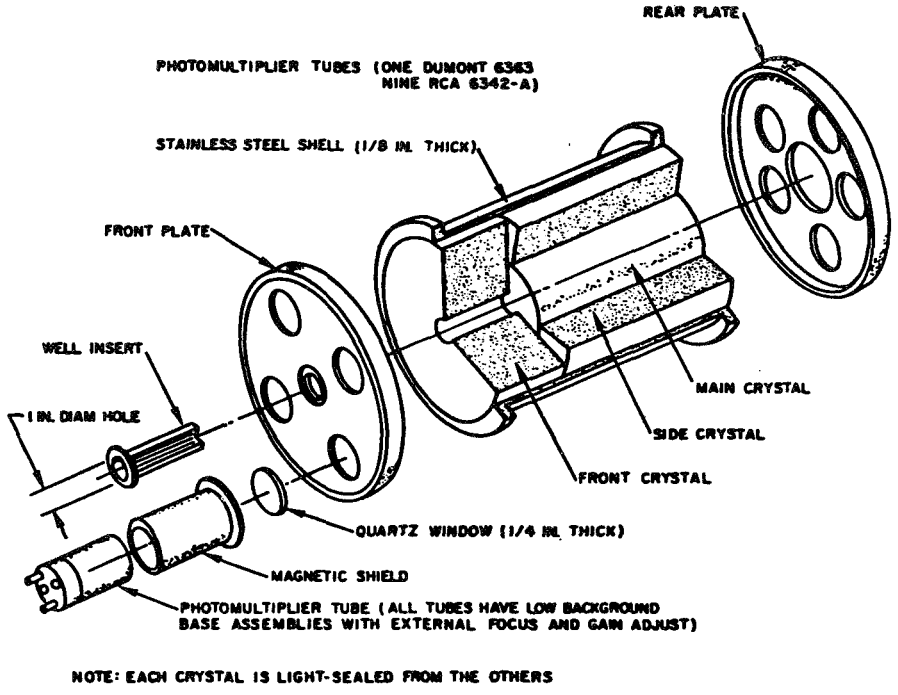

Fig. 2. Anticoincidence Na(Tl)I scintillation spectrometer

response while the escape of the positron annihilation radiation from pair production gives rise to single-escape and double-escape peaks at points lower in energy than the total energy absorption peak. Since the center crystal is surrounded by the front and side crystals, radiation which escapes from the center crystal has a high probability of producing an interaction in either the front or side crystals, and thus produces a signal indicating that some energy has escaped. An anticoincidence requirement is set such that events which produce a signal in the center crystal and also a signal in either the front or side crystal are rejected. The anticoincidence requirement greatly reduces the number of events that are recorded where some of the energy escapes from the center crystal. The efficiency is reduced somewhat in this scheme, but the shape of the response is greatly improved.

To unfold the bremsstrahlung energy spectra from the pulse-height data obtained from the detector, the detector's response to various gamma ray energies must be determined. Measurements of detector responses were made by placing radioactive gamma sources in essentially the target position so that the detector viewed them in parallel beam geometry. The gamma sources and corresponding lines were: ^{22}Na at 0.511 and 1.275 MeV, ^{137}Cs at 0.662 MeV, ^{54}Mn at 0.835 MeV, ^{88}Y at 0.90 and 1.84 MeV, ^{60}Co at 1.17 and 1.33 MeV, ^{24}Na at 1.37 and 2.75 MeV, and a Pu-Be source at 4.44 MeV (reaction ^{9}Be(α, n)^{12}C - 4.44 MeV).

The response to sources with one gamma-ray energy showed a flat Compton distribution. This simplified the analysis for those sources that have two gamma lines since it permitted extrapolating the Compton plateau due to the higher energy peak by drawing a horizontal line to lowest channels and subtracting all contributions by the higher energy peak from the pulse-height distribution to find the shape of the response to the low-energy peak.

Comparison with recent measurements on a Trail-Raboy type detector of the same over-all outside diameter [7] showed great similarity as regards the relative areas of the single- and double-escape peaks. Since those measurements included a gamma line at 6.13 MeV from ^{16}N, the corresponding escape peak parameters for this experiment could be extrapolated with added confidence to energies greater than 4.44 MeV. Furthermore, the sources for the detector efficiency calibration used in these measurements had previously been carefully cross calibrated to within ± 3 percent.

It was necessary to modify the beam monitoring system for the bremsstrahlung measurements since the old system magnetically analyzed the transmitted electron beam. Since most of the beam is stopped in the target used for the bremsstrahlung measurements, a new monitoring system had to be devised; it is described in the next section.

2.2.2 ΔE Detector Used as Beam Current Monitor

Experiments involving the measurement of small incident electron pulsed currents are hampered by the inability of the usual charge integration schemes to give accurate results. The usual method of charge integration is to charge (or discharge) a capacitor of known size with the beam current and measure the voltage and thus obtain the charge from $Q = \frac{V}{C}$. For large currents ($> 10^{-12}$ A), this method works very well. For smaller currents ($< 10^{-12}$ A) the accuracy of this method is significantly diminished because of dark currents in the system as well as leakage across insulators. Unless the environment of the system remains constant, changes in the dark current and leakage can take place, and these changes prevent the application of accurate corrections to the incident current. A further disadvantage is that the incident beam must be stopped in a Faraday cup. This prevents (in most cases) the use of the beam for an experiment while a current measurement is taking place. The latter

disadvantage rules out the use of a Faraday cup in the present work. To eliminate these difficulties a new beam monitor was developed.

If a pulsed monoenergetic electron beam is allowed to pass through a thin ($\approx$ 300 μ) ΔE detector, electron-hole pairs are formed in the detector. The number of electron-hole pairs formed is directly proportional to the number of electrons passing through the detector. The charge coming from the detector is then proportional to the number of incident electrons. This charge can then be integrated, and after calibration can be used to give the number of electrons passing through the detector. Two important advantages of this system are evident: (1) a charge amplification is possible, since each electron may produce several electron-hole pairs, and (2) the beam passing through the detector is only slightly degraded in energy ($\approx$ 50 keV) and therefore can be used in an experiment as well as being monitored at the same time.

Figure 3 shows the block diagram of the electronics associated with the ΔE detector. A charge sensitive preamplifier was used with conventional electronics for pulse shaping. The output of the amplifier was sent to a single channel pulse-height analyzer. By requiring coincidence between the analyzer output pulse and data pulse (i. e., the pulse from gamma-ray detector) pile-up could be eliminated. For if the beam intensity increased to a point where pile-up was probable the analyzer could be set such that the monitor pulse would be outside the window, thus, the data would not be counted for that beam pulse. Current integration was performed by a scaler counting the memory address pulse train coming from a multichannel analyzer's ADC. The number of pulses from the ADC is proportional to the pulse height, and the pulse height is proportional to the number of electrons in the beam pulse. The scaler keeps a running sum of the pulse heights coming from the monitor detector, and this sum is proportional to the number of electrons that have passed through the detector. That this is indeed the case may be seen from the following discussion.

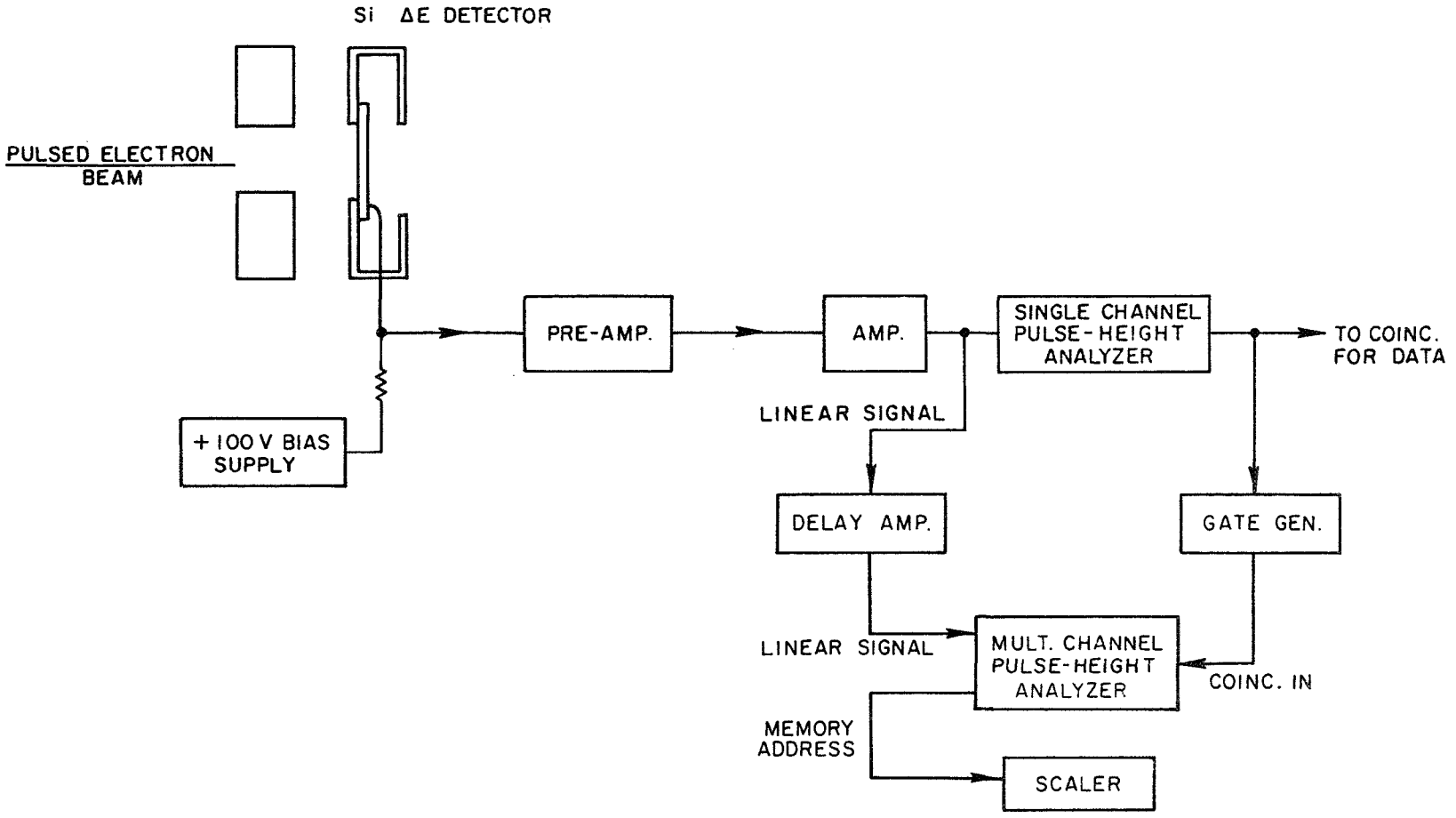

Fig. 3. Block diagram of electronics used with ΔE beam current monitor

Consider N_1 electrons passing through ΔE detector in the first pulse, N_2 in the second pulse and so on. The total number of electrons in k pulses is:

$$N = \sum_{j=1}^{k} N_j \tag{1}$$

Let Q_j = charge collected during the j^{th} pulse. In a run the total charge collected is just

$$Q = \sum_{j=1}^{k} Q_j \tag{2}$$

We may break up the j^{th} pulse into electron groups. Let N_{1j} = the number of electrons producing charge q_1, N_{2j} = number of electrons producing q_2 charge, etc. Thus

$$Q_j = \sum_{i=1}^{\ell} q_i N_{ij} \tag{3}$$

and

$$Q = \sum_{j=1}^{k} \sum_{i=1}^{\ell} q_i N_{ij} \tag{4}$$

rearranging the order of summation

$$Q = \sum_{i=1}^{\ell} q_i \sum_{j=1}^{k} N_{ij} \tag{5}$$

For a large number of electrons, N,

$$\sum_{j=1}^{k} N_{ij} = N f(q_i) \tag{6}$$

Where $f(q_i)$ is the probability of q_i being produced in the detector. Now Q is given by

$$Q = \sum_{i=1}^{\ell} q_i \, N \, f(q_i) = N \sum_{i=1}^{\ell} q_i \, f(q_i) \tag{7}$$

or

$$Q' = (q_{av})N \tag{8}$$

where q_{av} is just the average charge produced in the detector by an electron. From the above it should be noted that only N needs to be a large number for statistical confidence and it is not necessary for N_j, the number of electrons in the j^{th} pulse, to be large.

The sum of all the pulse heights (scalar number C_k) will be proportional to Q and thus to N. This gives

$$N = K C_k \tag{9}$$

where K is proportionality constant which is determined by a calibration run.

The calibration of the monitor was done in the following way. The beam was permitted to pass through the detector into a Faraday cup and the total charge was measured by conventional current integration. Knowing the total charge and thus the total number of electrons the proportionality constant could be found.

Tests have been made to check the linearity of the beam monitor as beam intensity was changed. Calibration runs were made for widely different average beam currents, and K was obtained. Table 1 shows the results of these runs.

Table 1

Average Current (Amp)	K (electrons/scaler count)
2.92×10^{-12}	2608
5.0×10^{-12}	2550
2.37×10^{-11}	2598
5.0×10^{-11}	2538

The average value of K from these runs is 2574 (electrons/scaler count). The maximum deviation from the average value is 1.4 percent.

The stability of the monitor has been demonstrated by performing calibration runs separated by about one month of time. The amplifier for the monitor system was adjusted by means of a precision pulser so that the two runs were performed with the same electronic gain. The proportionality constant differed by only 1.5 percent between these two runs.

One additional advantage is obtained by this monitor. The LINAC operator has an indication of beam intensity by viewing the linear signal on a scope pulse by pulse, and can tune the machine so that the pulses are more uniform in size. Other monitor systems do not have this advantage but only give an average indication. Sudden changes in beam intensity are seen much sooner with this system than with an average indicator, and can be corrected faster.

2.3 THIN TARGET BREMSSTRAHLUNG MEASUREMENTS

When the energy of the incident electron beam is much greater than the rest mass energy of the electron, the bremsstrahlung yield from a thin target is concentrated in a narrow cone around the incident beam direction. The angle of the cone is given roughly by $\theta = \frac{MoC^2}{E}$, where E is the energy of the electrons. For 8 MeV electrons $\theta \approx 0.06$ radians or 3.6^{o}. For 4 MeV electrons the angle is then around 7.2^{o}. This means that thin target bremsstrahlung measurements at these energies must be made by a detector looking within a small angle of the beam direction. At these angles the detector is illuminated by bremsstrahlung from the target as well as any thing the beam has struck in traveling down the beam pipe. The bremsstrahlung from anything other than the target, of course, constitutes a background which must be kept small. Past experience with this collimation system which was used for the electron transmission measurements has shown a large bremsstrahlung background for angles less than 5^{o} which is just the region of interest for the thin target bremsstrahlung measurements. Simple shielding of the collimators did not prove effective since a hole in the shielding must be provided which is large enough so that no direct or scattered electrons strike the shielding thereby producing further bremsstrahlung. The most satisfactory solution is to remove the collimators and provide a free drift region for the electrons. Past attempts to run without these collimators have not been satisfactory because of instabilities in the accelerator energy and the magnetic transport system producing a drift of the electron beam from the center of the target. The instabilities, though small, are magnified because of the long distances involved.

Minor changes in the beam transport system, however, produced a system which greatly improved performance since the difficulties were largely eliminated. Figure 4 shows the layout of the new system. An aluminum collimator with a 3/8-in. hole is placed just before the entrance

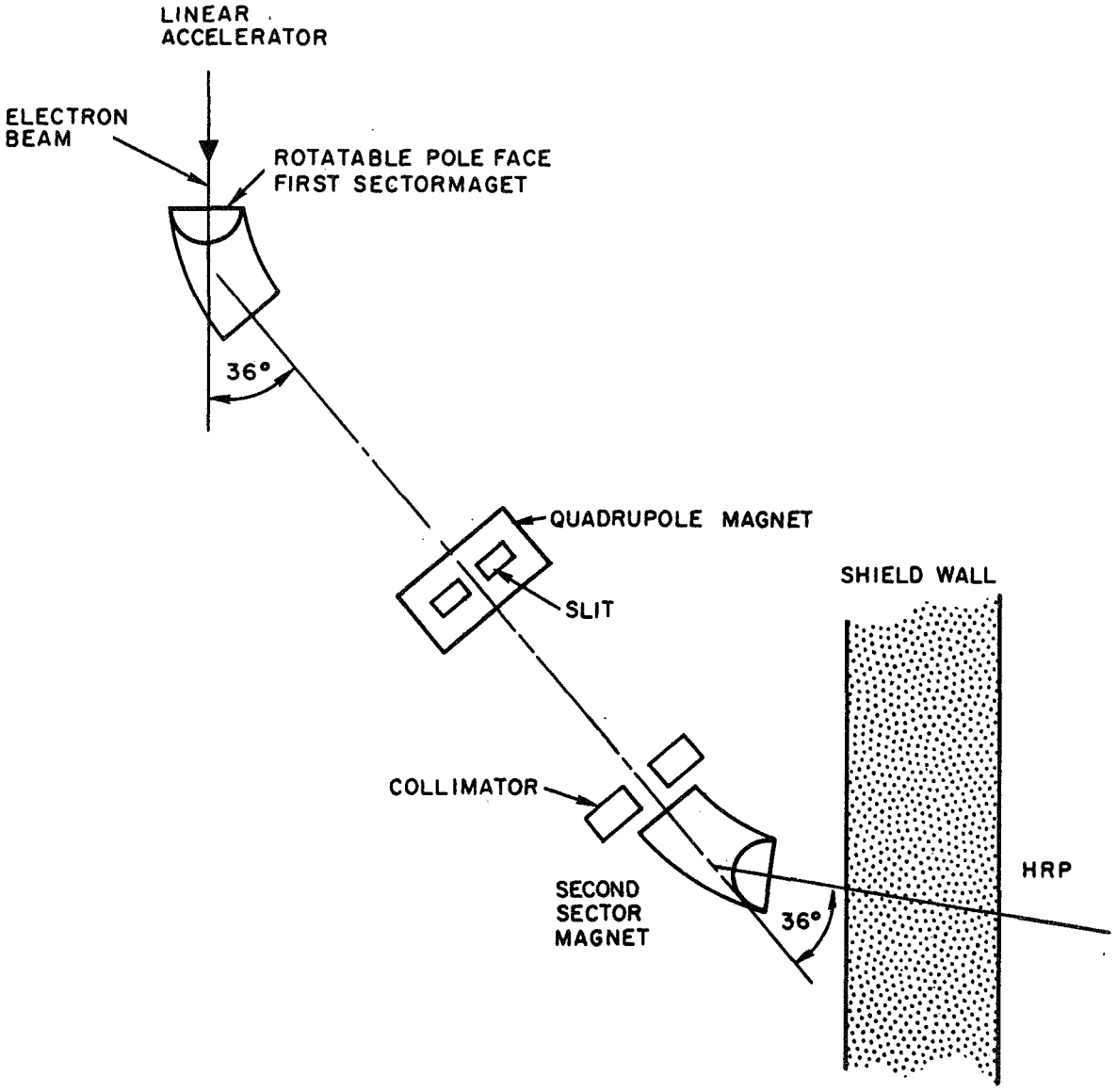

Fig. 4. Electron beam transport system showing position of slit and new collimator

to the second 36° magnet. The slit for the first 36° magnet was moved midway between the two 36° magnets where better control of beam energy is obtained. Figure 4 shows the changes in the magnet system. Since the two 36° magnets have the same current (they are series connected) slight changes in magnet current cannot produce changes in position on the target. The only way the beam position can change is if the position or direction of the beam changes on entering the second 36° magnet. The collimator and slit determine the direction under which the beam enters the second 36° magnet and the collimator determines the position of the beam and entrance. The slit and the first 36° magnet, of course, control the energy of the beam viewed by the second magnet. This arrangement results in a system which is inherently very stable; in addition, the detector was very well shielded from all collimators.

Two quadrupole magnets were placed in the system after the second 36° magnet; these served to focus the beam to a small spot at the target position. An accelerator run was made while viewing the beam spot on a screen placed at the target positions via a television monitor. Adjustment of the quadrupole magnets after the final bend produced a spot approximately 3/16 inch in diameter. The accelerator conditions were changed over a wide range. This caused the beam current to change but no movement of the center of spot was observed. Small changes (0.3 percent) in the bending magnet current showed no movement of the spot center.

Thin targets of silver and gold were placed in the electron beam and the energy spectra of bremsstrahlung produced at the targets were measured for 0°, 1.5° and 3°. The electron energy was 8 MeV; the target was 0.601 mg/cm^2 thick for the gold and 0.50 mg/cm^2 for the silver. For electron energy of 4 MeV bremsstrahlung spectra were obtained at 0°, 3°, and 6° for the gold and silver targets. The bremsstrahlung energy spectra were measured with the anticoincidence NaI detector described in Section 2.2.1. After the electron beam passed through the target the beam

was bent into a Faraday cup by a magnet placed after the scattering chamber. Conventional current integration was used to determine the total charges of a run. Background counts were determined by removing the targets and placing an empty target holder in the target chamber. The background runs gave counting rates of about half the counting rates with the target foils in place. It is estimated that the background has been lowered several orders of magnitude at 0^{o} with the new collimation system.

3. RESULTS

3.1 ELECTRON TRANSMISSION MEASUREMENTS

The normal incidence spectral data have been normalized to one incident electron by the following calibration procedures. The electron flux was plotted in two ways:

1. Flux versus the cosine of the corresponding angle
2. Flux multiplied by the sine of the corresponding angle and the product plotted versus angle.

A smooth curve was drawn through the points in each plot and the area, A, under each distribution determined. These areas correspond to two separate integrations of the transmitted electrons over the forward hemisphere, normalized to the beam monitor. The results of the two integrations always agreed to within one percent. The angular distribution and energy spectra were then renormalized to one incident electron by multiplying the data by a normalization factor Na where N is given by the following expression:

$$N = \frac{\text{electrons transmitted through target}}{A} .$$

The number of electrons transmitted through the targets were taken from the work of Ebert, et al., [8, 9] and are displayed in Table 2 along with pertinent data about the targets. The estimated error on these experimentally determined transmission fractions is 2 percent. Also shown in the table are values generated with ETRAN 15, a Monte Carlo computer program. [1]

Table 2

Material	Incident Beam Energy (MeV)	Target Thickness g/cm^2	csda Range	Ebert	ETRAN 15
Sn	8.0	3.29	0.65	0.080	0.082
Sn	8.0	2.42	0.5	0.337	0.330
Sn	8.0	1.02	0.2	0.916	0.900
Sn	4.0	1.47	0.5	0.072	0.112
Sn	4.0	0.595	0.2	0.723	0.760

The oblique incidence data were normalized with a common monitor to spectra measured with normal incidence. This was necessary because integration in the manner described above was rendered inaccurate or not possible by the nonsymmetric character of the transmitted data. The thin silicon transmission detector described in Section 2. 2 was placed in the beam. Since electrons passing through the detector lose very little energy, the beam is essentially unperturbed by the monitor. When the signal from this monitor is integrated, the integral is proportional to the charge incident on the target. Spectra were measured at 30° and 40° at each angle of incidence. The ratio of these spectra per unit monitor output gives the factor by which the oblique incidence data must be adjusted to be correctly normalized.

The results at normal incidence are shown in Figs. 5 through 14 and Tables 3 through 7. The curve drawn through the points is the Landau universal function[10] least squares fitted to the data points. As is indicated in these figures the fit to the data is excellent. The fit was accomplished by adjusting only three parameters: (1) a normalization factor, (2) a parameter corresponding to the most probable exit energy, and (3) a straggling width parameter. A very useful analytical approximation to the Landau function is given by Blunck and Leisegang.[11] They approximate the Landau function by a series of Gauss functions:

$$\varphi(\lambda) = \sum_{\nu=1}^{4} C\nu \exp\left[-\left(\frac{\lambda+\lambda\nu}{\gamma\nu}\right)^2\right] \qquad (10)$$

The value of the constants $C\nu$, $\gamma\nu$, and $\lambda\nu$ are displayed in Table 3.

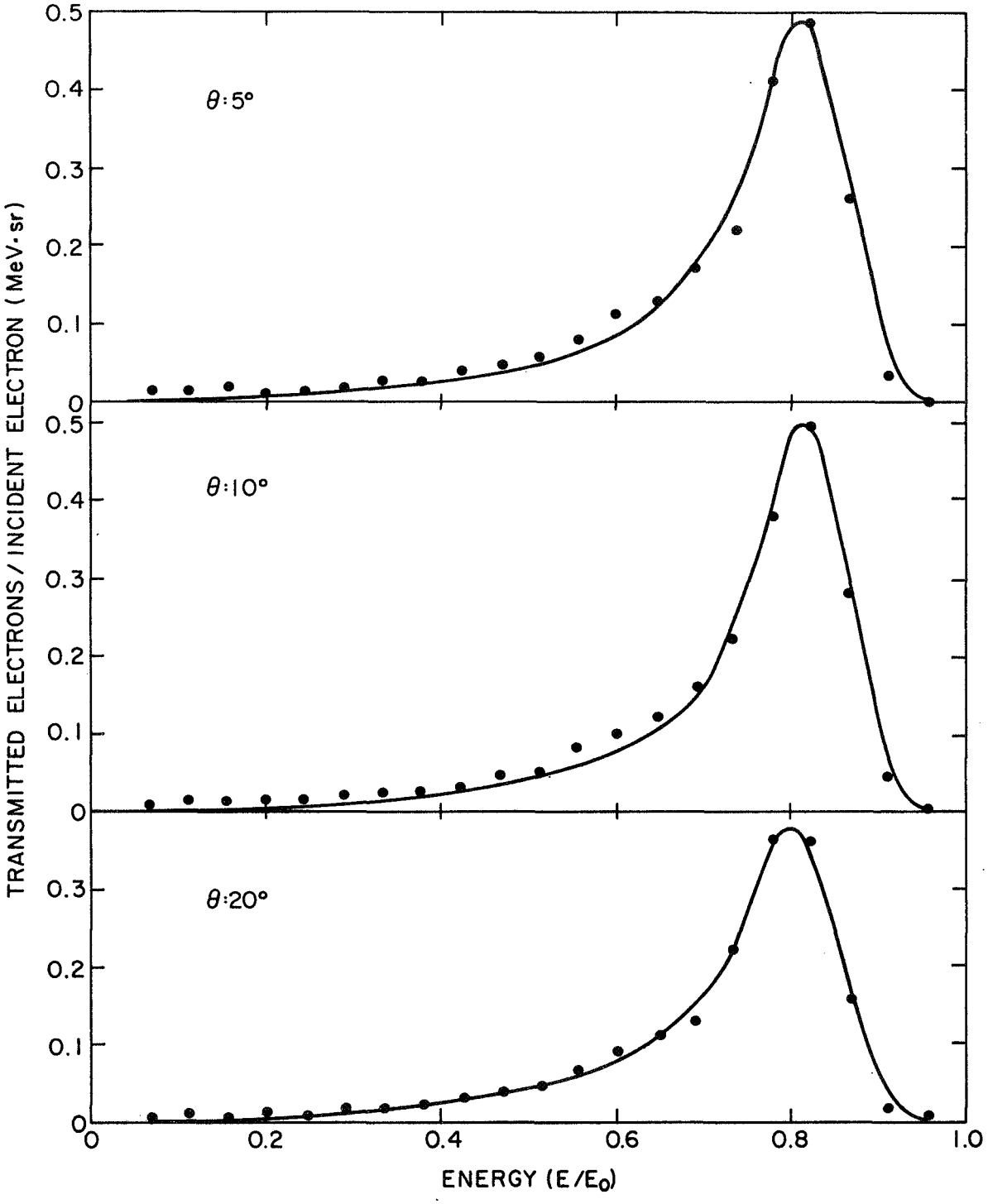

Fig. 5. Spectra at 5°, 10°, and 20° of straggled electrons emitted from a 0.595 g/cm^2 thick tin target bombarded by 4.0 MeV electrons. The solid curve is the Landau function fitted to the data point.

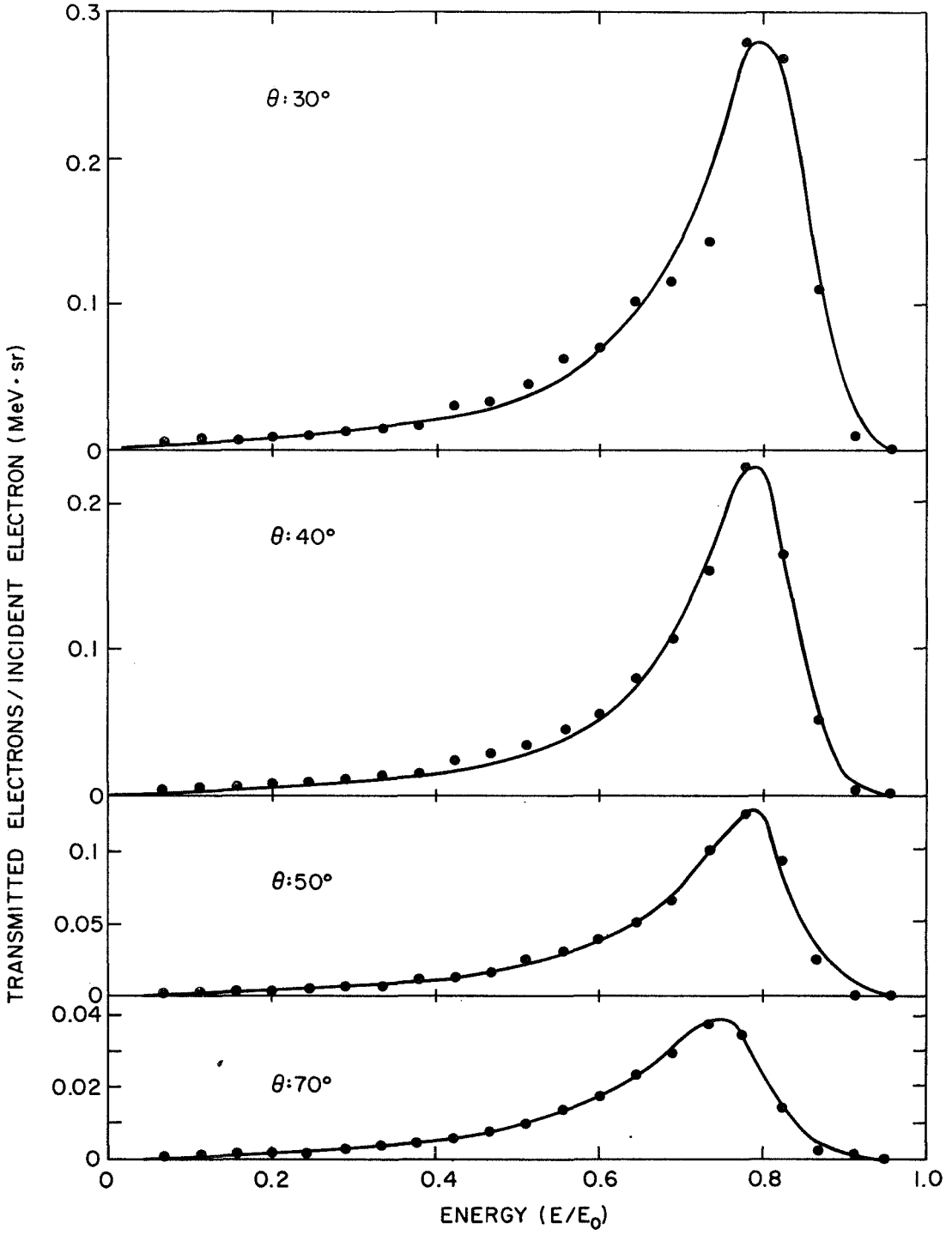

Fig. 6. Spectra at 30°, 40°, 50°, and 70° of straggled electrons emitted from a 0.595 g/cm^2 thick tin target bombarded by 4.0 MeV electrons. The solid curve is the Landau function fitted to the data points.

Table 3

EXPERIMENTAL DATA FOR 4.0 MeV ELECTRONS INCIDENT ON 0.595 g/cm^2 Sn TARGET

θ / E/E_o	Transmitted Electrons/Incident Electron-(MeV-sr)						
	5°	10°	20°	30°	40°	50°	70°
0.069	0.0116	0.0102	0.0074	0.0047	0.0050	0.0030	0.0009
0.114	0.0141	0.0135	0.0122	0.0086	0.0054	0.0038	0.0014
0.160	0.0195	0.0135	0.0099	0.0075	0.0055	0.0040	0.0018
0.206	0.0116	0.0162	0.0138	0.0111	0.0084	0.0056	0.0020
0.252	0.0170	0.0170	0.0122	0.0116	0.0096	0.0053	0.0022
0.298	0.0187	0.0223	0.0181	0.0111	0.0112	0.0078	0.0029
0.343	0.0282	0.0244	0.0189	0.0156	0.0127	0.0080	0.0036
0.389	0.0278	0.0265	0.0260	0.0164	0.0160	0.0122	0.0045
0.435	0.0399	0.0332	0.0314	0.0303	0.0237	0.0137	0.0064
0.481	0.0444	0.0476	0.0385	0.0345	0.0303	0.0161	0.0087
0.526	0.0581	0.0536	0.0477	0.0448	0.0351	0.0251	0.0099
0.572	0.0781	0.0822	0.0686	0.0626	0.0458	0.0314	0.0130
0.618	0.108	0.101	0.0908	0.0720	0.0604	0.0405	0.0179
0.664	0.130	0.121	0.112	0.102	0.0798	0.0495	0.0233
0.710	0.173	0.157	0.134	0.127	0.107	0.0666	0.0295
0.755	0.222	0.226	0.223	0.184	0.154	0.0994	0.0381
0.801	0.408	0.386	0.358	0.281	0.224	0.123	0.0359
0.847	0.487	0.500	0.362	0.271	0.165	0.0930	0.0153
0.893	0.265	0.279	0.155	0.113	0.0531	0.0260	0.0028
0.939	0.0378	0.0478	0.0176	0.0097	0.0044	0.0035	0.0002
0.984	0.0046	0.0039	0.0026	0.0008	0.0010	0.0014	0.00007

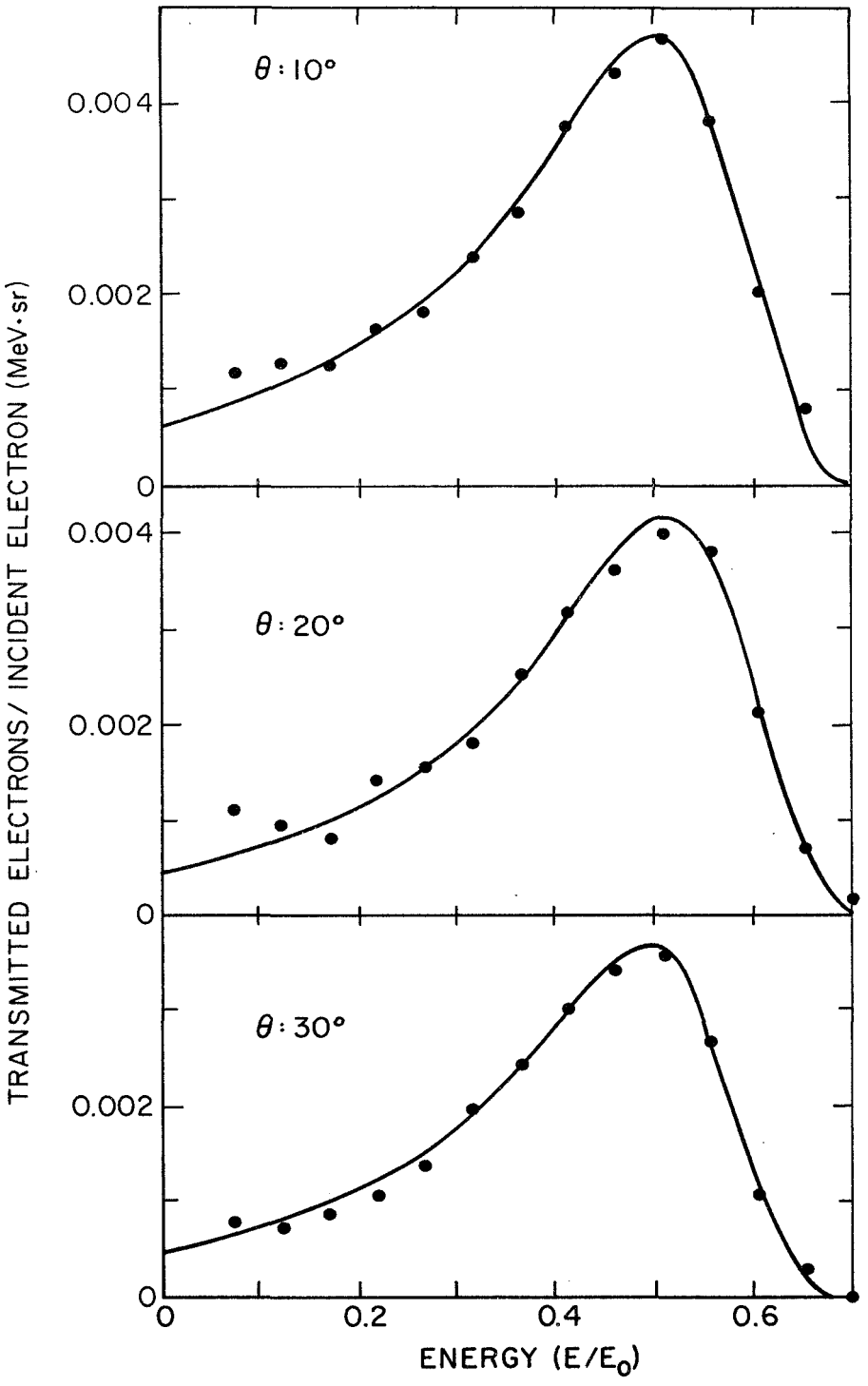

Fig. 7. Spectra at 10°, 20° and 30° of straggled electrons emitted from a 1.47 g/cm^2 thick tin target bombarded by 4.0 MeV electrons. The solid curve is the Landau function fitted to the data points.

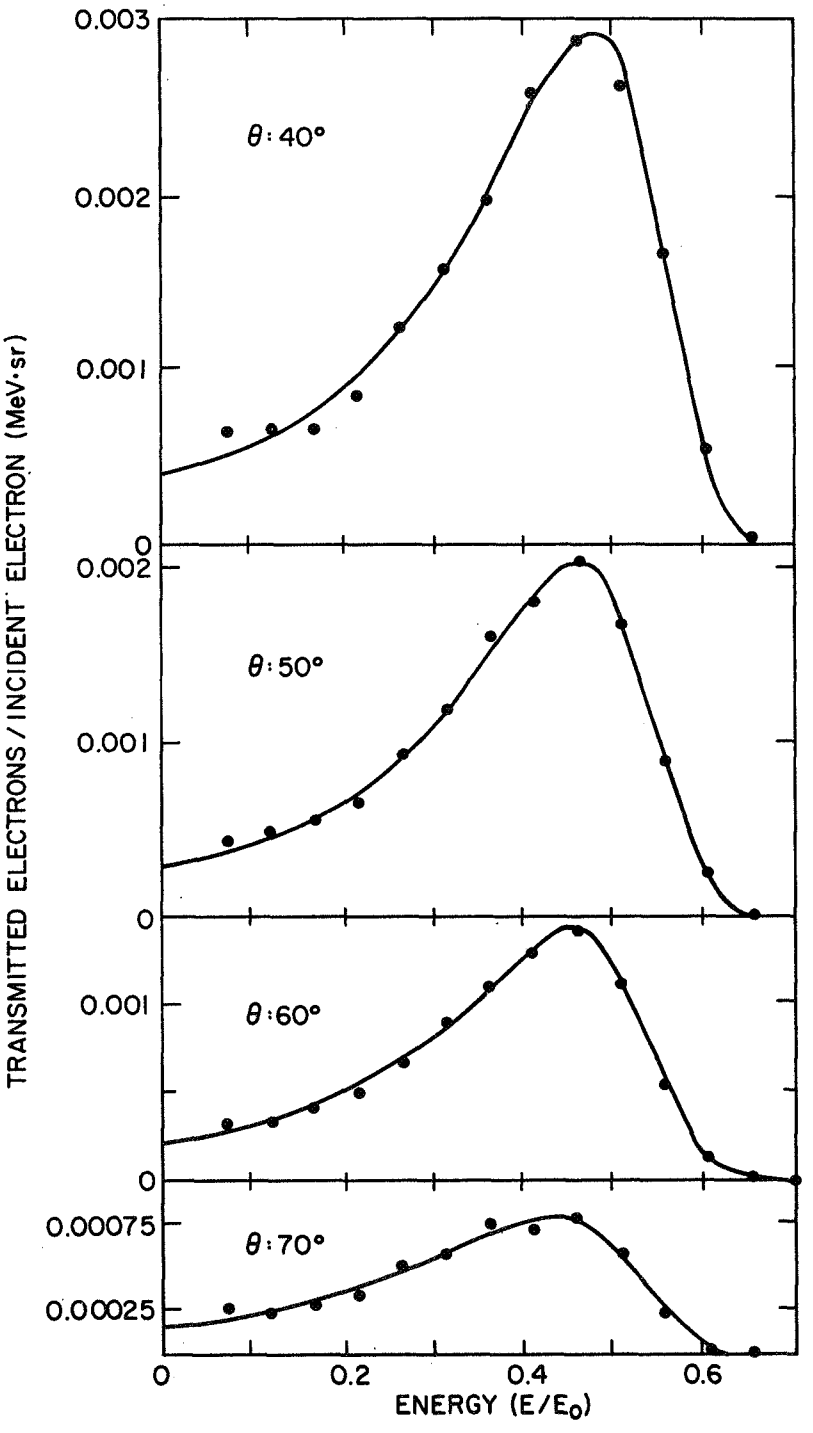

Fig. 8. Spectra at 40°, 50°, 60°, and 70° of straggled electrons emitted from a 1.47 g/cm^2 thick tin target bombarded by 4.0 MeV electrons. The solid curve is the Landau function fitted to the data points.

Table 4

EXPERIMENTAL DATA FOR 4 MeV ELECTRONS ON
1.47 g/cm^2 THICK TARGET OF Sn

E/E_o \ θ	Transmitted Electron/Incident Electron-(MeV-sr)						
	10^o ($\times 10^{-3}$)	20^o ($\times 10^{-3}$)	30^o ($\times 10^{-3}$)	40^o ($\times 10^{-3}$)	50^o ($\times 10^{-3}$)	60^o ($\times 10^{-3}$)	70^o ($\times 10^{-3}$)
0.072	1.19	1.09	0.78	0.64	0.44	0.33	0.26
0.121	1.29	0.96	0.72	0.64	0.49	0.33	0.24
0.170	1.26	0.80	0.88	0.78	0.54	0.42	0.28
0.218	1.62	1.41	1.05	0.85	0.65	0.49	0.33
0.267	1.80	1.54	1.38	1.22	0.92	0.68	0.49
0.315	2.38	1.80	1.99	1.56	1.18	0.91	0.56
0.364	2.85	2.47	2.45	1.97	1.60	1.10	0.74
0.412	3.78	3.15	3.01	2.58	1.80	1.29	0.71
0.461	4.30	3.60	3.43	2.88	2.04	1.40	0.78
0.509	4.67	4.00	3.60	2.61	1.69	1.14	0.59
0.558	3.80	3.86	2.70	1.66	0.88	0.54	0.23
0.606	2.04	2.12	1.08	0.54	0.26	0.12	0.04
0.654	0.81	0.71	0.28	0.07	0.03	0.03	0.01
0.703	----	0.22	0.08	----	----	----	----

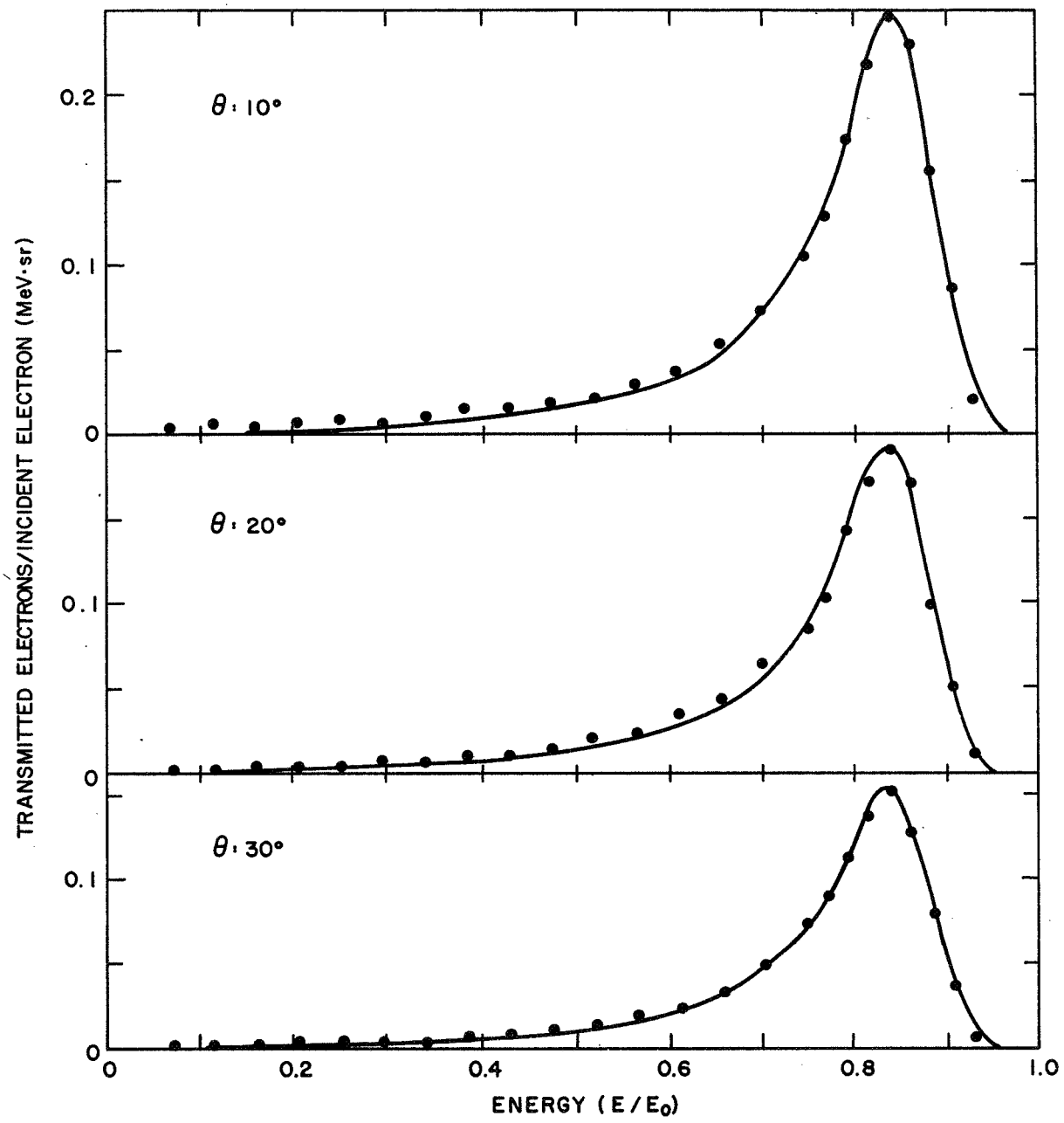

Fig. 9. Spectra at 10°, 20°, and 30° of straggled electrons emitted from 1.02 g/cm^2 thick tin target bombarded by 8.0 MeV electrons. The solid curve is the Landau function fitted to the data points.

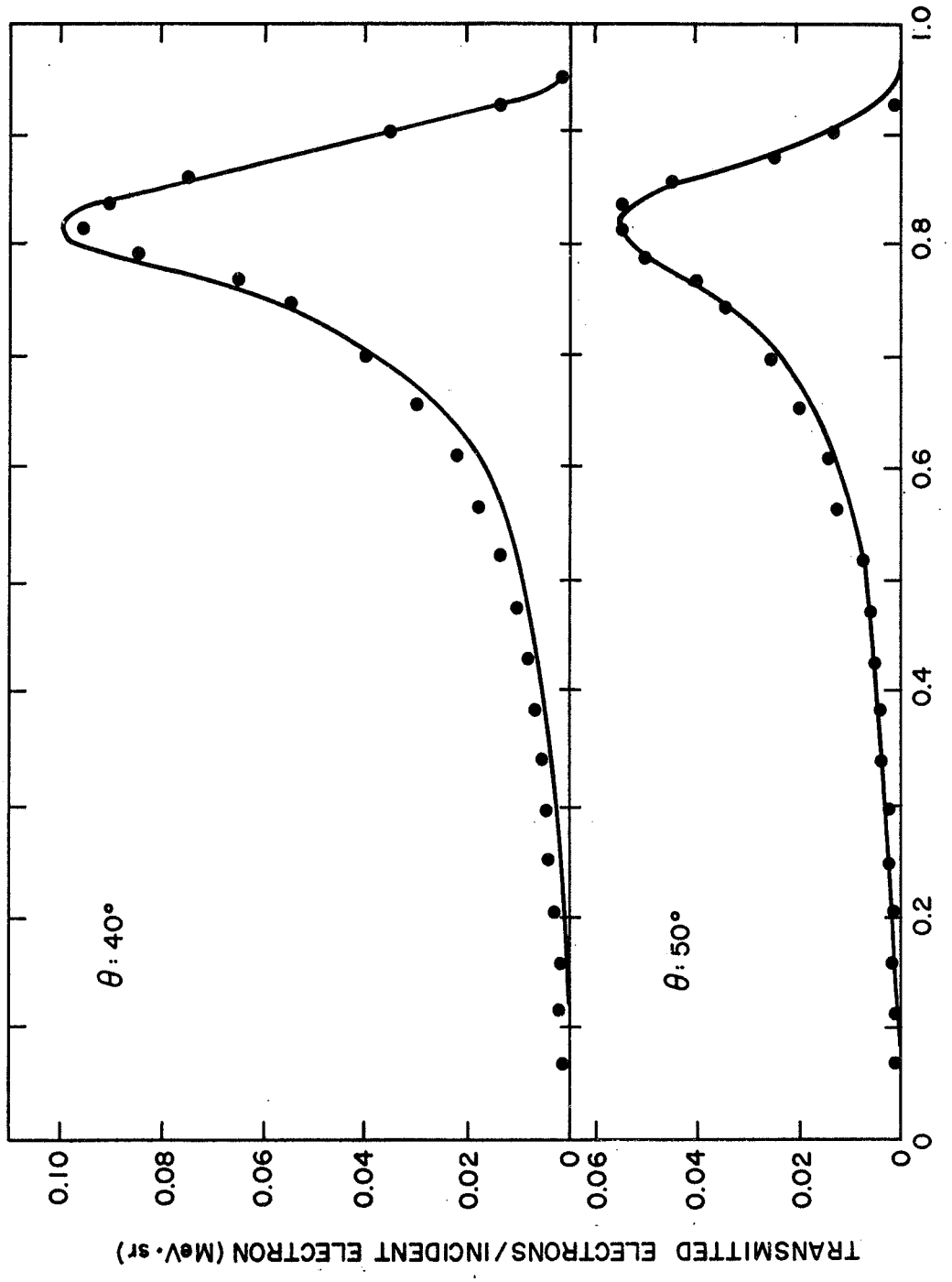

Fig. 10. Spectra at 40^{o} and 50^{o} of straggled electrons emitted from 1.02 g/cm^{2} thick tin target bombarded by 8.0 MeV electrons. The solid curve is the Landau function fitted to the data points.

Table 5

EXPERIMENTAL DATA FOR 8.0 MeV ELECTRONS ON 1.02 g/cm^2 THICK TARGET OF Sn

θ / E/E_o	Transmitted Electrons/Incident Electron-(MeV-sr)				
	10^o	20^o	30^o	40^o	50^o
0.068	0.003	0.003	0.003	0.001	0.001
0.114	0.006	0.004	0.003	0.002	0.001
0.159	0.005	0.005	0.003	0.002	0.002
0.204	0.007	0.005	0.004	0.003	0.001
0.250	0.008	0.005	0.004	0.004	0.002
0.295	0.007	0.008	0.006	0.004	0.002
0.340	0.010	0.007	0.006	0.005	0.004
0.386	0.012	0.010	0.007	0.006	0.004
0.432	0.013	0.012	0.009	0.008	0.005
0.478	0.017	0.015	0.012	0.010	0.006
0.523	0.020	0.019	0.014	0.013	0.007
0.568	0.029	0.025	0.020	0.018	0.012
0.614	0.038	0.035	0.024	0.022	0.014
0.659	0.053	0.046	0.035	0.029	0.019
0.704	0.072	0.065	0.049	0.039	0.024
0.750	0.106	0.085	0.074	0.055	0.034
0.773	0.127	0.103	0.091	0.065	0.040
0.795	0.177	0.144	0.112	0.085	0.049
0.818	0.218	0.169	0.139	0.095	0.055
0.840	0.245	0.189	0.152	0.091	0.054
0.864	0.237	0.169	0.129	0.074	0.045
0.886	0.156	0.099	0.079	0.036	0.025
0.909	0.086	0.050	0.034	0.014	0.013
0.932	0.020	0.010	0.008	0.002	0.003

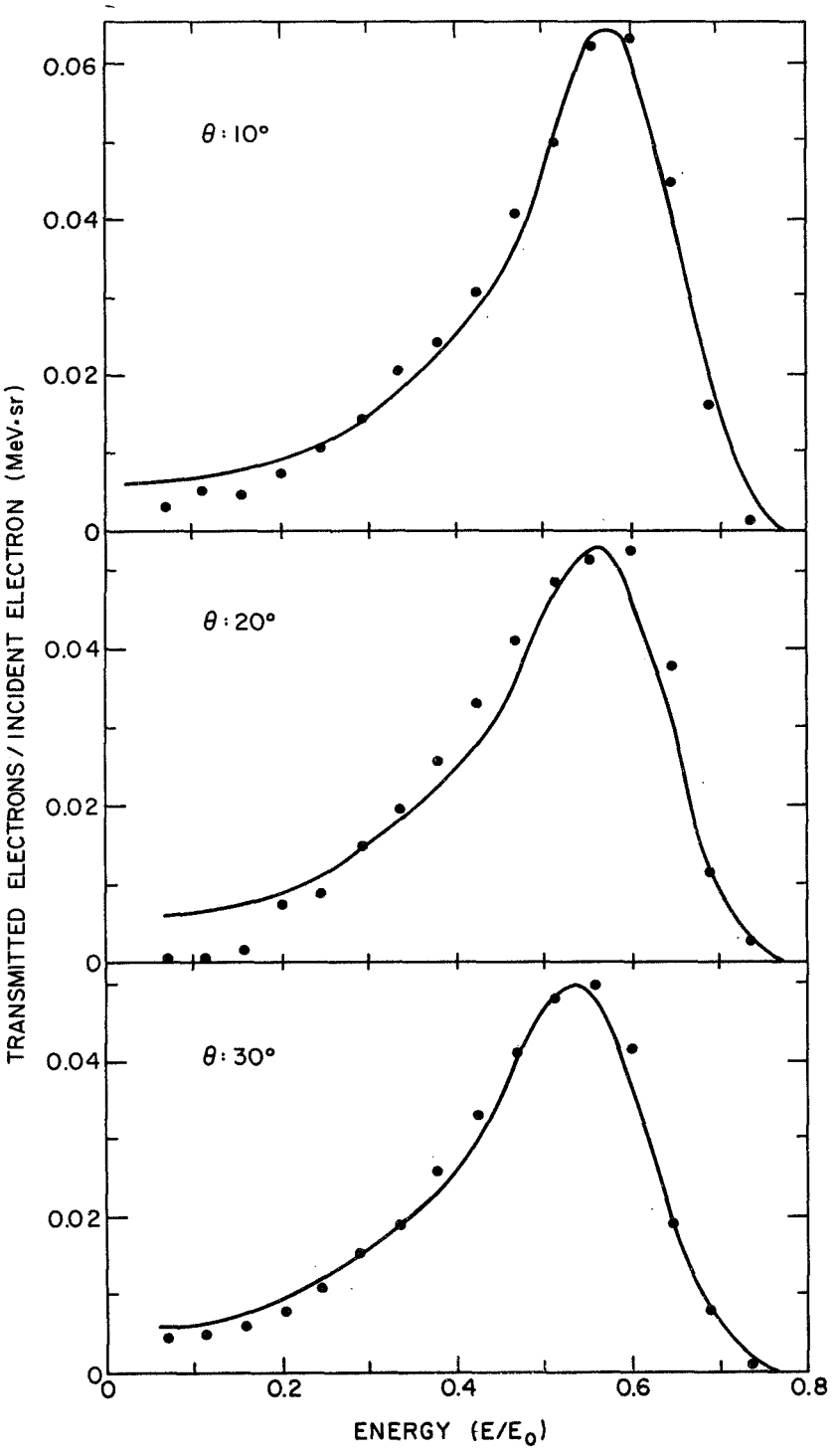

Fig. 11. Spectra at 10°, 20°, and 30° of straggled electrons emitted from 2.42 g/cm^2 thick tin target bombarded by 8.0 MeV electrons. The solid curve is the Landau function fitted to the data points.

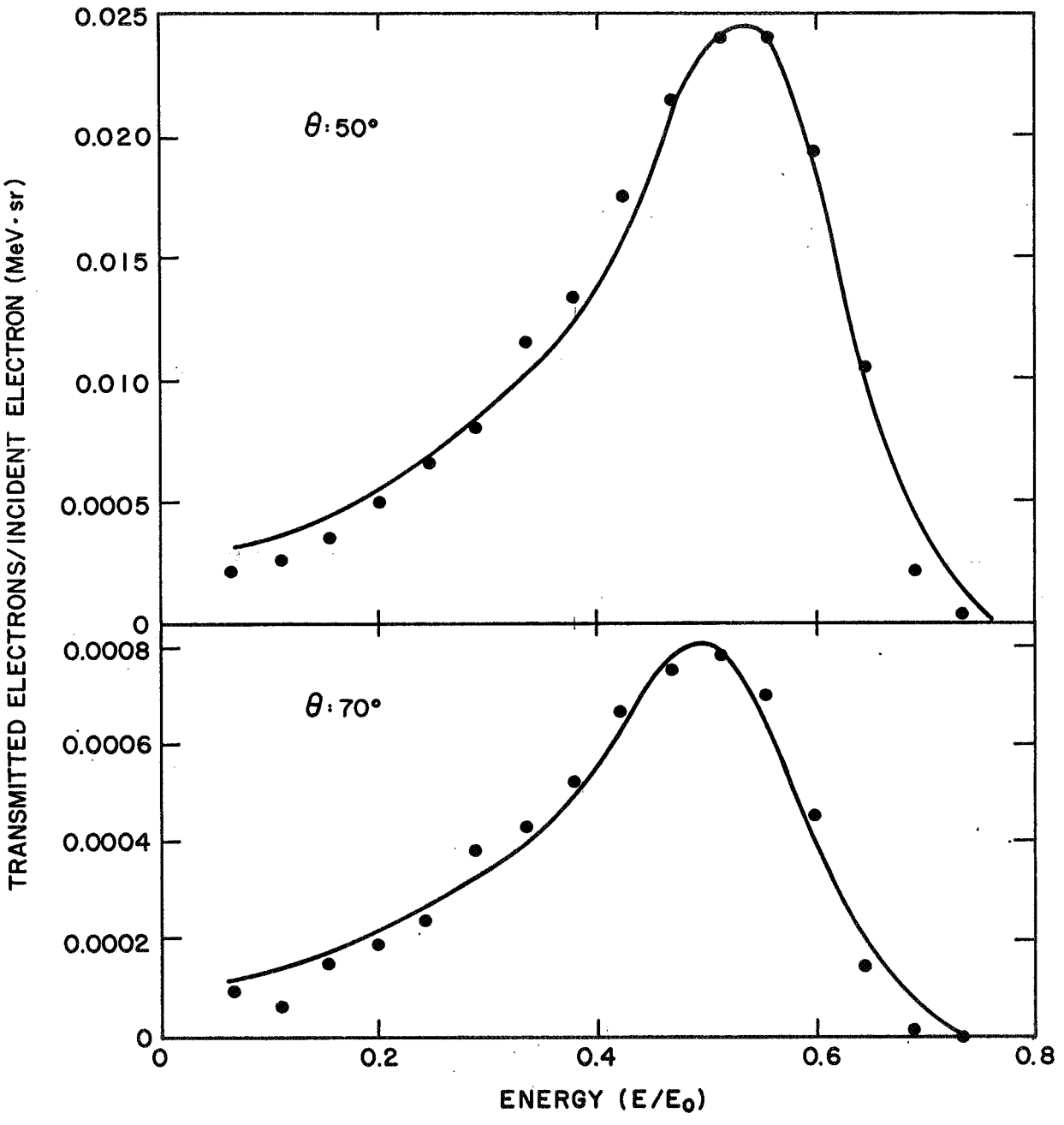

Fig. 12. Spectra at 50° and 70° of straggled electrons emitted from 2.42 g/cm^2 thick tin target bombarded by 8.0 MeV electrons. The solid curve is the Landau function fitted to the data points.

Table 6

EXPERIMENTAL DATA FOR 8.0 MeV ELECTRONS INCIDENT ON 2.42 g/cm^2 THICK Sn TARGET

θ / E/E_o	Transmitted Electrons/Incident Electron-(MeV-sr)				
	10^o ($\times 10^{-2}$)	20^o ($\times 10^{-2}$)	30^o ($\times 10^{-2}$)	50^o ($\times 10^{-2}$)	70^o ($\times 10^{-2}$)
0.068	0.296	0.0	0.43	0.21	0.093
0.114	0.526	0.0	0.48	0.28	0.057
0.160	0.447	0.105	0.59	0.36	0.150
0.205	0.724	0.734	0.81	0.50	0.193
0.251	1.05	0.892	1.13	0.65	0.239
0.297	1.45	1.47	1.56	0.80	0.389
0.342	2.07	1.94	1.91	1.16	0.435
0.388	2.43	2.57	2.64	1.36	0.528
0.434	3.16	3.33	3.34	1.77	0.670
0.479	4.08	4.15	4.14	2.15	0.752
0.525	4.97	4.88	4.80	2.40	0.799
0.571	6.18	5.17	4.95	2.41	0.706
0.616	6.28	5.27	4.20	1.95	0.456
0.662	4.47	3.77	1.94	1.05	0.143
0.708	1.55	1.13	0.404	0.21	0.025
0.753	0.164	0.24	0.107	0.028	0.0

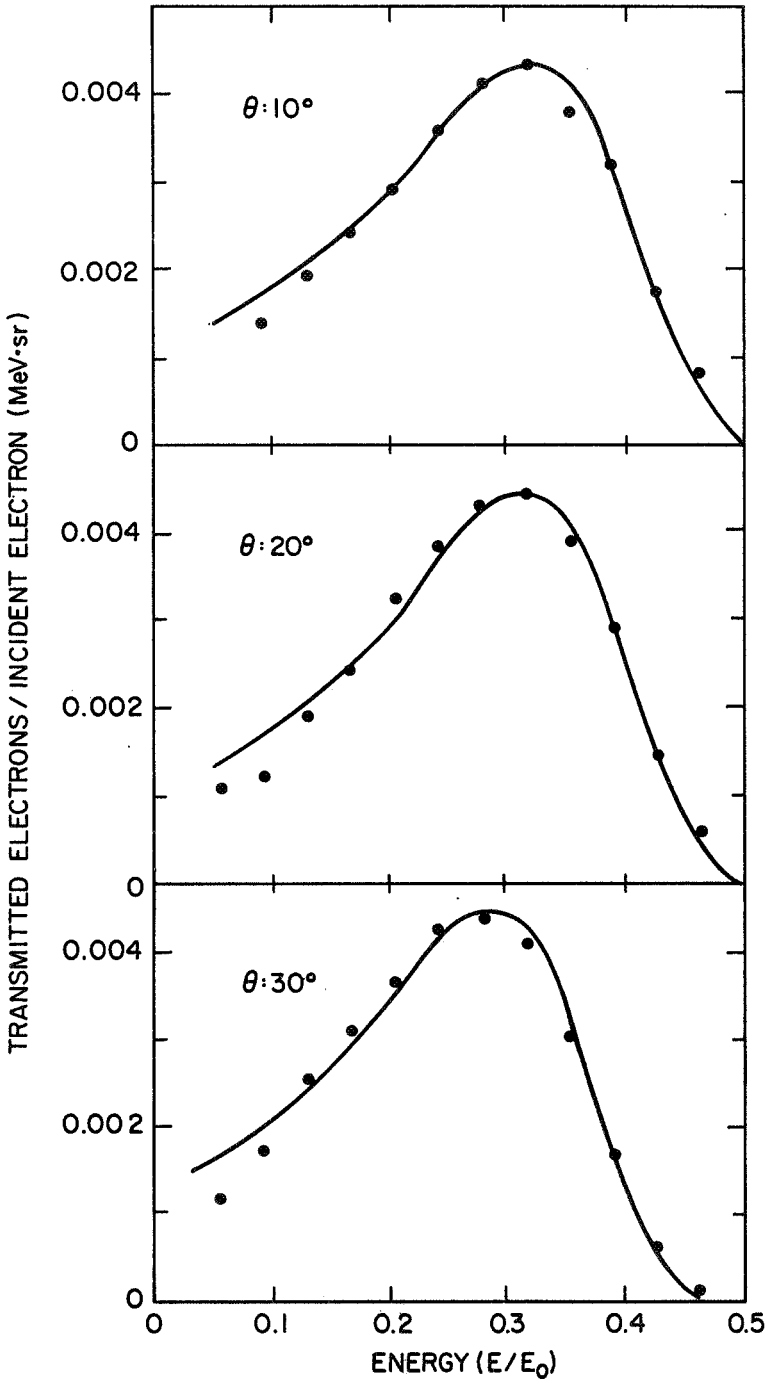

Fig. 13. Spectra at 10°, 20°, and 30° of straggled electrons emitted from 3.29 g/cm^2 thick tin target bombarded by 8.0 MeV electrons. The solid curve is the Landau function fitted to the data points.

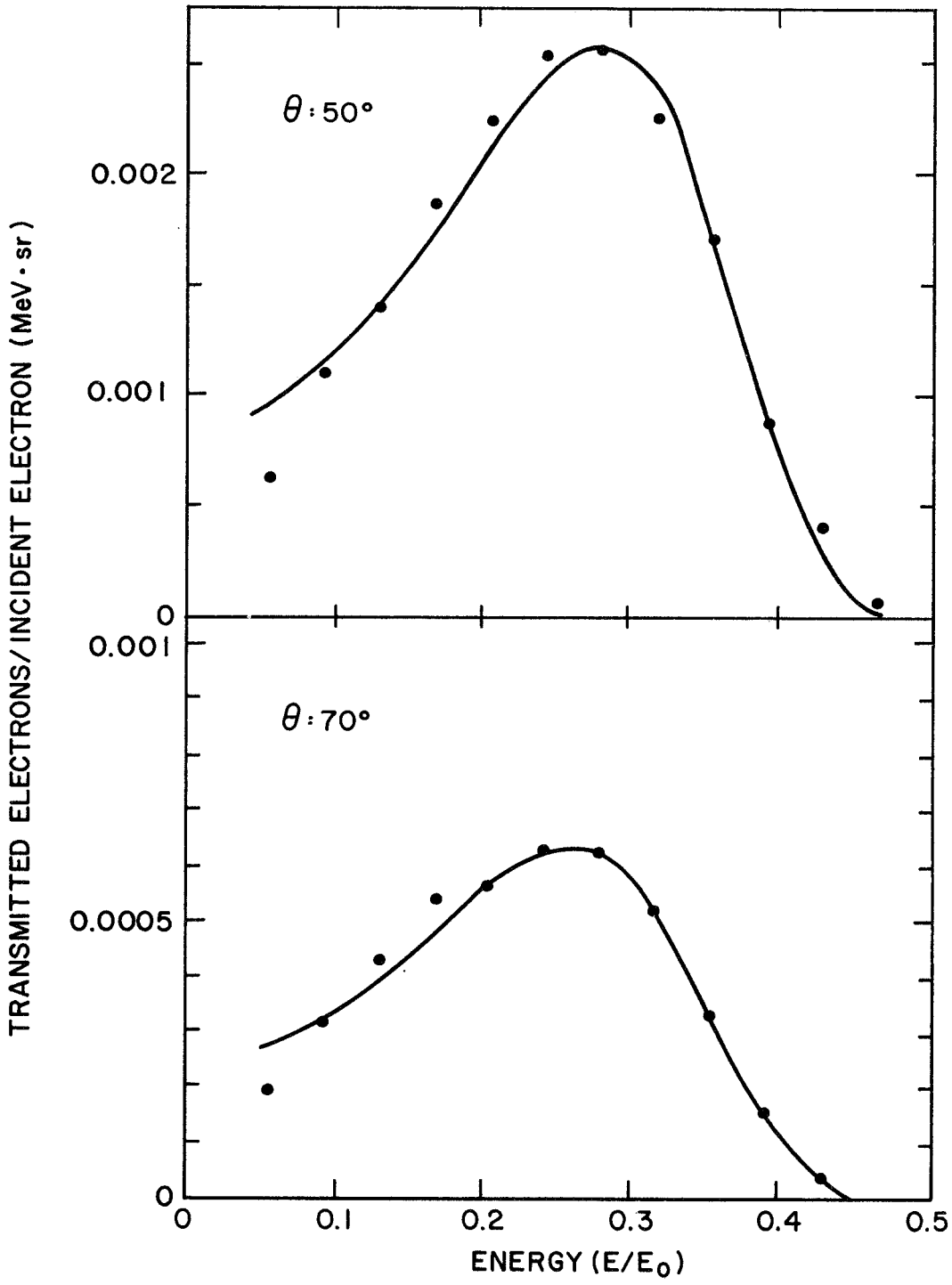

Fig. 14. Spectra at 50° and 70° of straggled electrons emitted from 3.29 g/cm^2 thick tin target bombarded by 8.0 MeV electrons. The solid curve is the Landau function fitted to the data points.

Table 7

EXPERIMENTAL DATA FOR 8.0 MeV ELECTRONS INCIDENT ON 3.29 g/cm^2 THICK Sn TARGET

θ / E/E_o	Transmitted Electrons/Incident Electron-(MeV-sr)				
	10^o ($\times 10^{-3}$)	20^o ($\times 10^{-3}$)	30^o ($\times 10^{-3}$)	50^o ($\times 10^{-3}$)	70^o ($\times 10^{-3}$)
0.055	----	1.08	1.21	0.62	0.20
0.092	1.38	1.21	1.75	1.10	0.32
0.129	1.92	1.94	2.54	1.40	0.43
0.165	2.44	2.44	3.11	1.87	0.54
0.202	2.94	3.27	3.65	2.26	0.56
0.239	3.59	3.84	4.25	2.55	0.63
0.276	4.18	4.28	4.35	2.57	0.63
0.312	4.38	4.41	4.03	2.24	0.53
0.349	3.84	3.81	3.01	1.73	0.34
0.386	3.22	2.92	1.68	0.88	0.16
0.423	1.78	1.46	0.63	0.40	0.044
0.460	0.90	0.57	0.13	0.07	-----

Table 8

ν	1	2	3	4
$C\nu$	0.174	0.058	0.019	0.007
$\lambda\nu$	0.0	3.0	6.5	11.0
$\gamma\nu$	1.8	2.0	3.0	5.0

The least squares fit to the data was accomplished by a computer program which adjusted the parameters Emp, Sw, and N such that χ^2(Emp, Sw, N) of the following was a minimum.

$$\chi^2(\text{Emp, Sw, N}) = \sum_{i=1} \left[yi - N\varphi\left(\frac{1.4\{\epsilon_i - E_{mp}\}}{S_w}\right)\right]^2 \quad , (11)$$

where yi is the number of transmitted electrons with energy ϵ_i. The energy ϵ_i is in units of E/E_o, E_o is the incident energy, and E is the measured energy.

The results of the calculations for these are given in Tables 9 and 10. The above procedure was equally successful in fitting the data obtained earlier in the program[6] for Al, Be, and Au. This functional representation permits a useful and compact presentation of the data. It is also useful for obtaining empirical straggling formulae.

In Figs. 15 through 19 the angular distribution of electrons transmitted through various target thicknesses is plotted for the two electron energies used. The errors for each point are a combination of:

1. Statistical counting errors (2%)
2. Uncertainty in the transmission coefficient (2%)
3. Uncertainty in integration procedure (2%)

Table 9

Incident Energy: 8.0 MeV

Target Thickness: 1.02 g/cm^2 (Sn)

Angle	10°	20°	30°	40°	50°
Sw(E/E_o)	0.049	0.049	0.049	0.049	0.059
Emp(E/E_o)	0.84	0.84	0.84	0.82	0.82

Incident Energy: 8.0 MeV

Target Thickness: 3.29 g/cm^2 (Sn)

Angle	10°	20°	30°	50°	70°
Sw(E/E_o)	0.096	0.091	0.092	0.093	0.1
Emp(E/E_o)	0.31	0.30	0.27	0.27	0.25

Incident Energy: 8.0 MeV

Target Thickness: 2.42 g/cm^2 (Sn)

Angle	10°	20°	30°	50°	70°
Sw(E/E_o)	0.085	0.095	0.092	0.099	0.098
Emp(E/E_o)	0.59	0.58	0.55	0.54	0.51

Table 10

Incident Energy: 4.0 MeV

Target Thickness: 1.47 g/cm^2 (Sn)

Angle	10^o	20^o	30^o	40^o	50^o	60^o	70^o
$Sw(E/E_o)$	0.10	0.10	0.097	0.093	0.96	0.096	0.13
$Emp(E/E_o)$	0.49	0.50	0.48	0.46	0.45	0.44	0.39

Incident Energy: 4.0 MeV

Target Thickness: 0.595 g/cm^2 (Sn)

Angle	5^o	10^o	20^o	30^o	40^o	50^o
$Sw(E/E_o)$	0.054	0.052	0.058	0.061	0.057	0.064
$Emp(E/E_o)$	0.84	0.84	0.83	0.82	0.81	0.80

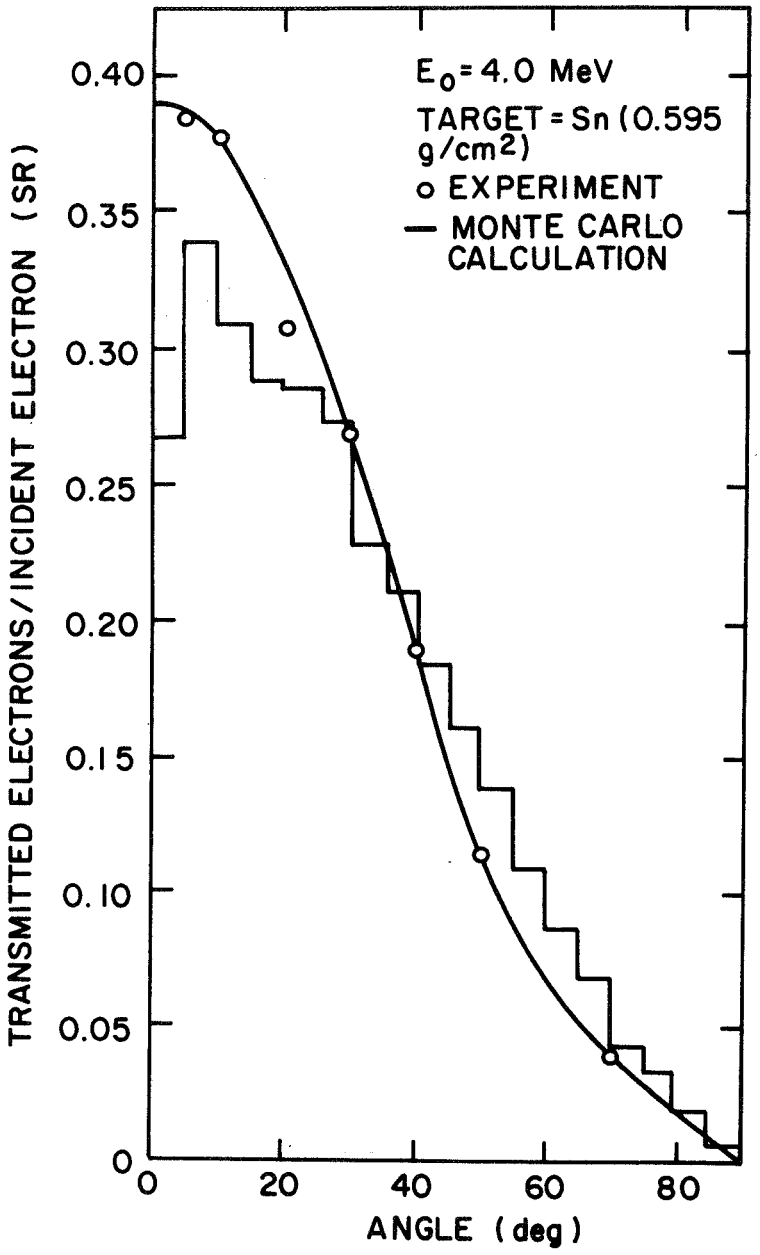

Fig. 15. Angular distribution of electrons emitted from a 0.595 g/cm^2 thick tin target (0.2 range c.s.d.a.) bombarded by 4.0 MeV electrons. The histogram is a Monte Carlo calculation generated with ETRAN 15. There were 20,000 histories run.

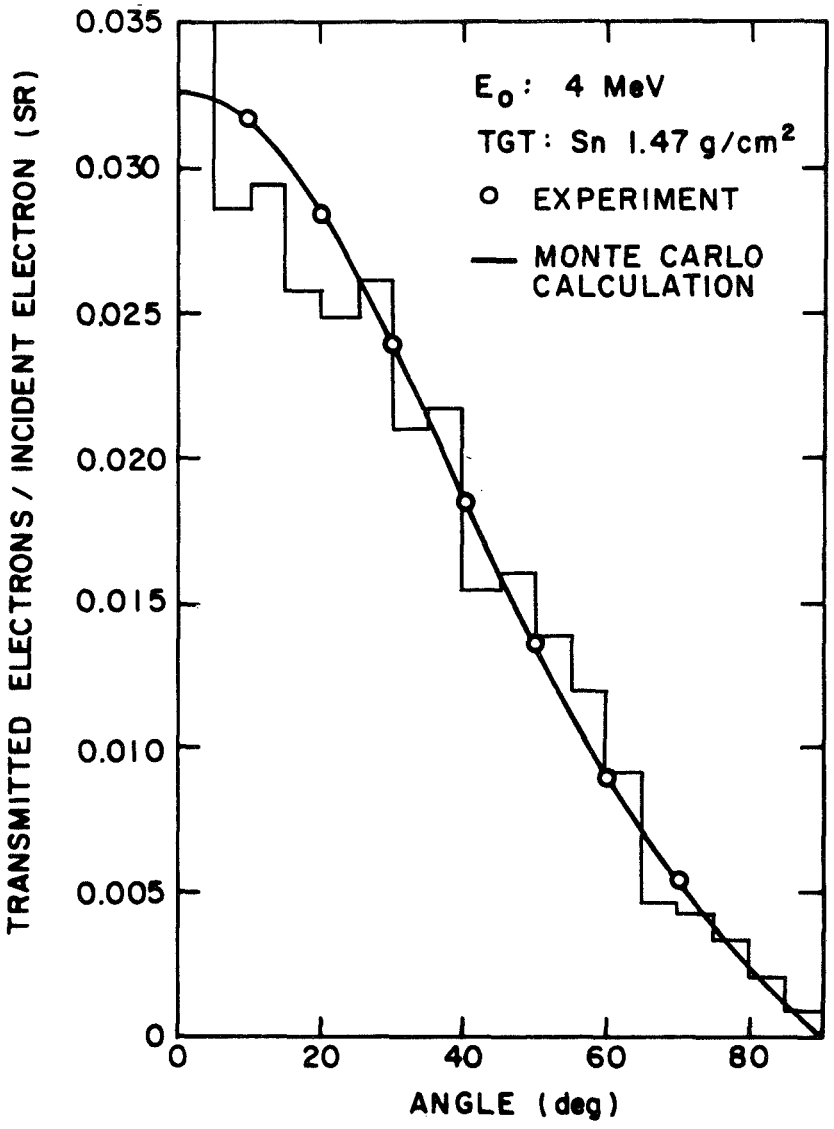

Fig. 16. Angular distribution of electrons from a 1.47 g/cm^2 thick tin target (0.5 range c.s.d.a.) bombarded by 4 MeV electrons. The histogram was generated by ETRAN 15, a Monte Carlo computer program. The calculations have been renormalized to experimental transmission coefficients.

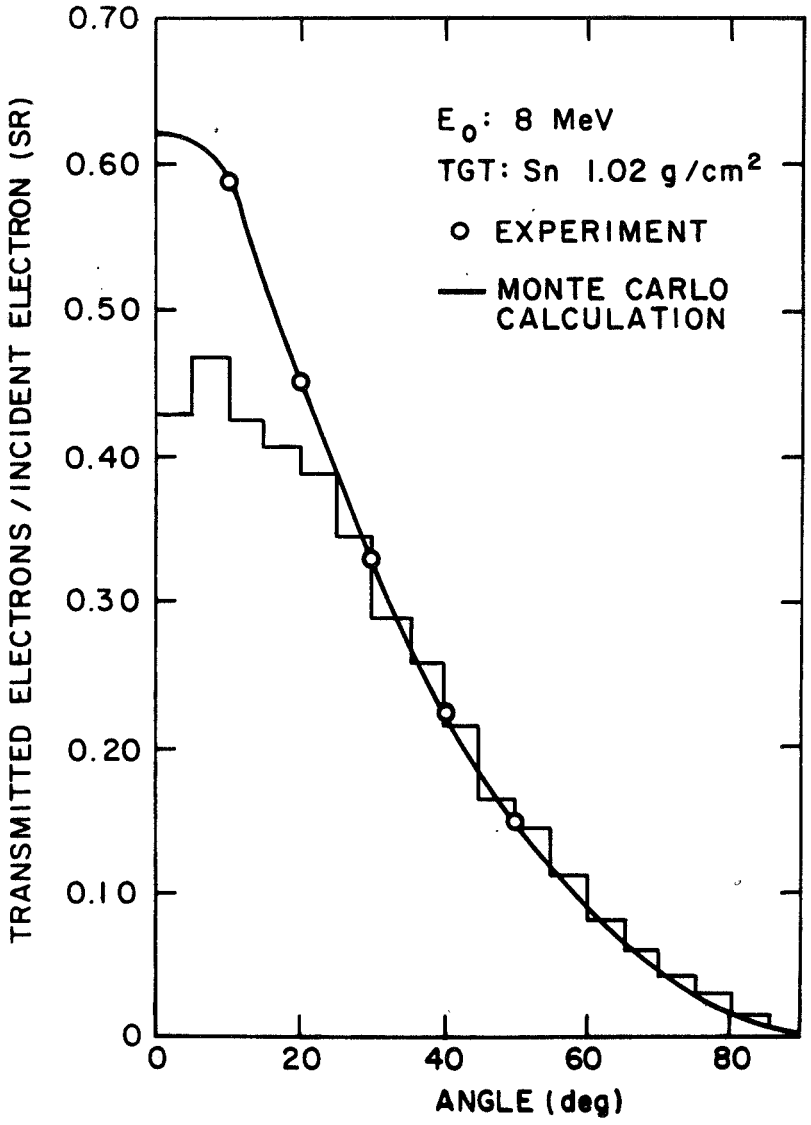

Fig. 17. Angular distribution of electrons emitted from a 1.02 g/cm^2 thick target of tin (0.2 range c.s.d.a.) bombarded by 8.0 MeV electrons. The Monte Carlo calculation is by ETRAN 15.

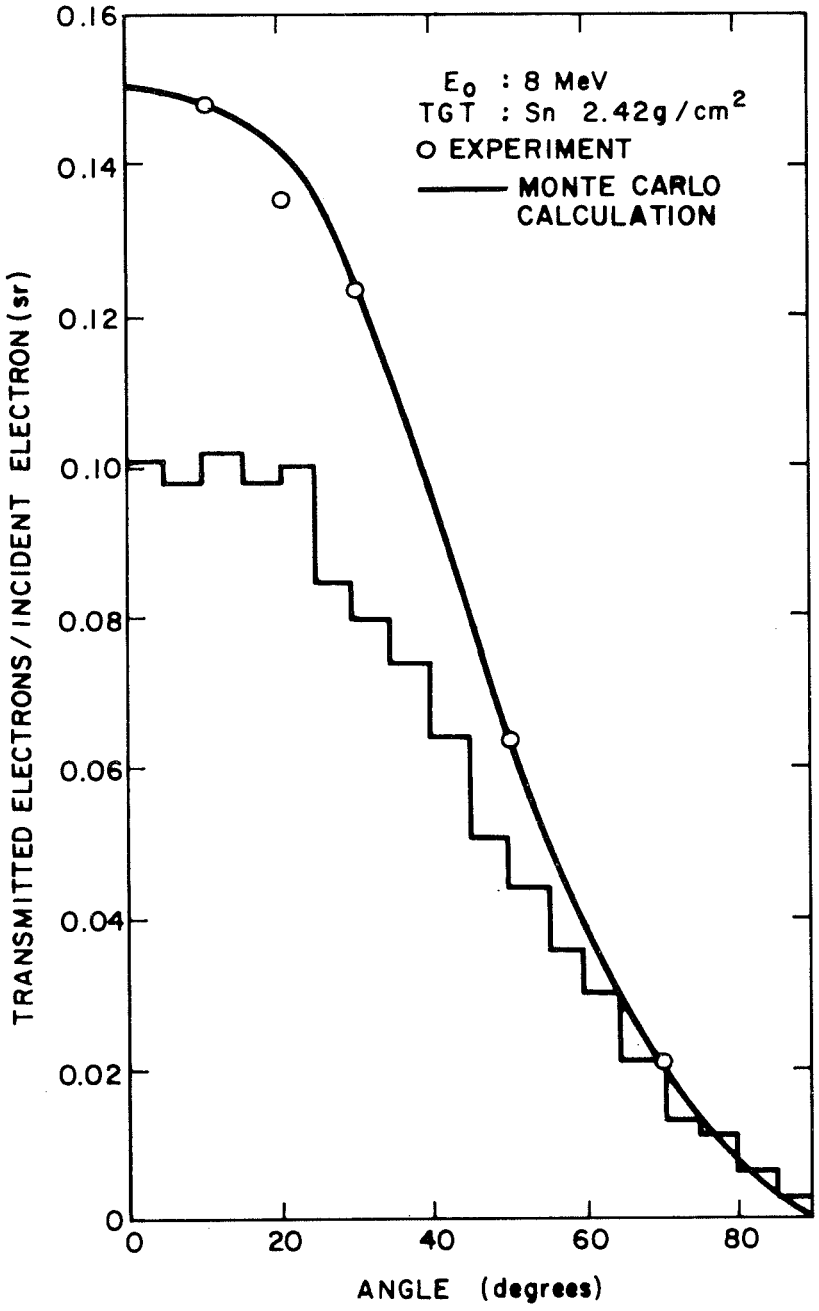

Fig. 18. Angular distribution of electrons emitted from a 2.42 g/cm^2 thick tin target (0.5 range c.s.d.a.) bombarded by 8.0 MeV electrons.

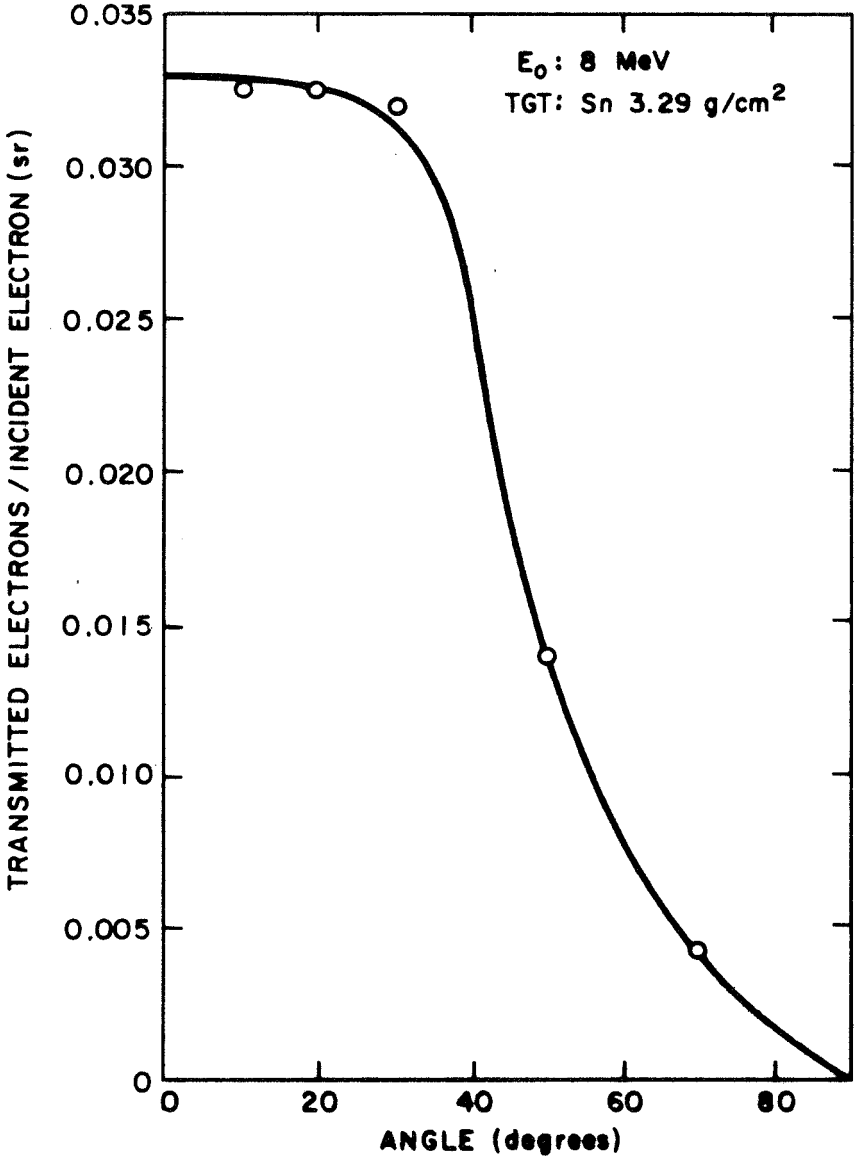

Fig. 19. Angular distribution emitted from 3.29 g/cm^2 thick tin target (0.65 range c. s. d. a.) bombarded by 8.0 MeV electrons

4. Background due to bremsstrahlung (1%)

5. Pile-up (1.5%).

The total error from these independent sources is 4 percent. A smooth curve has been drawn through the points as an aid to interpolation. In Figs. 15, 16, and 17 histograms are plotted which are the results of a Monte Carlo calculation. The ETRAN 15 code[1] was used to generate 20,000 electron histories in tin. Computer runs were made at 4.0 and 8.0 MeV. Boundaries corresponding to three target thicknesses were selected; angular distribution and energy spectra of transmitted electrons were then calculated. The code also calculated the transmission coefficients listed in Table 2. The agreement is within the statistical uncertainty in all cases except for the 1.47 g/cm^2 thick target at 4.0 MeV. The Monte Carlo calculation gives a value for F which is 1.55 times that measured by Ebert.[8] This sort of discrepancy has been previously observed[6] and appears to correspond to a tendency for the code to overestimate the range of the electrons. The calculated distributions were reduced by a factor of 1/1.55 before they were compared with the experiment in Fig. 16. This was done so that a shape comparison could be made more easily.

Shape comparison of the measured and calculated angular distributions indicates that the calculated angular spreading is greater by a small but measurable amount than the experimental results for the target thicknesses corresponding to 0.2 range (c.s.d.a.). The calculations agree well within the statistical uncertainties with the experiments for the 0.5 range c.s.d.a. target at 4.0 MeV.

Energy spectra at selected angles are plotted in Figs. 20 through 22. The data points have the same uncertainty associated with them as the angular distribution points, with one exception. The statistical errors in the energy spectra are larger; they are 3 percent for the peak points and up to 20 percent for the end points. The errors are attributed to the

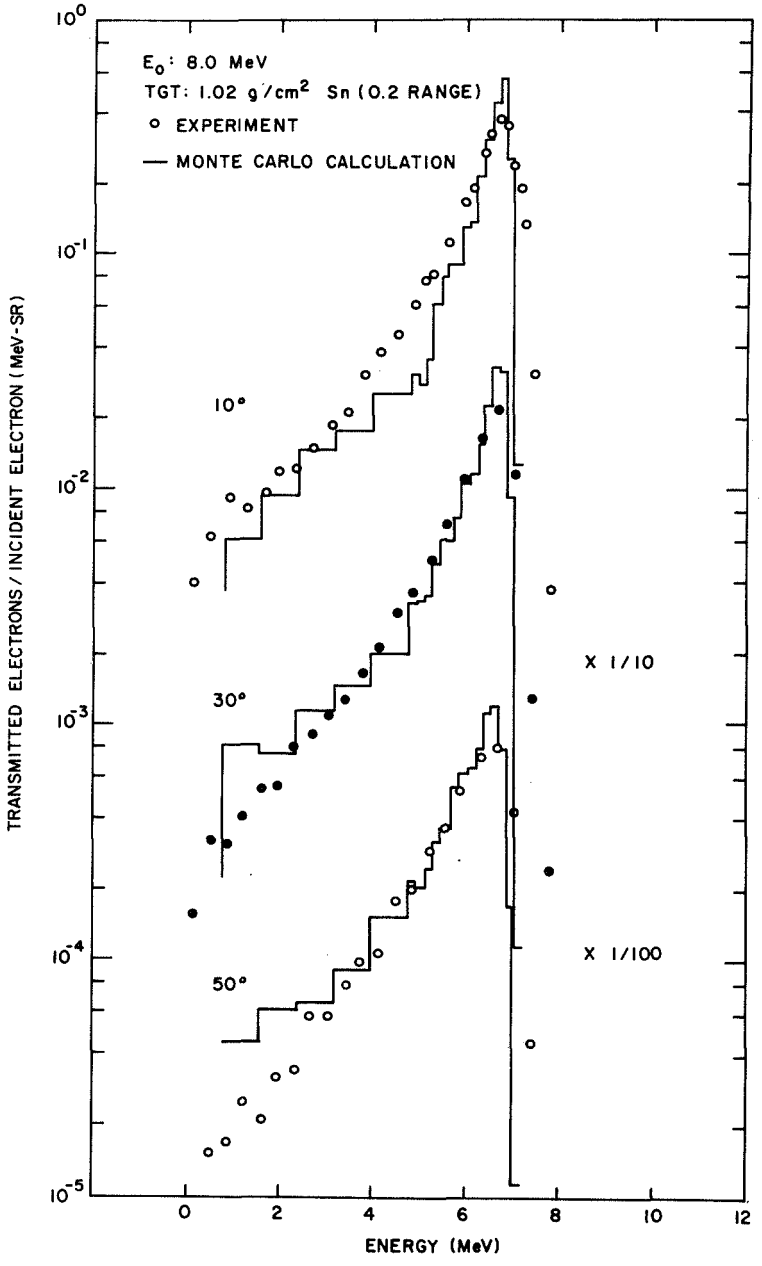

Fig. 20. Energy spectrum of straggled electrons emitted at 10°, 30°, and 50° from a 1.02 g/cm^2 thick (0.5 range c.s.d.a.) tin target bombarded by 8.0 MeV electrons. The histogram was generated by ETRAN 15, a Monte Carlo computer code.

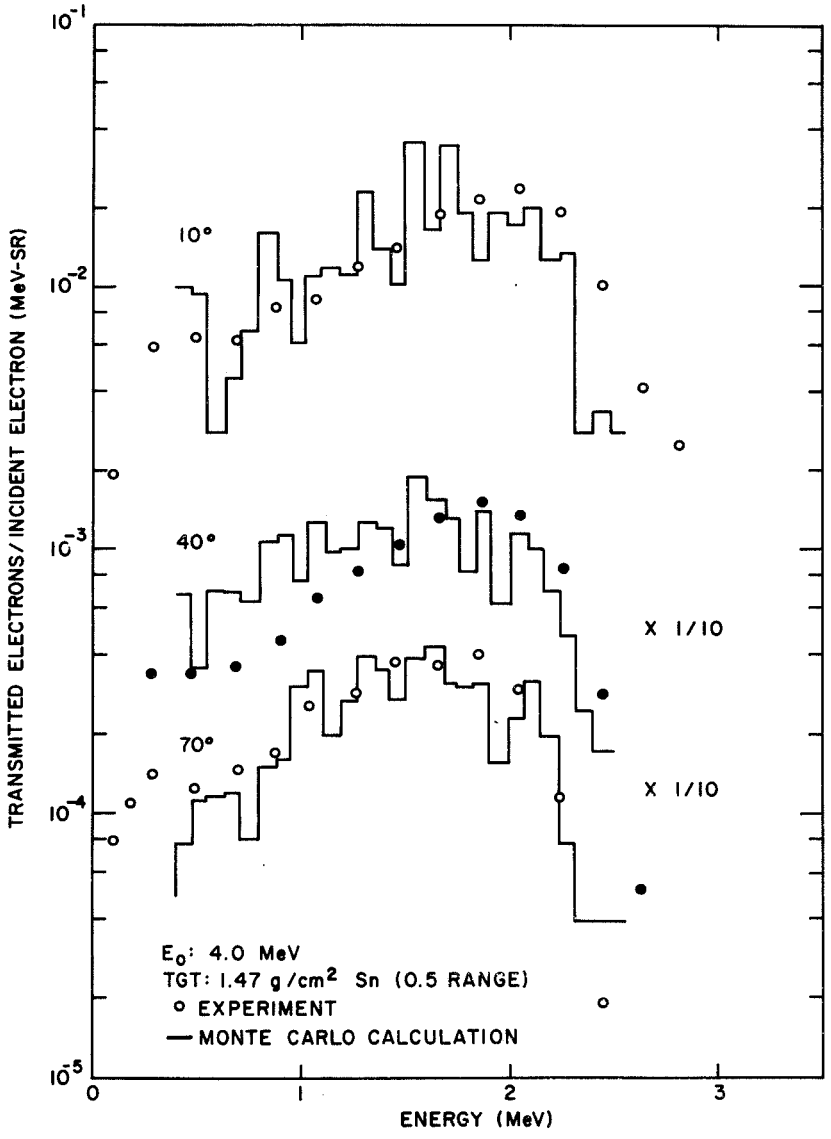

Fig. 21. Energy spectrum of straggled electrons emitted at 10°, 40°, and 70° from a 1.47 g/cm^2 thick (0.5 range c.s.d.a.) tin target bombarded by 4.0 MeV electrons. The calculations were renormalized to experimental transmission coefficients.

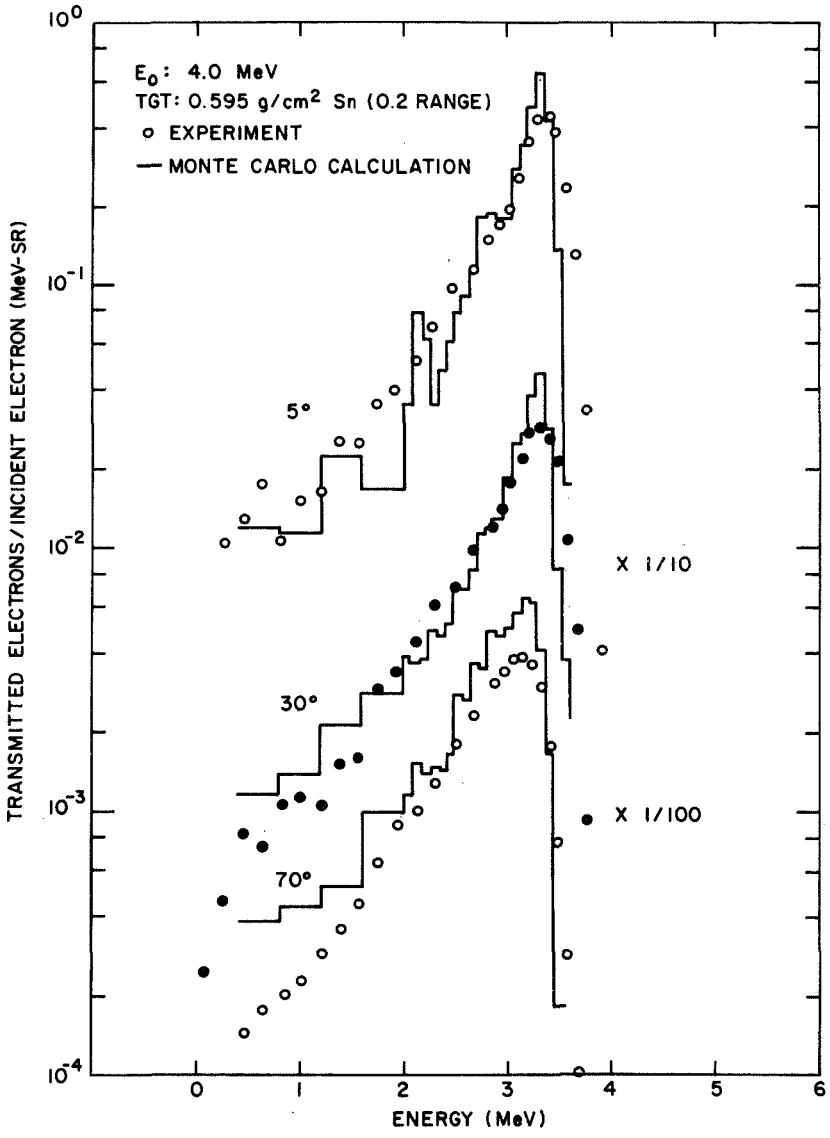

Fig. 22. Energy spectrum of straggled electrons emitted at 5°, 30°, and 70° from a 0.595 g/cm^2 thick (0.2 range c.s.d.a.) tin target bombarded by 4.0 MeV electrons. The histogram was generated by ETRAN 15, a Monte Carlo computer code.

normalization procedure which carry over to the energy spectra. In addition to these uncertainties there is a broadening of the energy spectra due to the response of the spectrometer which was not unfolded from the data.

The results are compared with histograms generated in the Monte Carlo calculations mentioned above. Again the calculated results for the 1/2 range c. s. d. a. target at 4. 0 MeV have been renormalized to the measured transmission coefficients. In all cases the calculations agree with the experimental results. The fact that the measured spectra appear broader in the peak than the calculated spectra can be entirely attributed to the detector response. The low energy tail of the calculated spectra seems to be higher on the average than those observed in the experiments. This may be real but no firm conclusion can be drawn without better statistical accuracy in the calculation.

In Fig. 23 the angles necessary to define the oblique angle of incidence results are depicted. Measurements were made at two incident energies; 4 and 8 MeV and with two-target orientation at each energy. In one configuration ($\beta = 0^{\circ}$, $\varphi = 30^{\circ}$) the normal to the plane of the target was in the plane defined by the beam axis and the detector (plane A). In the other configuration ($\beta = 45^{\circ}$, $\varphi = 0^{\circ}$) the plane defined by the normal to the target plane and the beam axis is perpendicular to plane A. The targets used at each energy corresponded in thickness to 1/2 the range of the incident electrons (for normal incidence), they were 1. 47 and 2. 42 g/cm^2 thick. Each point in the distribution corresponds to the energy spectra measured at that angle integrated over energy. The relative errors in each point are the same as described for the normal incidence data and result in a combined error of 4 percent. The error in normalization, that is, the uncertainty in the ordinate scale of figures is 10 percent.

The angular distributions measured in the configuration: $\beta = 45^{\circ}$, $\varphi = 0^{\circ}$ (Figs. 24 and 25) are very similar in shape to those measured with the beam normally incident on the same target. The half-maximum

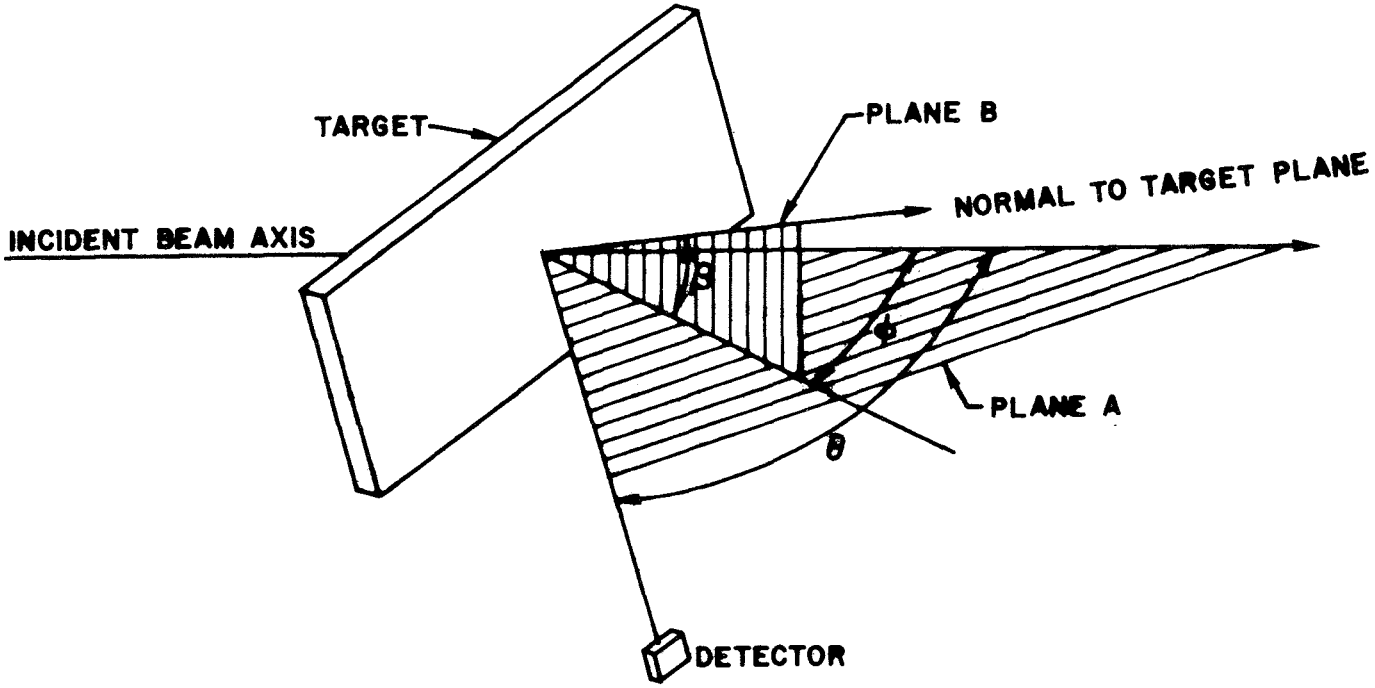

Fig. 23. A diagram showing the angles used to specify the orientation of the target and detector for the non-normal incident measurements.

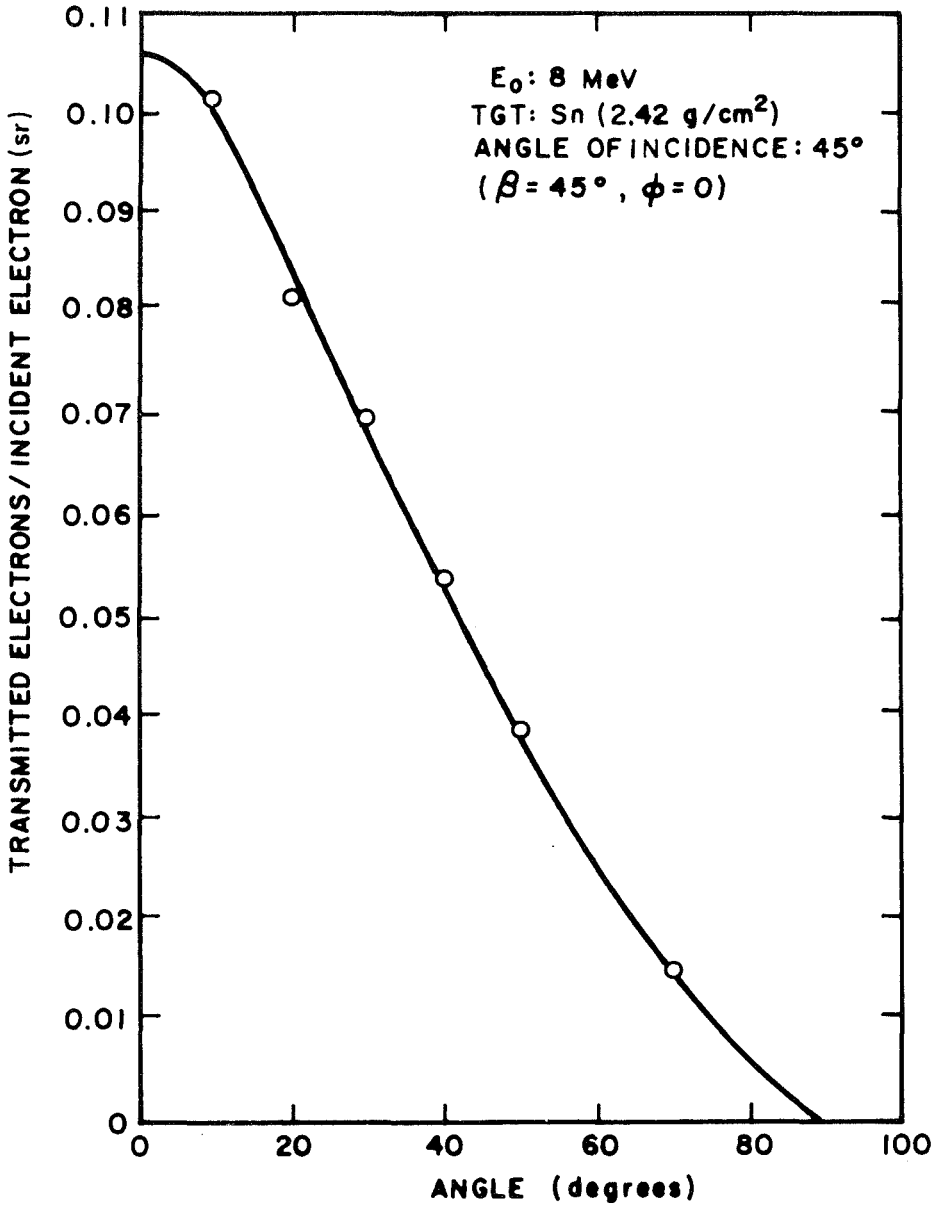

Fig. 24. Angular distribution of electrons emitted from a 2.42 g/cm^2 thick tin target bombarded by 8.0 MeV electrons at an angle of incidence of 45°. The orientation angles are β = 45°, φ = 0°.

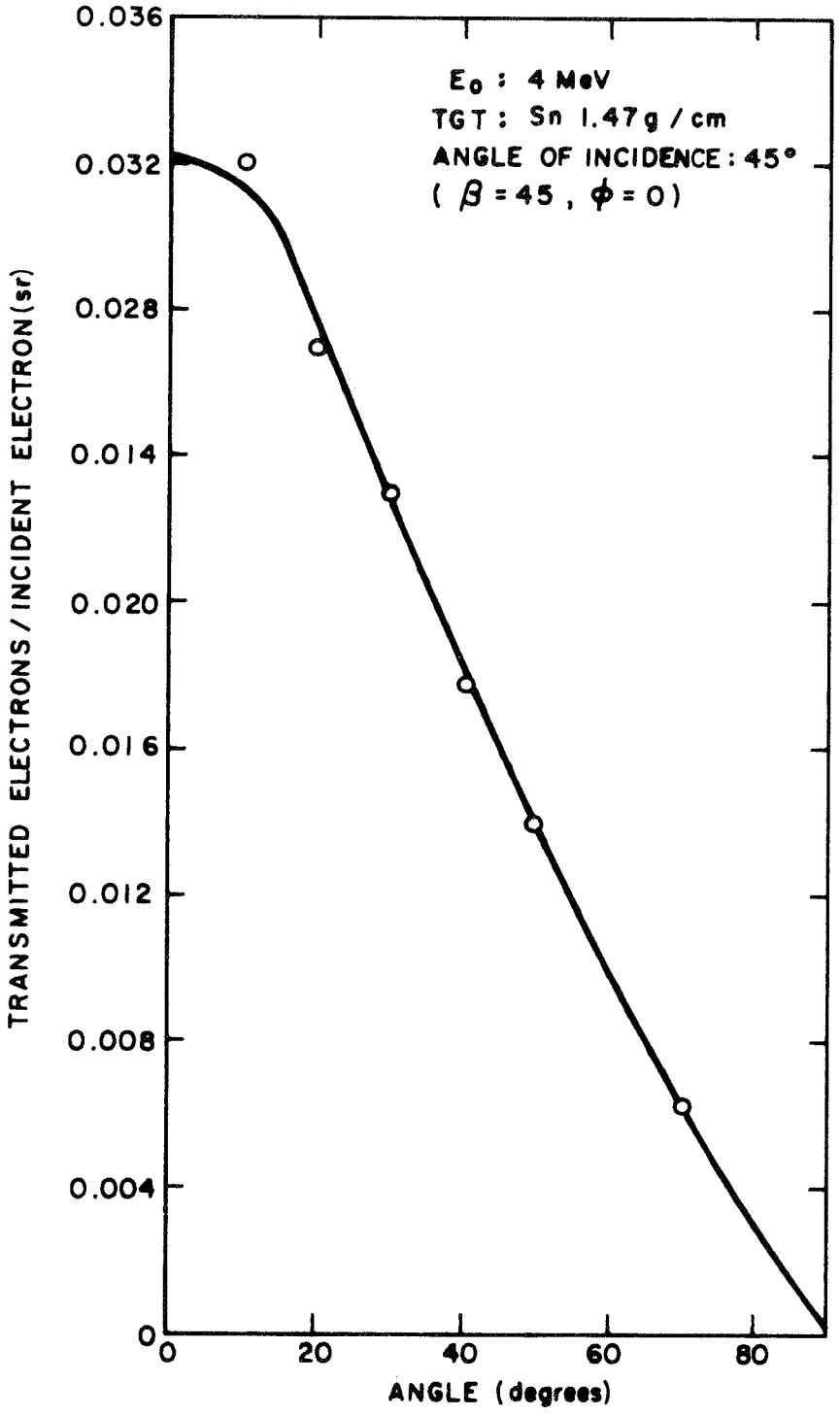

Fig. 25. Angular distribution of electrons emitted from a 1.47 g/cm^2 thick tin target bombarded by 4.0 MeV electrons at an angle of incidence of 45°. The orientation angles are $\beta = 45^\circ$, $\varphi = 0^\circ$.

point occurs at about 40° in each case. The angular distributions measured in the configuration: $\beta = 0^{\circ}$, $\varphi = 30^{\circ}$ (Figs. 26 and 27) show an almost perfect symmetry about the normal to the target plane (30°). There appears to be very little peaking about the incident beam direction (0°). Evidently the electrons emerging from the back surface have had their direction altered enough times while passing through the target that they emerge at the closest boundary without regard to their initial direction of motion. This symmetry is indicated less strongly in Fig. 28 where the most probable energy loss is plotted versus angle. Each point corresponds to the difference between the incident energy and the peak energy of the emission spectrum. The scatter in points reflects the uncertainty with which this peak can be defined.

3.2 THICK TARGET BREMSSTRAHLUNG MEASUREMENTS

The energy spectra were obtained from the pulse-height data by an unfolding procedure using the LSMUN code developed by Carl Young at LASL.[12] This code has two main functions: In the first one the response matrix characteristic of the detector is generated, which is subsequently used in the second part in which the energy spectrum is calculated.

The code calculates a response matrix G(I, J) composed of 200 vectors of 200 channels each. Each vector (J) represents the response of the detector to a gamma ray of energy E_J with the energy mesh corresponding to that of the input data.

The shapes of the vectors are determined on the basis of built-in response equations whose parameters were generated by fitting the response curves to measured pulse-height distributions. The response vectors, J, are finally normalized to the photopeak efficiencies at energies E_J so that the unfolded answer will be the absolute spectrum for the experimental geometry.

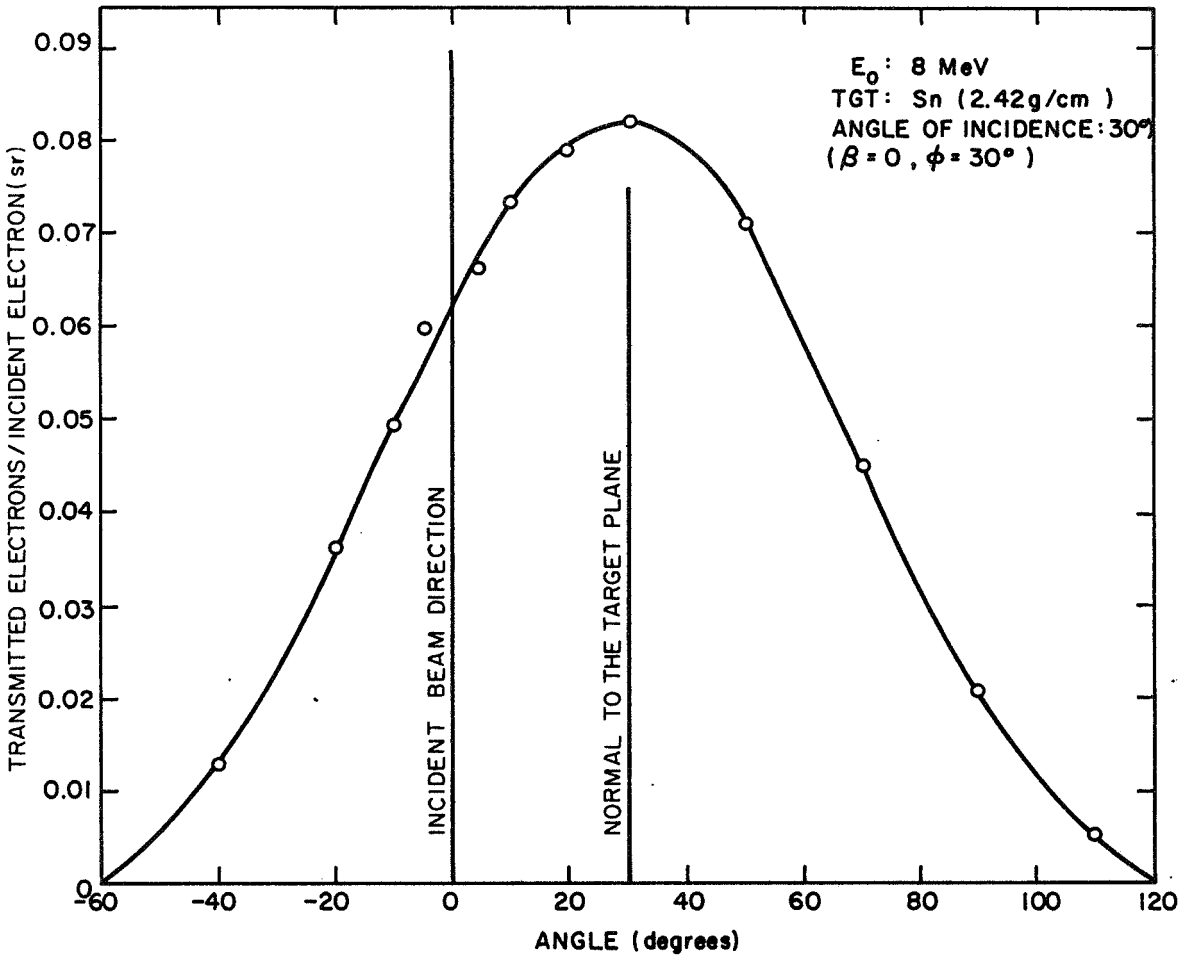

Fig. 26. Angular distribution of electrons emitted from a 2.42 g/cm^2 thick tin target bombarded by 8.0 MeV electrons at an angle of incidence of 30°. The orientation angles are $\beta = 0^\circ$, $\varphi = 30^\circ$.

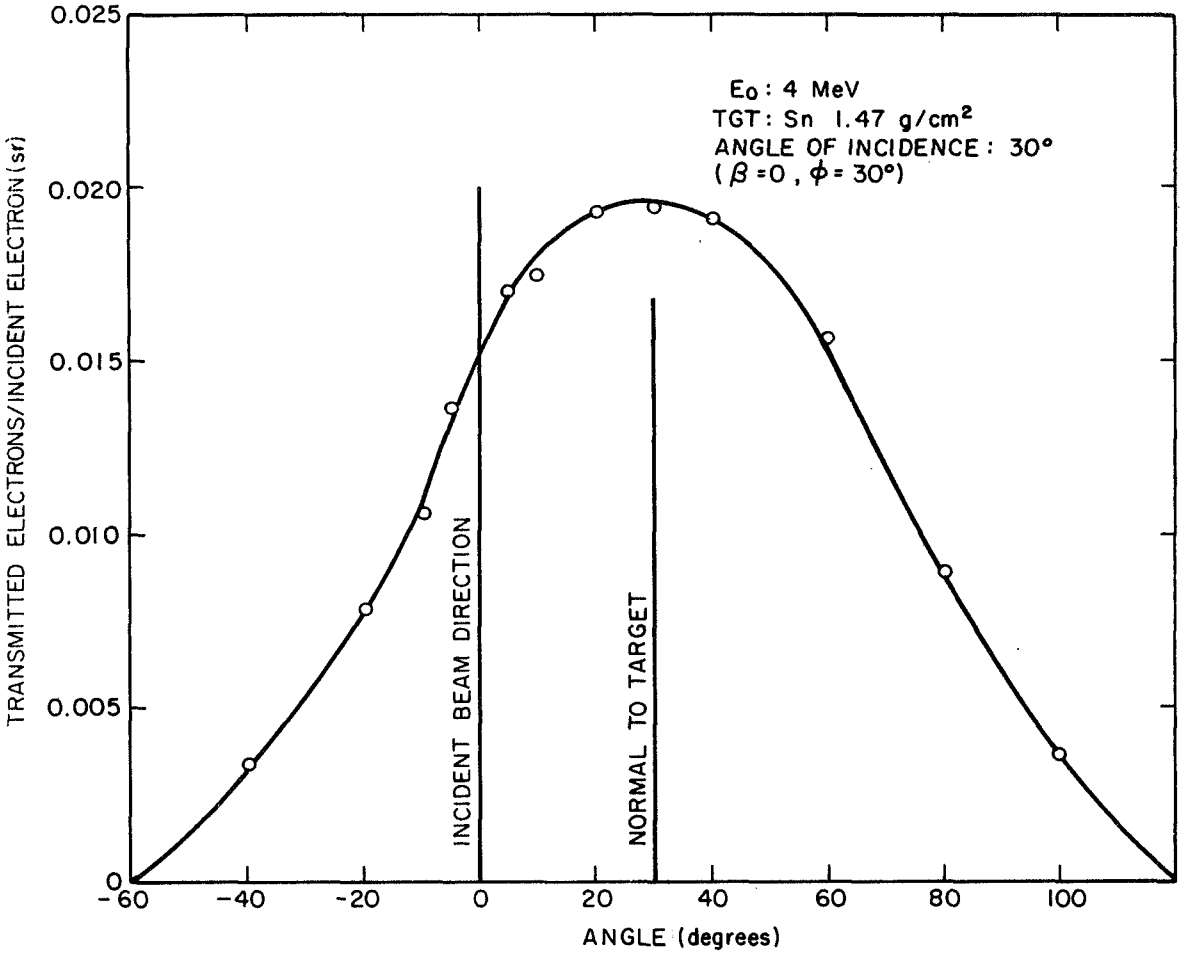

Fig. 27. Angular distribution of electrons emitted from a 1.47 g/cm^2 thick tin target bombarded by 4.0 MeV electrons at an angle of incidence of 30°. The orientation angles are $\beta = 0°$, $\varphi = 30°$.

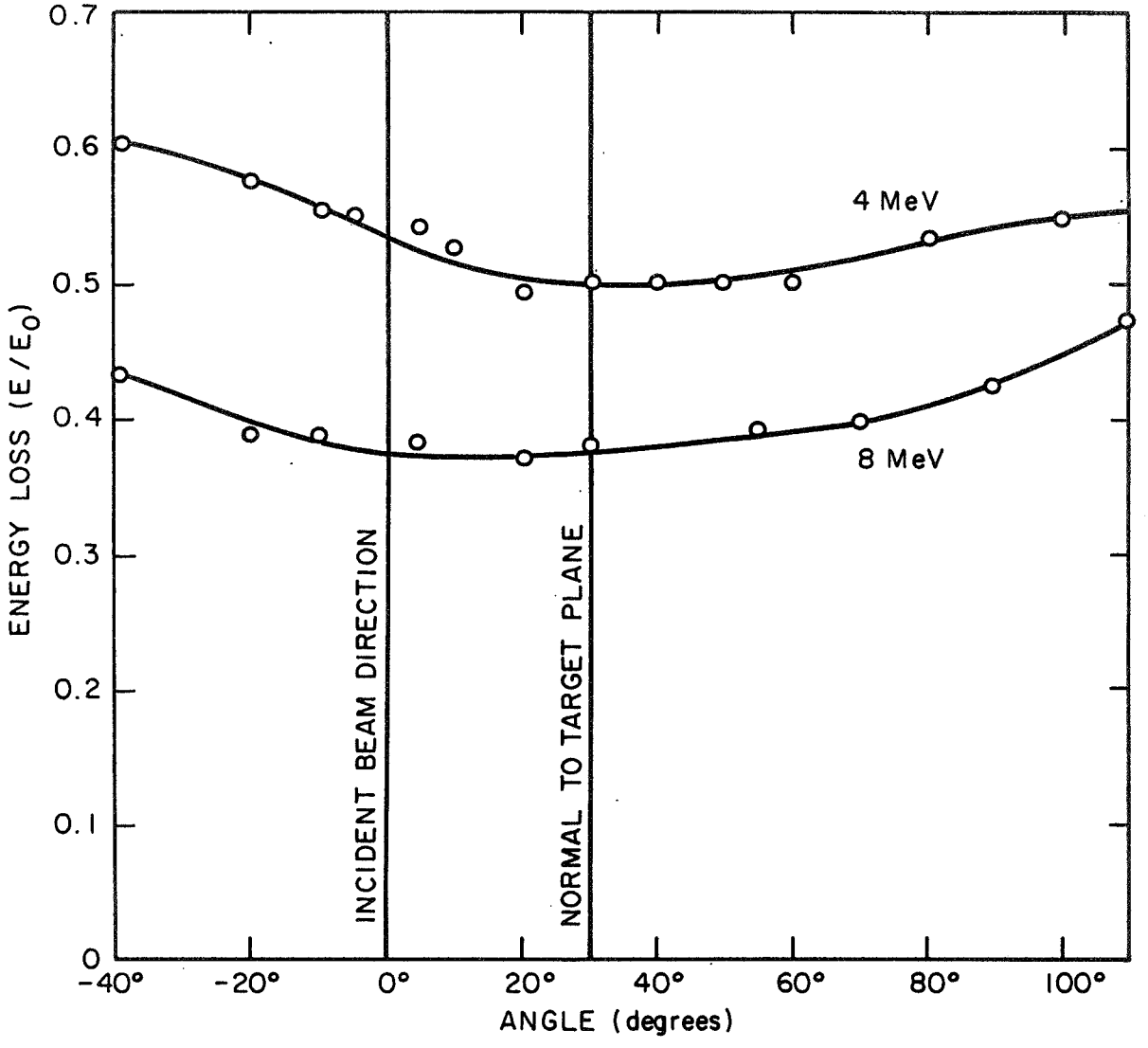

Fig. 28. Most probable energy lost in target oriented so the angle of incidence is 30° ($\beta = 0^{\circ}$, $\varphi = 30^{\circ}$). The incident beam energies are 4.0 and 8.0 MeV and the target thicknesses are 1.47 g/cm^2 and 2.42 g/cm^2.

Since the Compton plateau was found to be flat for this detector, its response equation is that of a horizontal line with exponential cutoffs at either end. Its height relative to the area of the corresponding photopeak is energy dependent and is given by the parameter

$$AMC = 0.291 \times (E)^{-0.1875} \quad . \tag{12}$$

The photopeak, as well as the escape peaks, are described as Gaussian-shaped with a standard deviation of

$$SIGMA = 0.0397 \times (E)^{0.586} \quad . \tag{13}$$

The height of the single-escape peak is given by a parameter which is the ratio of the areas of single escape peak over photopeak:

$$\text{For } E > 1.022 \text{ MeV } AMES = 0.2 \times (1 - \cos(0.25 \times E)) - 0.0064 \quad . \tag{14}$$

The height parameter for the double-escape peak, the ratio of the areas of single over double escape peak, is given as

$$A2ES = 0.655 \times \log(0.4 \times E) \text{ for } E > 2.5 \text{ MeV} \quad . \tag{15}$$

The normalization to photopeak efficiencies is performed by calculating the area under each of the 200 photopeaks and normalizing it to its respective full energy peak efficiency. This automatically normalizes each of the 200 vectors since all parameters are functions of the photopeak area.

The absolute full-energy peak efficiency, the product of intrinsic efficiency and photofraction, was put into the code as an 11-point table with an energy range from 0.1 to 10 MeV. A linear interpolation scheme on a log-log scale is used to extrapolate between the points in the table.

The unfolding is essentially the implementation of a paper by B. C. Cook[13] on applying a least structure smoothing technique to the problem of interpreting oscillating solutions. In more exact notation, given a data vector y, an energy vector x, and the response matrix $\underline{\underline{G}}$, the relationship between the three quantities is

$$\underline{y} = \underline{\underline{G}} \cdot \underline{x} \tag{16}$$

The exact solution to the problem of finding $\underline{x}$ for nonsingular $\underline{\underline{G}}$ becomes

$$\underline{x} = \underline{\underline{G}}^{-1} \cdot \underline{y} \quad . \tag{17}$$

Unfortunately $\underline{x}$ will oscillate violently unless the response matrix is known with much greater precision than can be claimed for this experiment where a limited number of measured gamma-ray spectra had to suffice to establish the set of response parameters and functions as functions of photon energy. Thus smoothing of some sort has to be applied. Also, lacking knowledge of the "true" response matrix, a unique true solution cannot be found. Consequently the problem is not only that of finding a solution, but of making it meaningful by applying some smoothing and selecting an acceptable solution among the possible ones.

B. C. Cook points out one method of achieving this complex goal. He demands that the input data be left untouched since small distortions in $\underline{y}$ may show up as large nonsignificant deviations in $\underline{x}$. Instead all smoothing is to be applied to $\underline{x}$ only in a completely numerical fashion so that the amount of smoothing becomes nonarbitrary and the distortion it introduces can be estimated unequivocally.

The smoothing is accomplished by a structure function $S(x_i^{\lambda})$ the exact definition of which is arbitrary to a certain extent. Whether a solution $\underline{x}^{\lambda}$ is acceptable as well as the distortion due to smoothing is estimated on the basis of a comparison between the input data $\underline{y}$ and the quantity

$$\underline{y}^{\lambda} = \underline{\underline{G}} \cdot \underline{x}^{\lambda} \quad . \tag{18}$$

A statistical quantity χ^2 is defined as

$$\chi^2 = \sum_{i=1}^{n} \frac{\left(\sum_{j=1}^{n} G_{ij} x_j^{\lambda} - y_i \right)^2}{(\Delta y_i)^2} \quad , \tag{19}$$

where n is the number of channels over which $\underline{y}$ and $\underline{x}^{\lambda}$ extend and Δy_i is the error on y_i.

An acceptable smooth (or least structure) solution is a solution $\underline{x}^{\lambda}$ which minimizes $S(x_i^{\lambda})$ with the constraint that $\chi^2 \approx n$. This is a variational problem which can be solved as

$$\lambda \delta (x_i^{\lambda}) + \delta \chi^2 (x_i^{\lambda}) = 0 \tag{20}$$

and can be written as

$$\underline{x}^{\lambda} = \left[\underline{\underline{G}} + \lambda (\underline{\underline{\tilde{G}}})^{-1} \cdot \underline{\underline{W}}^{-1} \cdot \underline{\underline{S}} \right]^{-1} \cdot \underline{y} \quad , \tag{21}$$

where

$\underline{\underline{S}}$ is a smoothing matrix the exact form of which depends on the structure function $S(x_i)$,

y is the input data,

$\underline{x}^{\lambda}$ is the least structure solution for a λ,

$\underline{\underline{W}}$ is a diagonal matrix with elements $W_{ij} = \frac{1}{(\Delta y_i)^2} \delta_{ij}$.

For a given initial value of λ the unfolding process starts by finding $\underline{x}^{\lambda}$ as indicated above. Subsequently $\chi^2(\underline{x}^{\lambda})$ is calculated and depending on how close to n it is a new λ is calculated which in turn determines a new $\underline{x}^{\lambda}$ and $\chi^2(\underline{x}^{\lambda})$. A maximum of eight iterations allows the code to find that solution for which $\chi^2 = n$ approximately.

Figures 29 and 30 show the unfolded energy spectra at 0° from 4 and 8 MeV electrons incident on tin. The unfolded measured spectra are compared to results calculated by Dickinson and Lent.[2] For the 4-MeV case the agreement between the absolute photon yields for the interval 0.365 to 4 MeV is quite good with 0.175 ± 0.009 MeV/steradian-electron for the present data and 0.174 MeV/steradian-electron for the calculated result. The agreement in shape is not as good. This is probably due in part to the fact that the intrinsic bremsstrahlung distribution generated by Schiff and utilized in the code diverges from the true cross section at low energies as well as in the high energy limit. The error bars shown in the unfolded spectrum as well as those shown on all other unfolded spectra represent only the statistical uncertainties explained below. In addition, there are systematic errors which are mostly due to the efficiency calibration of the gamma-ray detector, as discussed above (Section 2.2.1). The calculated results at 0° take into account the finite solid angle under which the target is viewed by the detector.

For the 8-MeV case the agreement between measured and calculated absolute yields is not as good as the 4-MeV case with 1.03 ± 0.05 MeV/steradian-electron measured versus 1.26 MeV/steradian-electron calculated for the energy interval 0.56 to 8 MeV. The discrepancy in shape is similar to that of the 4-MeV case.

Figures 31 through 37 show the unfolded energy spectra for 4 MeV electrons for angles 10°, 20°, 30°, 40°, 50°, 60°, and 70° compared to the results of the ETRAN 15 Monte Carlo calculations by Berger and Seltzer.[1] Again there is a discrepancy in shape between measured

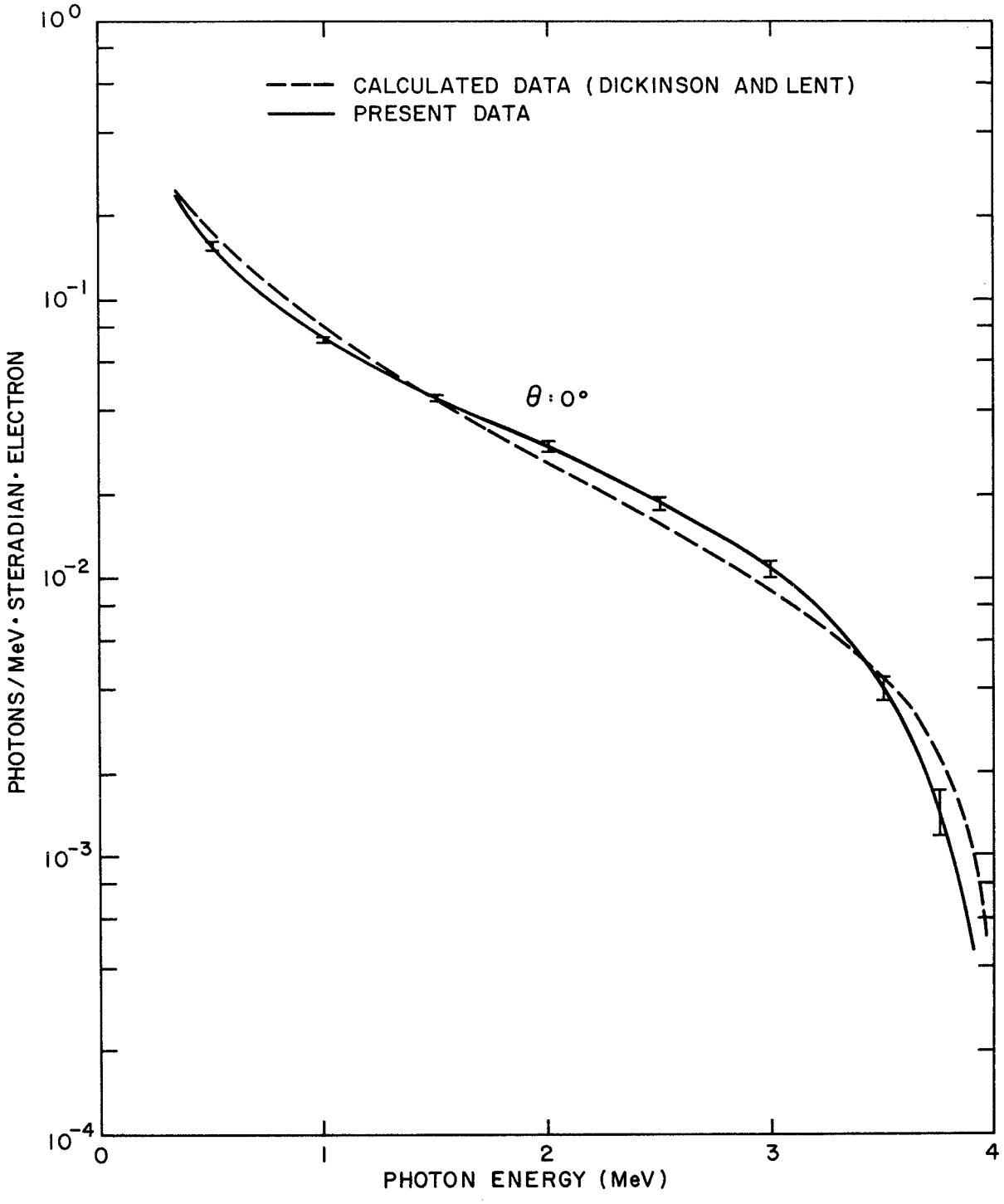

Fig. 29. The unfolded bremsstrahlung energy spectrum at 0° for 4.0 MeV electrons incident on a thick target of tin ($3.29\ g/cm^2$)

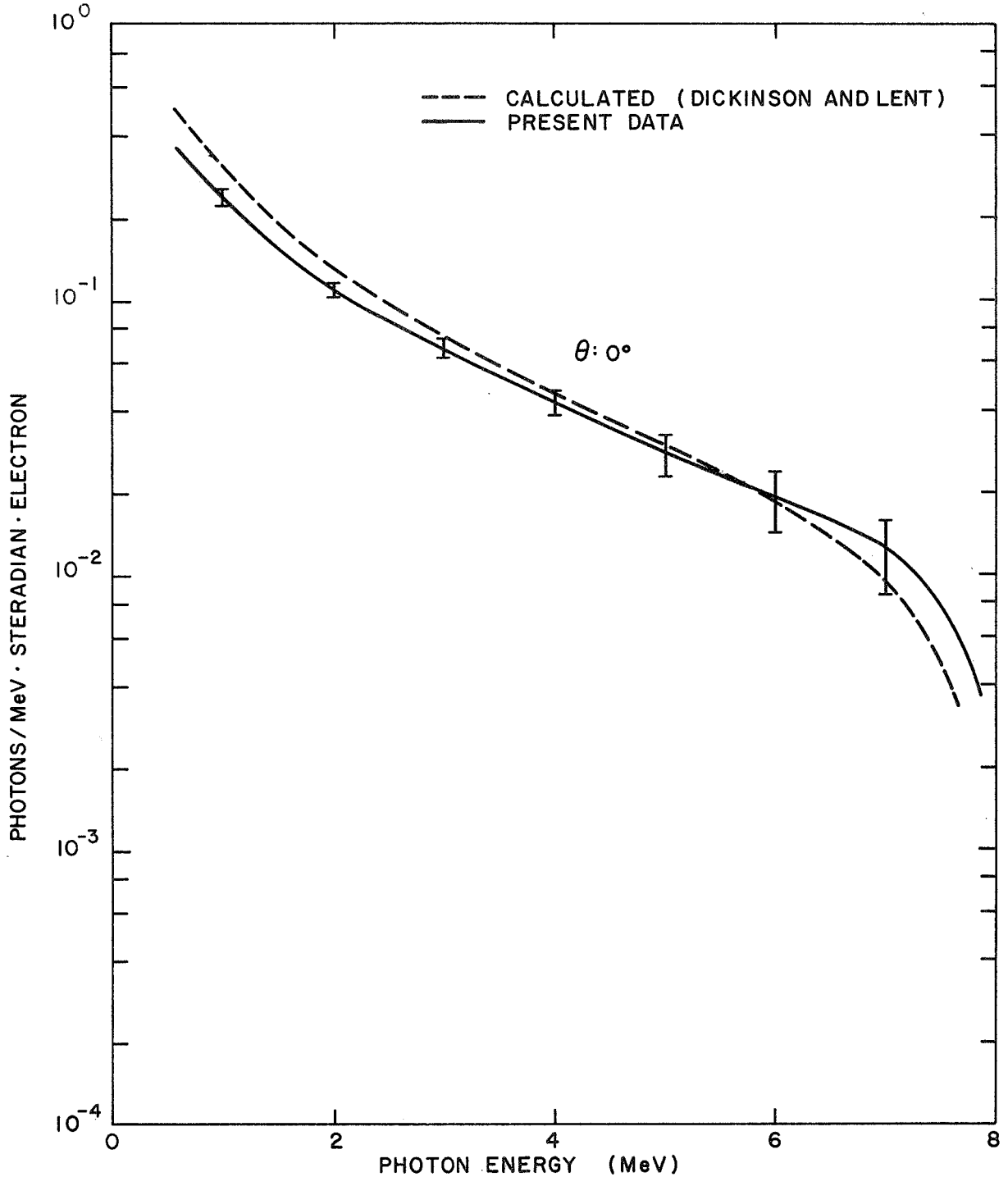

Fig. 30. The unfolded bremsstrahlung energy spectrum at 0° for 8.0 MeV electrons incident on a thick target of tin ($5.84\ g/cm^2$)

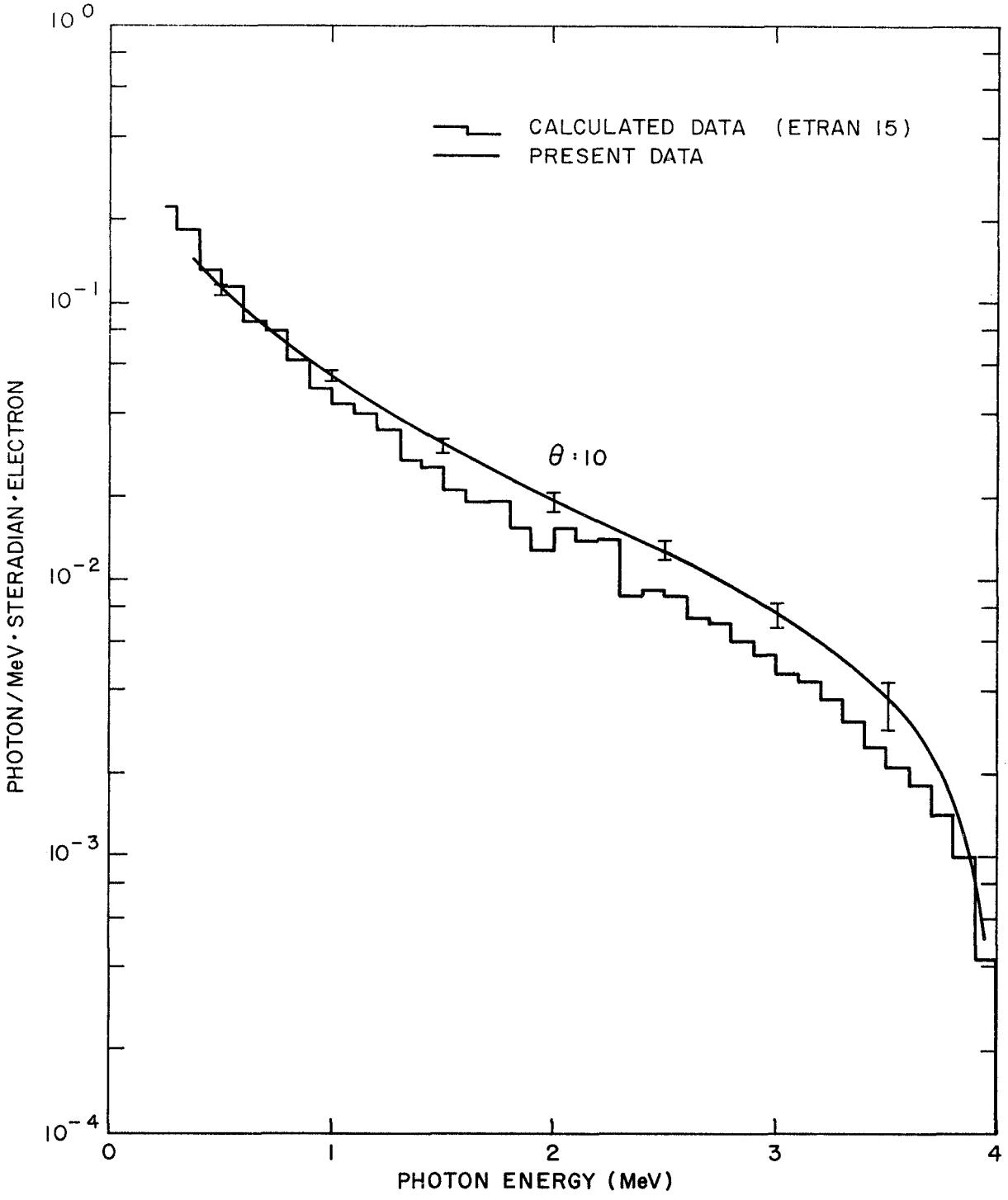

Fig. 31. Comparison between measured and calculated bremsstrahlung spectra at 10^{o} for 4.0 MeV incident electrons on a thick target of tin (3.29 g/cm^2)

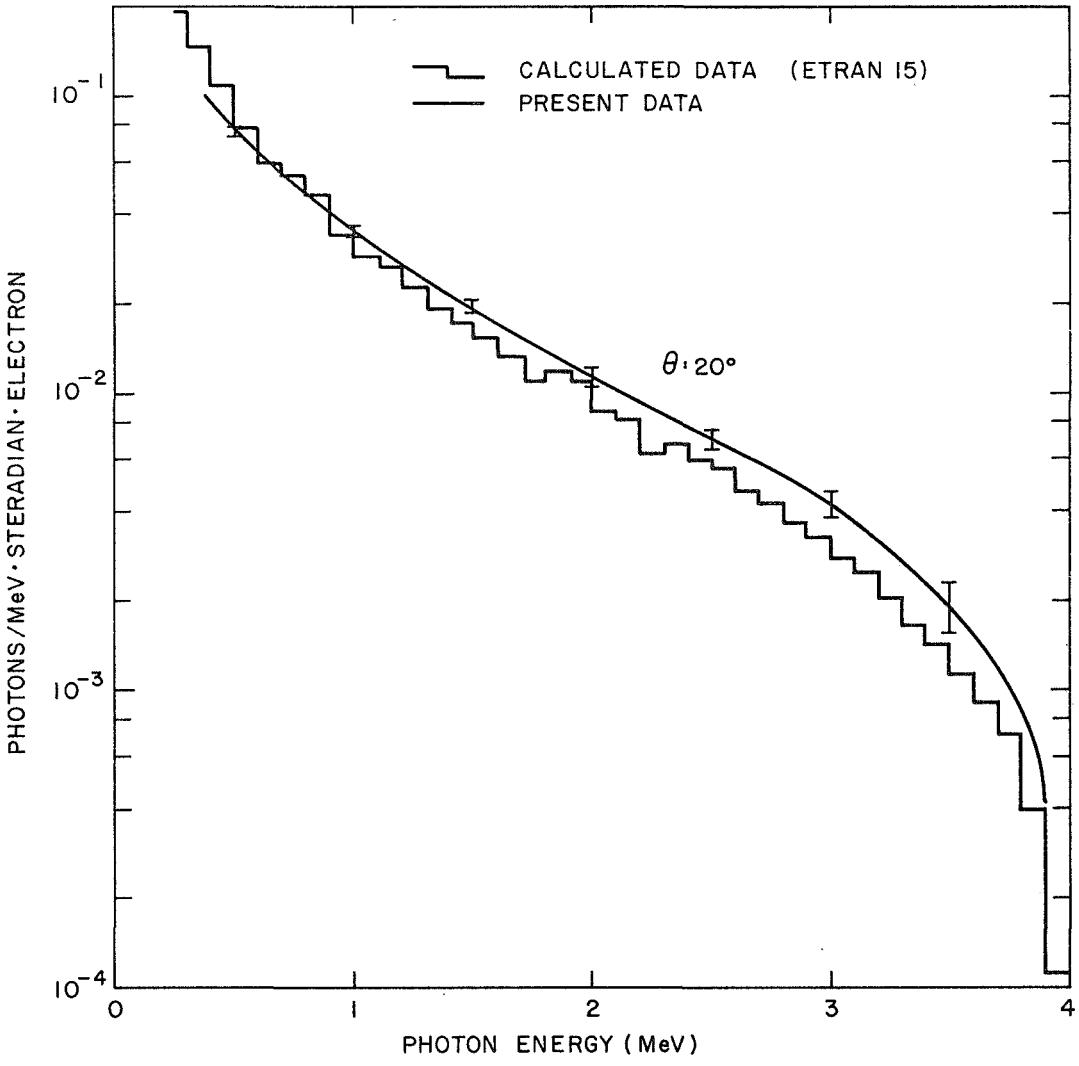

Fig. 32. Comparison between measured and calculated bremsstrahlung spectra at 20^{o} for 4.0 MeV incident electrons on a thick target of tin ($3.29\ g/cm^2$)

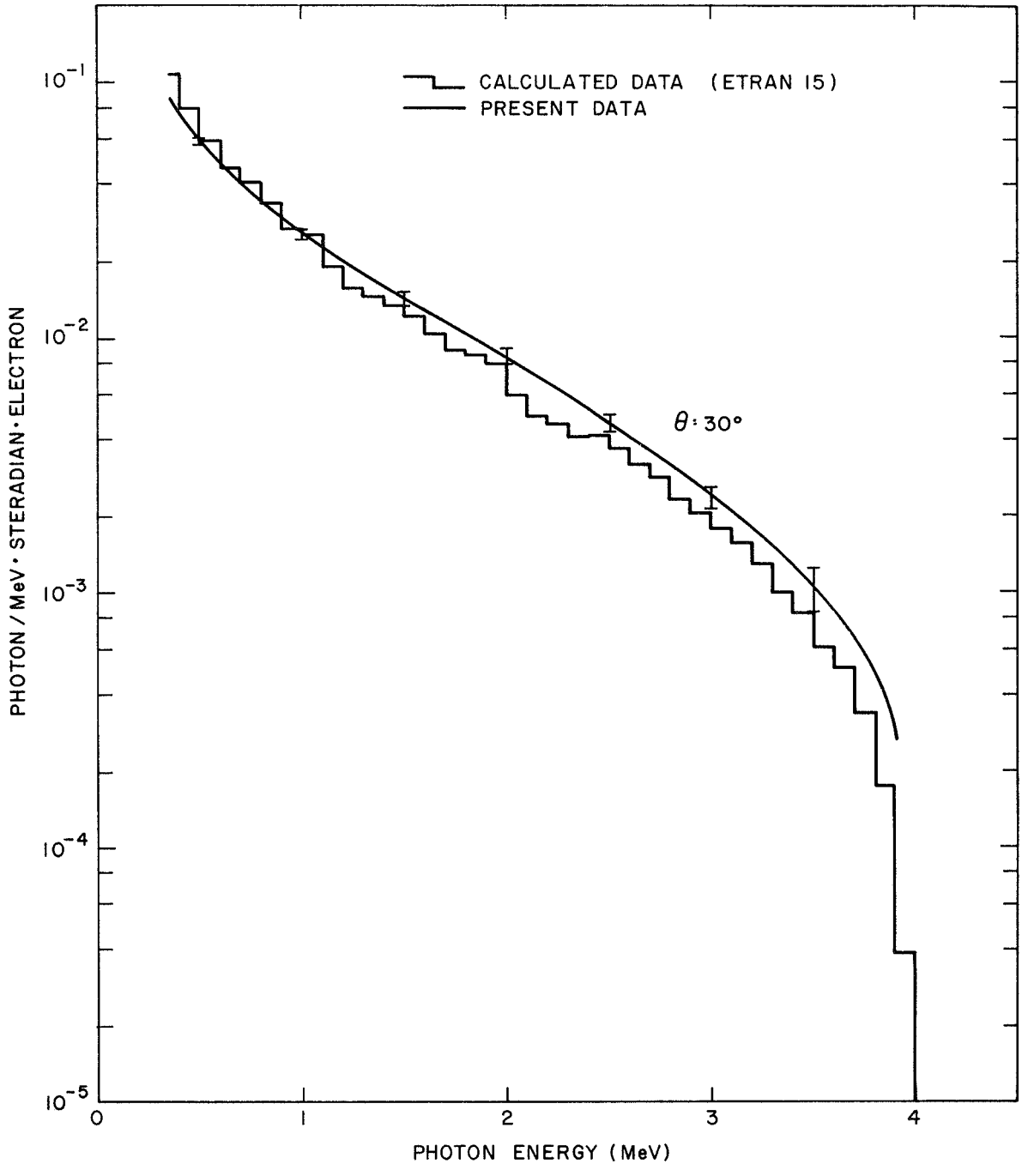

Fig. 33. Comparison between measured and calculated bremsstrahlung spectra at 30^{o} for 4.0 MeV incident electrons on a thick target of tin ($3.29\ g/cm^2$)

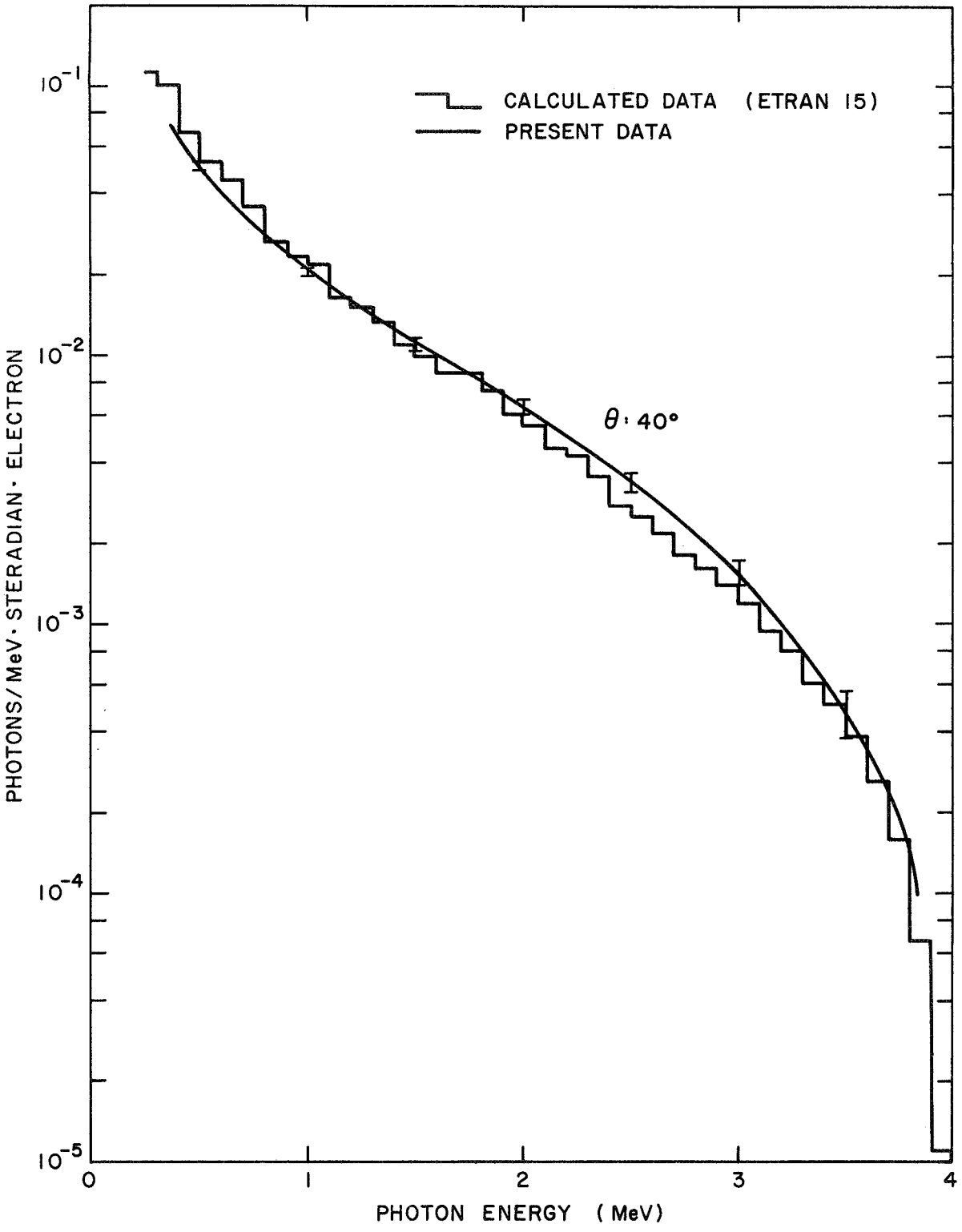

Fig. 34. Comparison between measured and calculated bremsstrahlung spectra at 40^{o} for 4.0 MeV incident electrons on a thick target of tin ($3.29\ g/cm^2$)

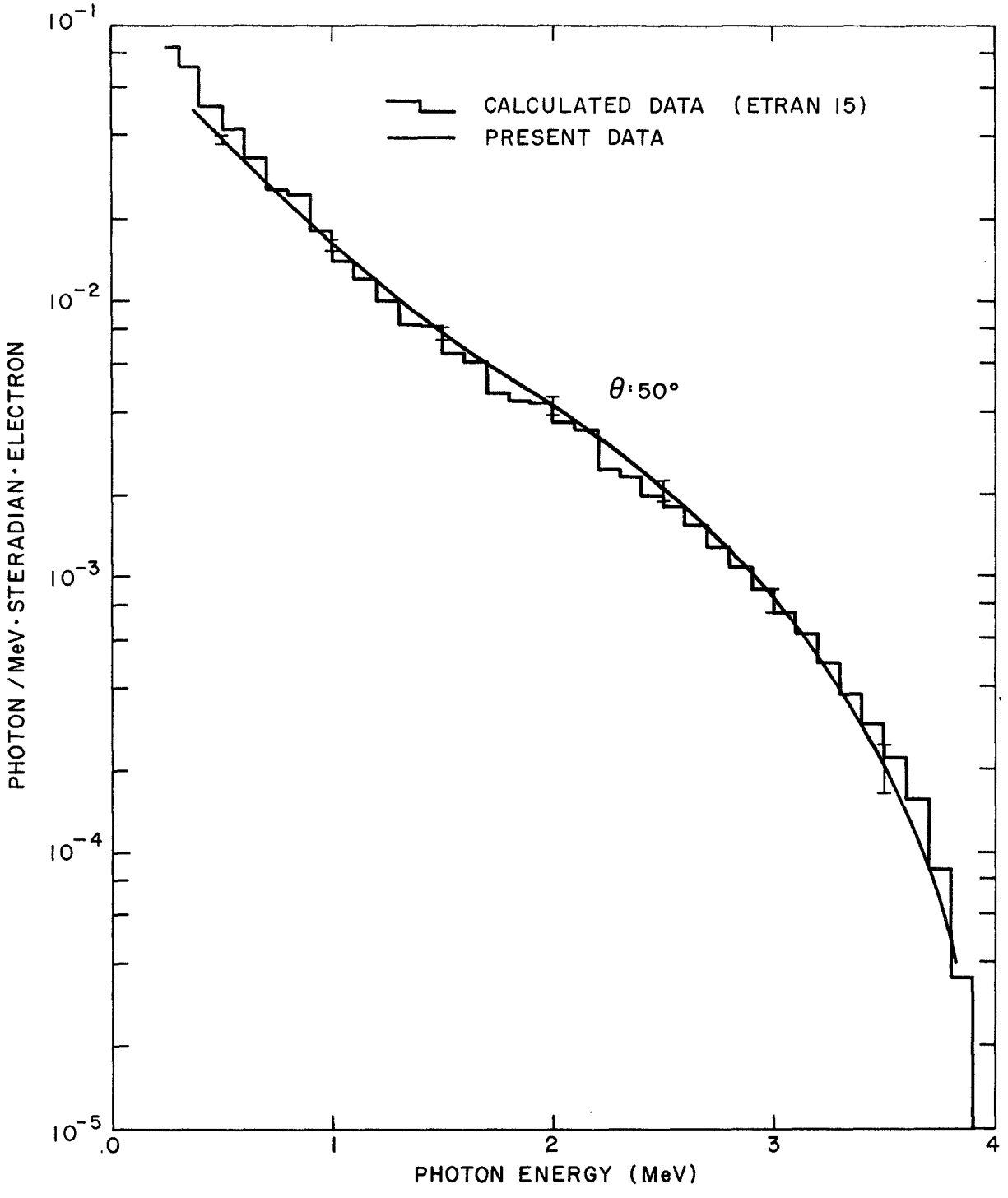

Fig. 35. Comparison between measured and calculated bremsstrahlung spectra at 50^{o} for 4.0 MeV incident electrons on a thick target of tin ($3.29\ g/cm^{2}$)

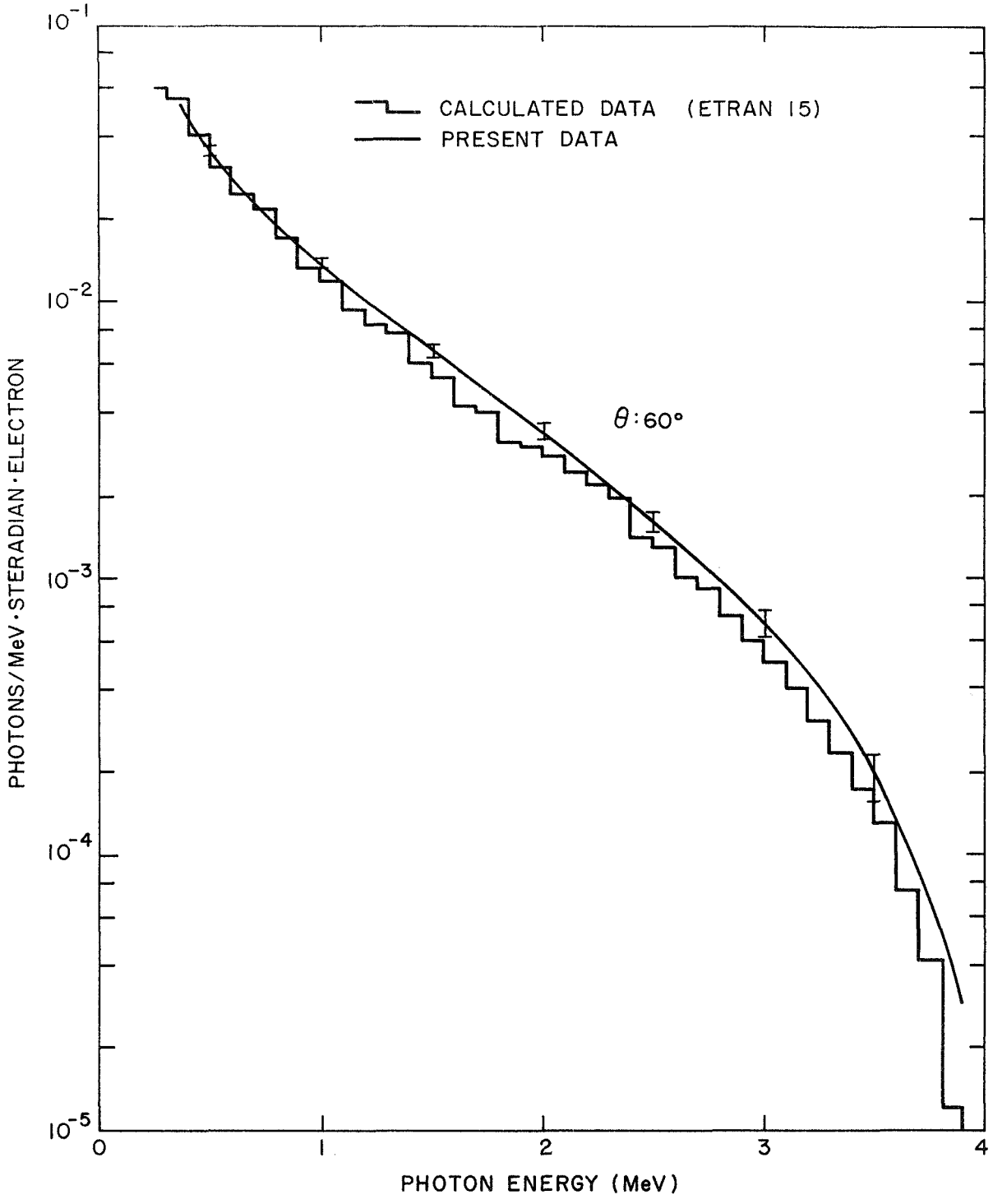

Fig. 36. Comparison between measured and calculated bremsstrahlung spectra at 60^{o} for 4.0 MeV incident electrons on a thick target of tin ($3.29\ g/cm^2$)

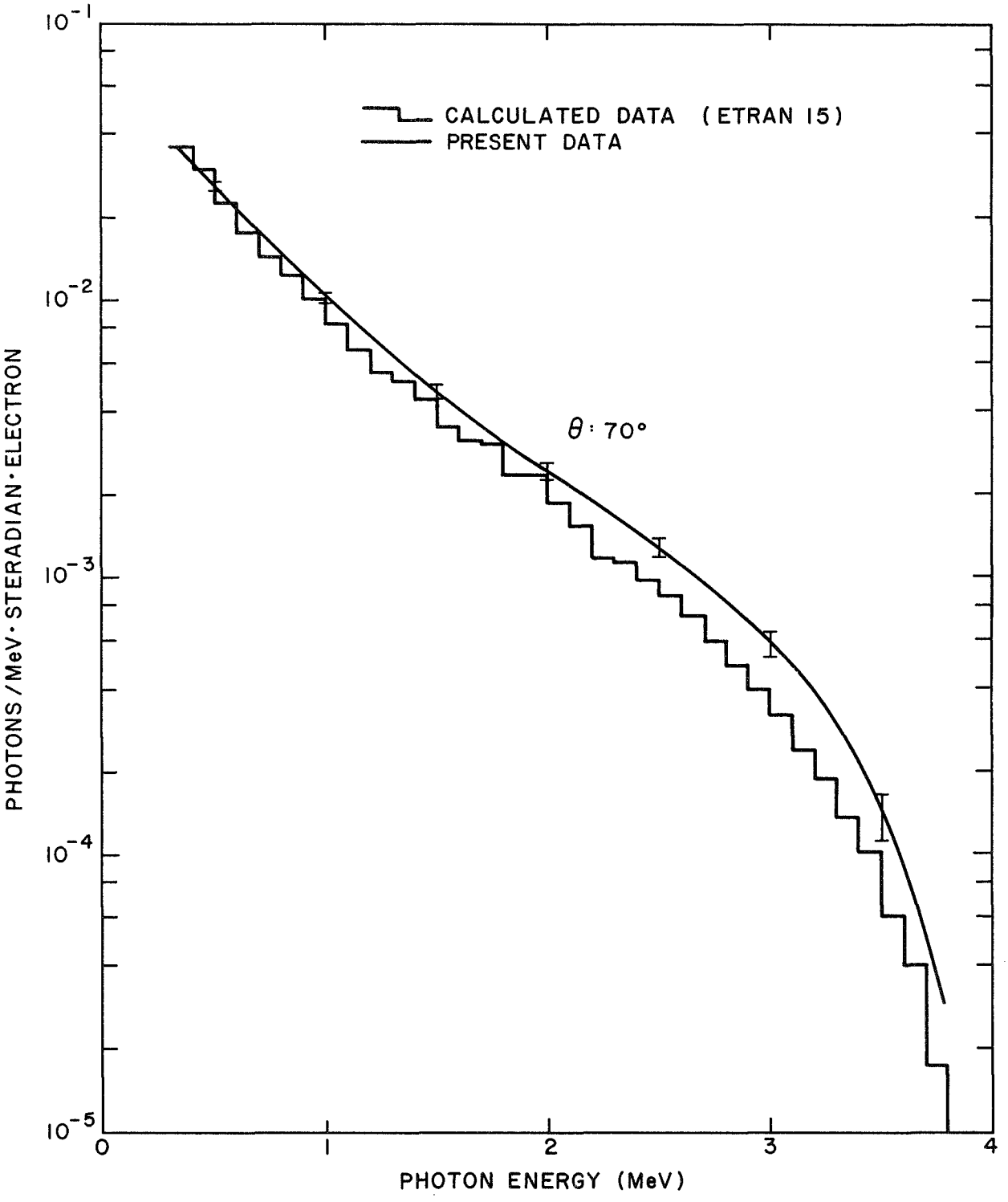

Fig. 37. Comparison between measured and calculated bremsstrahlung spectra at 70° for 4.0 MeV incident electrons on a thick target of tin ($3.29\ g/cm^2$)

and calculated data that is similar to the one observed for the 0^{o} measurements. The calculated curves or histograms have a steeper slope than the measured data at low energies. Over the range of energy up to the incident electron energy the ETRAN 15 results fit the measured data quite closely. As shown in Fig. 38 the absolute yields are typically lower than the measured data. The disagreement is worst at 10^{o} with 2.2 percent, and gradually improves to good agreement at 40^{o} to 60^{o}.

For angles 10^{o} through 70^{o} for 8-MeV incident electron energy, Figs. 39 through 45 again show discrepancies in shape between measured and calculated data similar to those pointed out for the 4-MeV data. In addition, in the high energy limit the calculated points drop off more rapidly than the measured values in a manner similar to the one observed at 0^{o}. As far as absolute yields are concerned, the calculated values are higher than the measured ones with the best agreement obtained at large angles as shown in Fig. 46. It can be safely assumed that the discrepancies in shape can be partly attributed to inadequacies in the bremsstrahlung production cross section at low energies as well as in the high energy limit. Also, the spectral shape as well as the yield should depend on the manner in which the effects of multiple scattering and energy loss are taken into account. The unfolded bremsstrahlung spectra as well as the integrated yields along with the errors are displayed in Tables 11, 12, and 13.

The most important sources of experimental error are associated with counting statistics, detector-efficiency calibration, generation of the response matrix and the unfolding calculations.

The nearly singular response functions of the detector as well as the rapidly falling spectrum facilitated the calculation of the statistical uncertainty on the unfolded spectrum $\underline{x}(E_i)$. The fractional error on $\underline{x}(E_i)$ may be obtained by adding in quadrature the fractional errors on the two components of the raw data y_k, i.e., the "photopeak counts" y_k^p due to photons of energy E_k and the Compton-tail (plus escape) counts y_k^c in channel

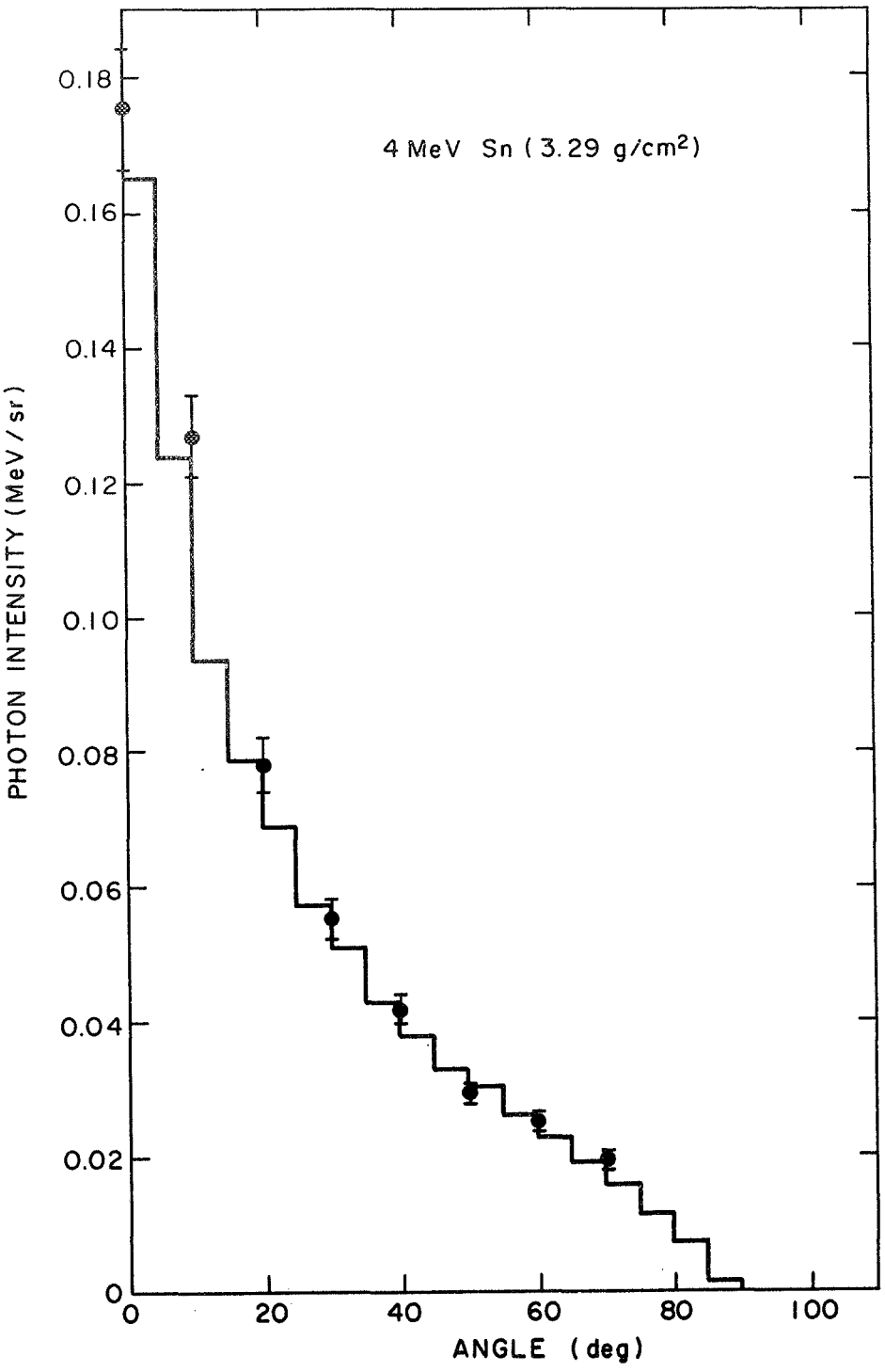

Fig. 38. A comparison of the total measured energy from bremsstrahlung at various angles with that given by ETRAN 15. The target was tin, 3.29 g/cm^2 thick and the incident electron energy was 4.0 MeV.

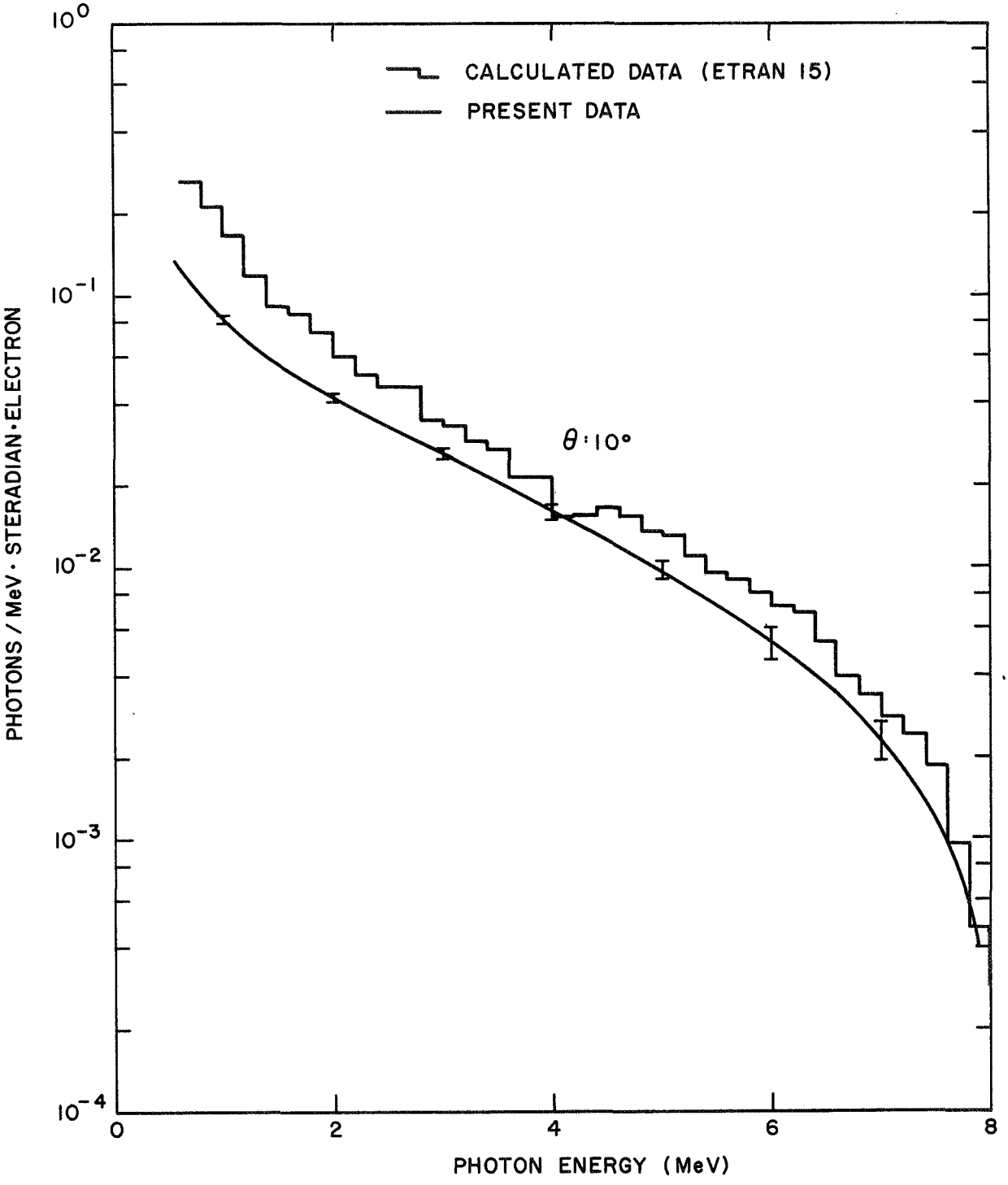

Fig. 39. Comparison between measured and calculated bremsstrahlung spectra at 10^{o} for 8.0 MeV incident electrons on a thick target of tin ($5.84\ g/cm^{2}$)

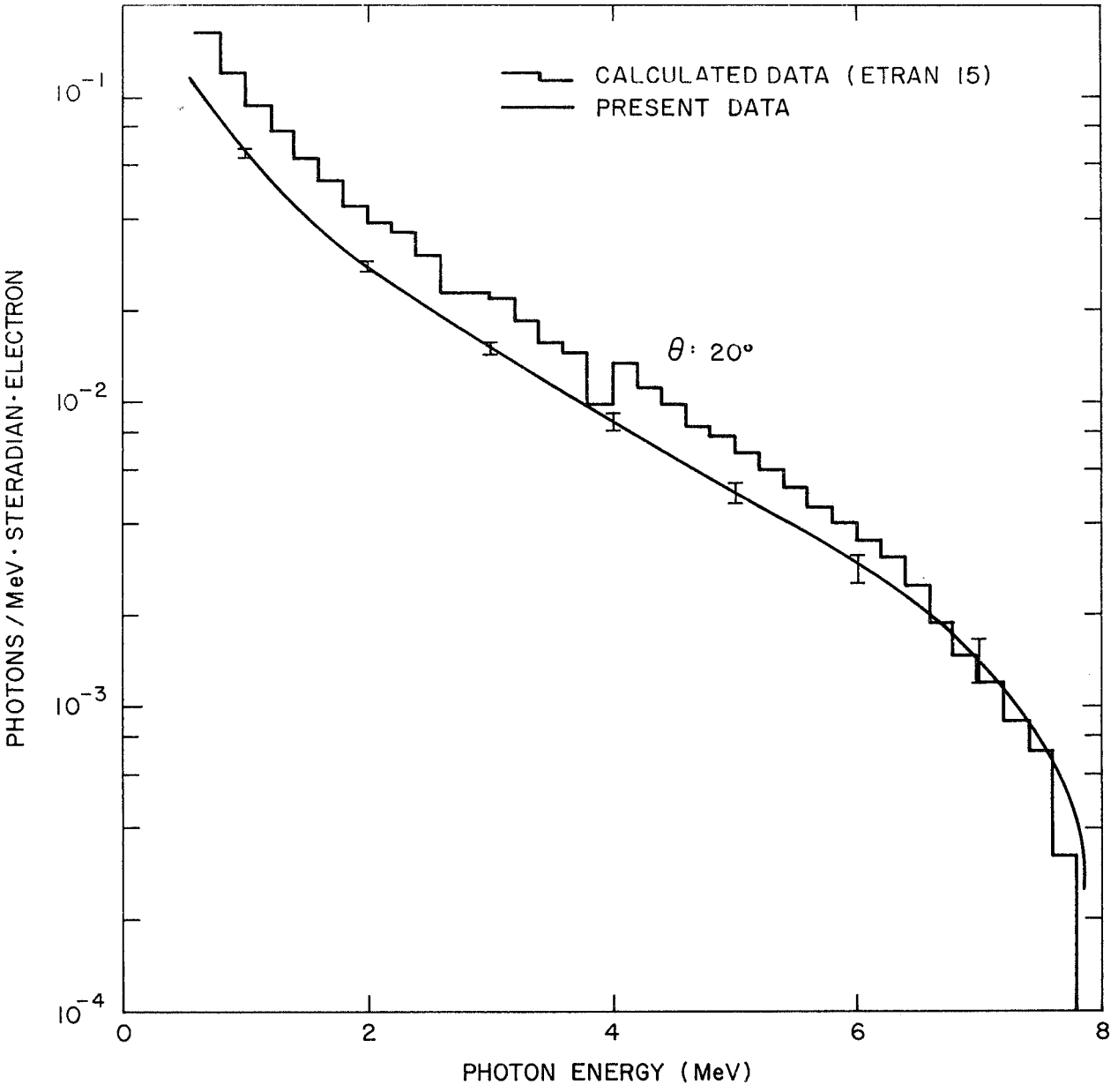

Fig. 40. Comparison between measured and calculated bremsstrahlung spectra at 20^{o} for 8.0 MeV incident electrons on a thick target of tin ($5.84\ g/cm^2$)

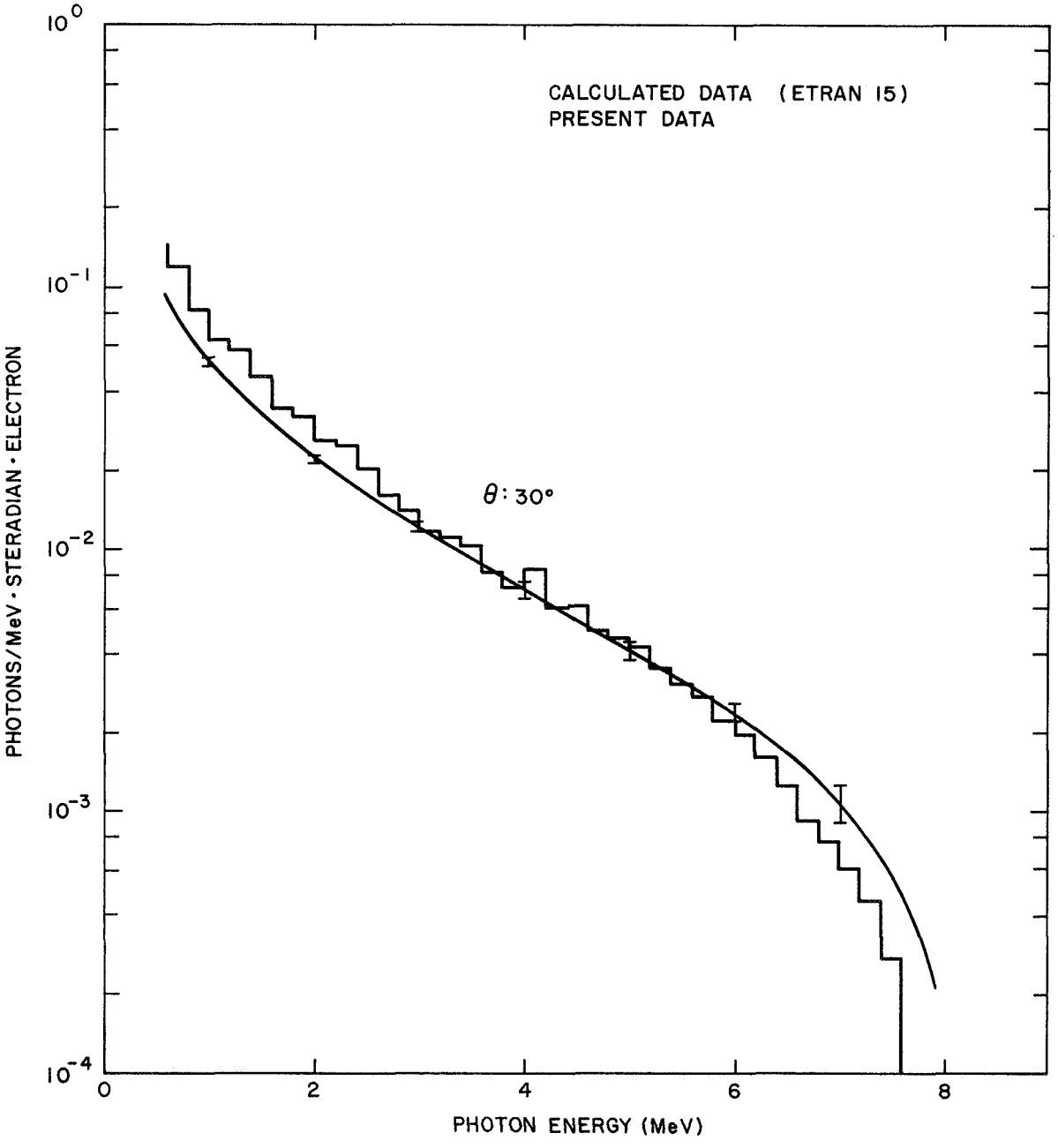

Fig. 41. Comparison between measured and calculated bremsstrahlung spectra at 30^{o} for 8.0 MeV incident electrons on a thick target of tin ($5.84\ g/cm^2$)

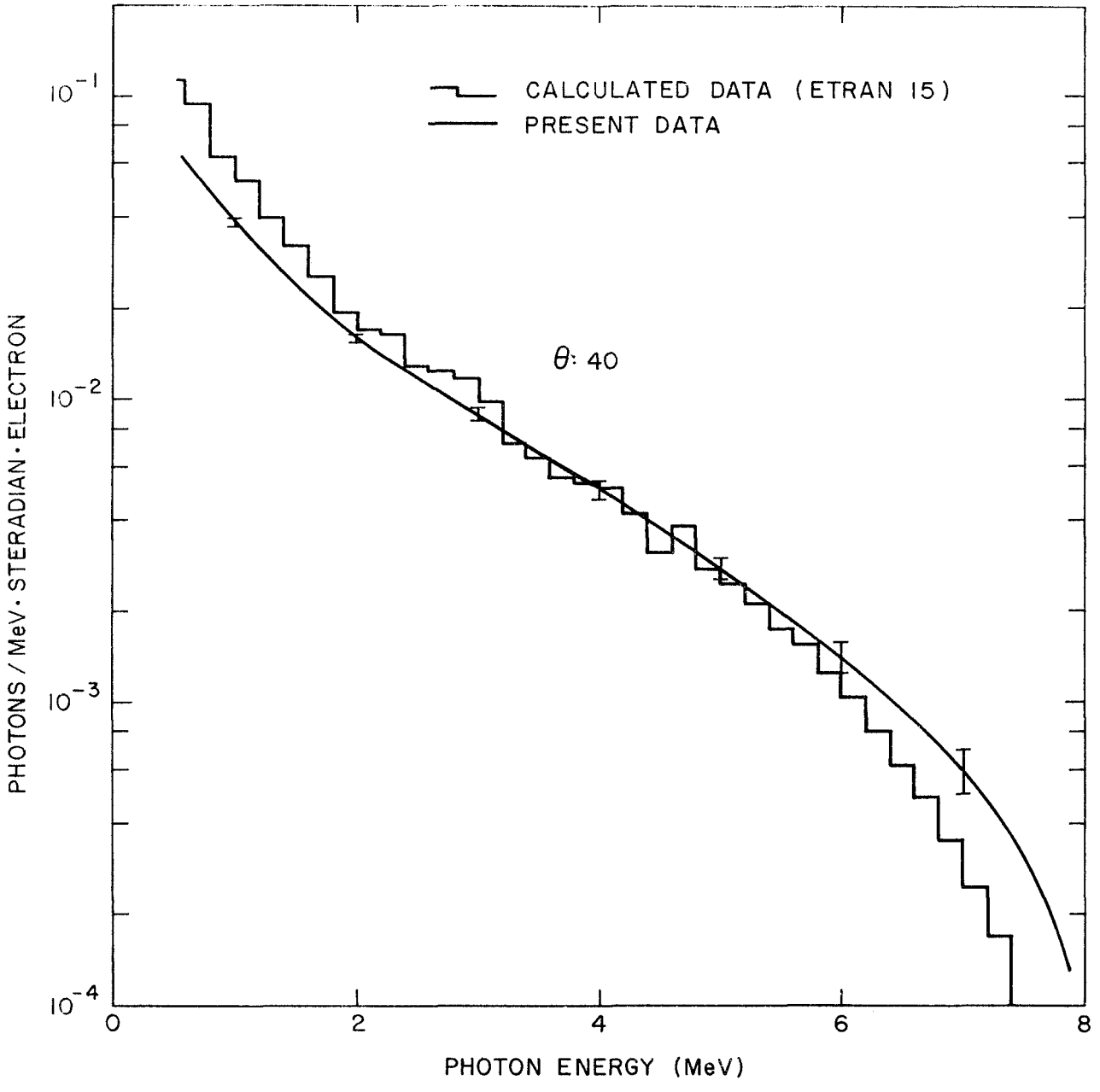

Fig. 42. Comparison between measured and calculated bremsstrahlung spectra at 40° for 8.0 MeV incident electrons on a thick target of tin ($5.84\ g/cm^2$)

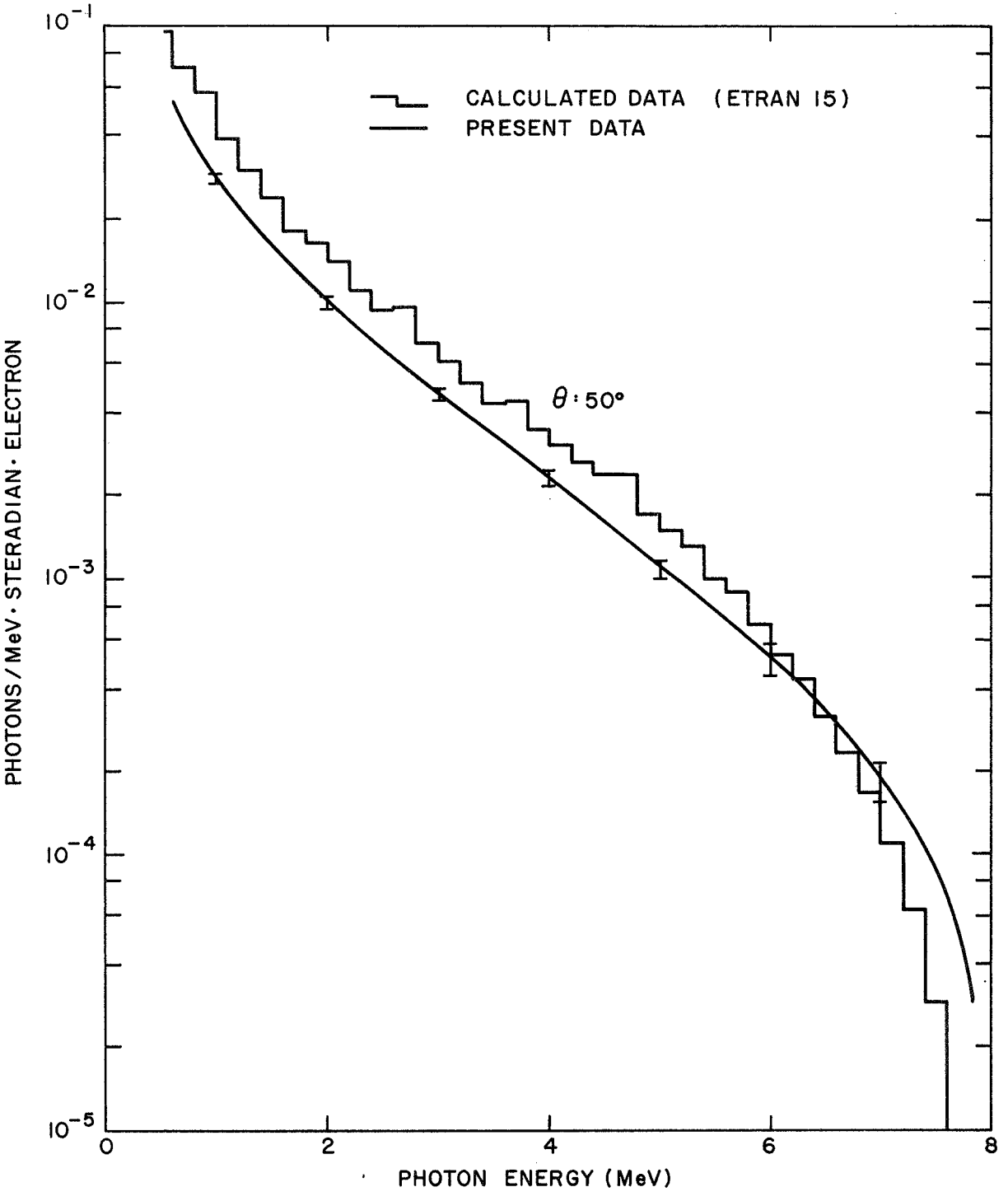

Fig. 43. Comparison between measured and calculated bremsstrahlung spectra at 50° for 8.0 MeV incident electrons on a thick target of tin ($5.84\ g/cm^2$)

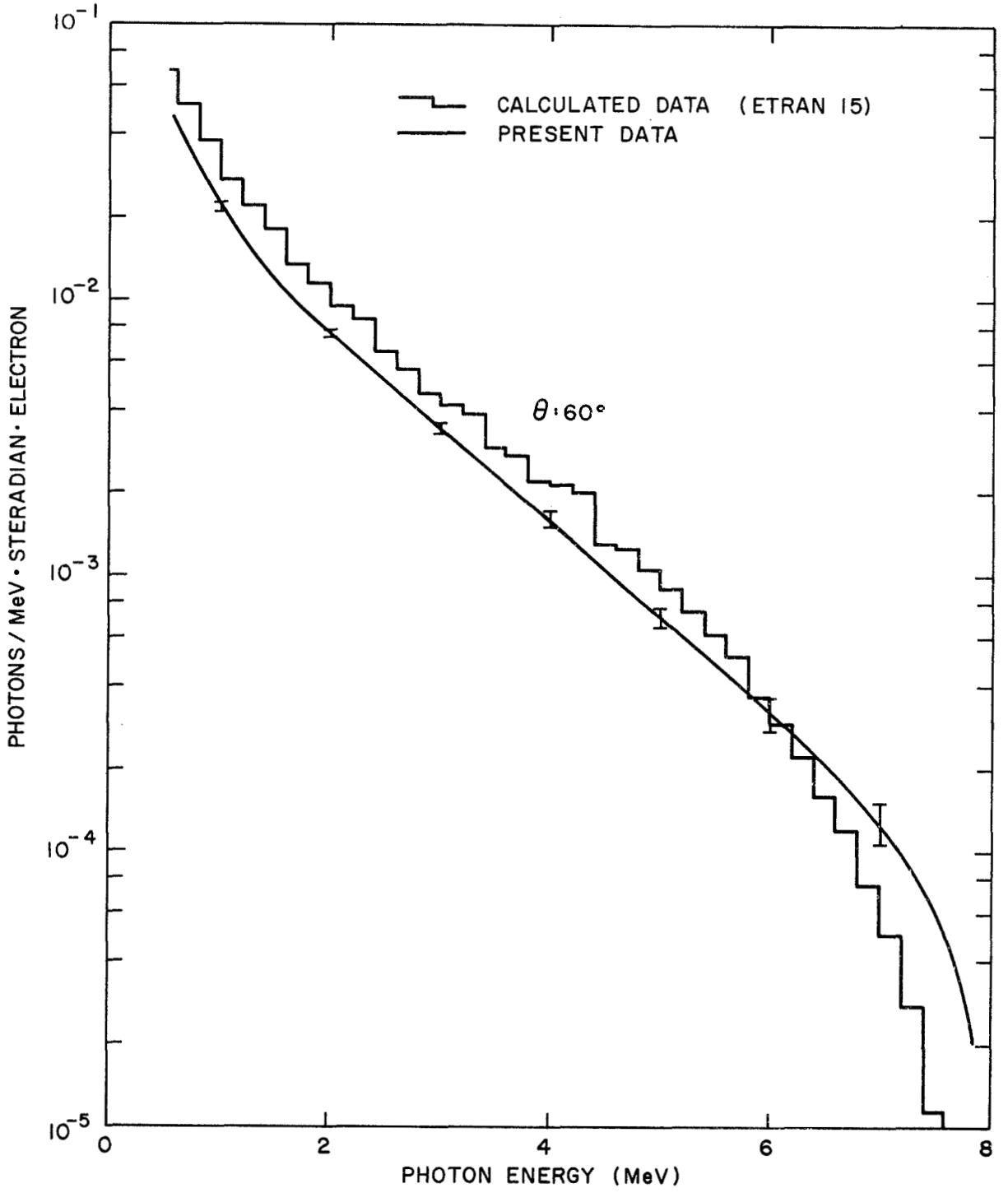

Fig. 44. Comparison between measured and calculated bremsstrahlung spectra at 60^{o} for 8.0 MeV incident electrons on a thick target of tin ($5.84\ g/cm^2$)

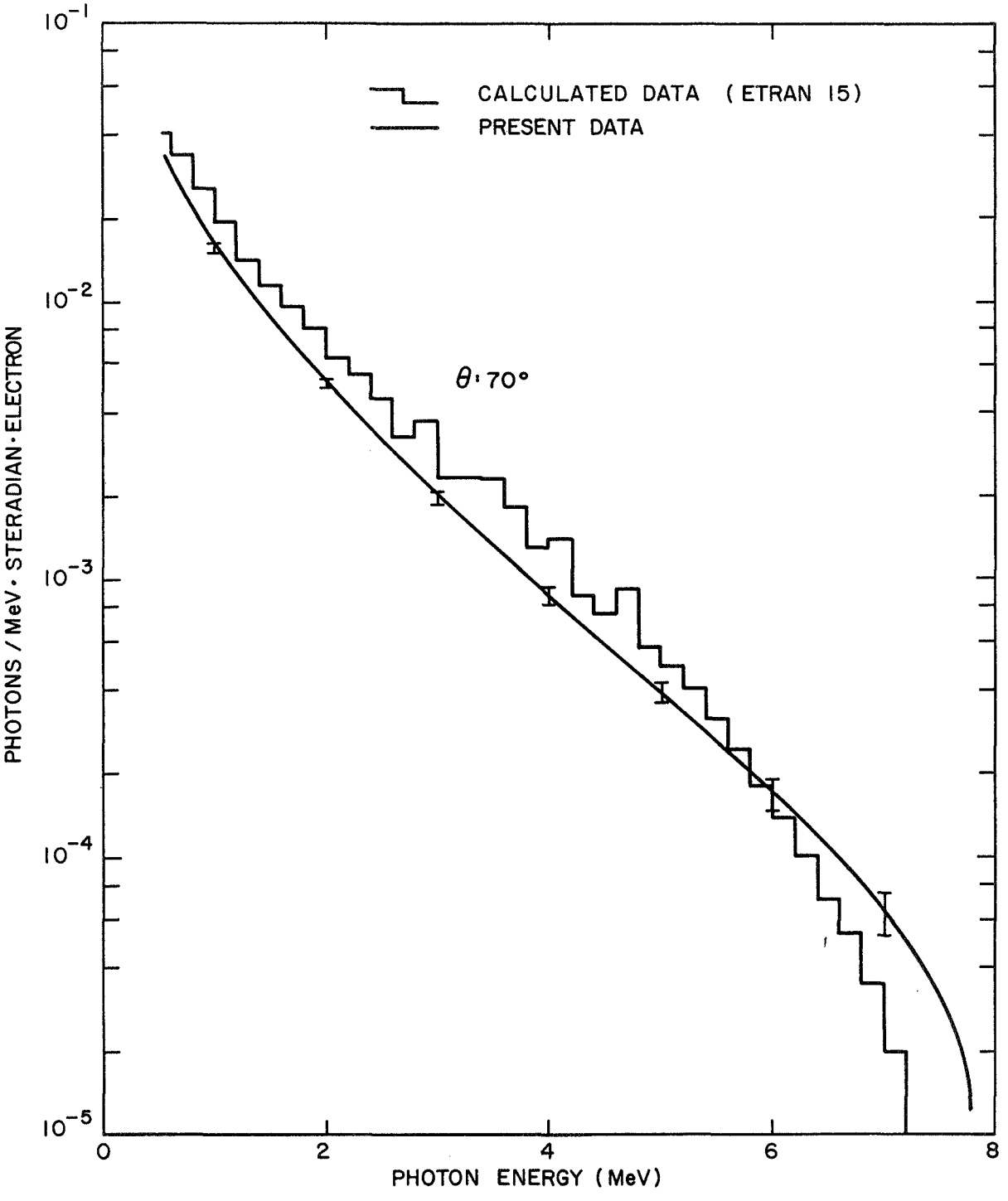

Fig. 45. Comparison between measured and calculated bremsstrahlung spectra at 70° for 8.0 MeV incident electrons on a thick target of tin ($5.84\ g/cm^2$)

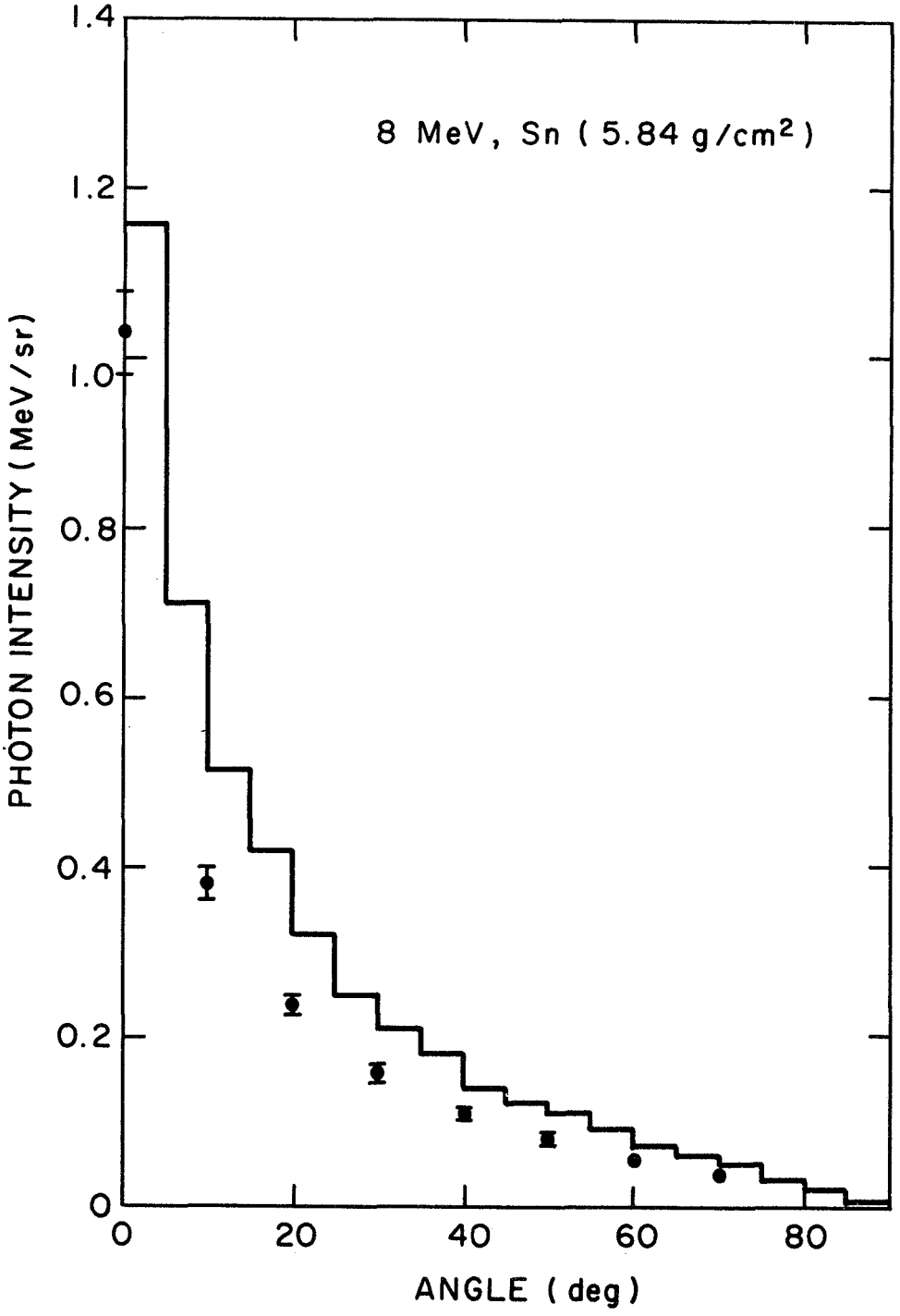

Fig. 46. A comparison of the total measured energy from bremsstrahlung at various angles with that given by ETRAN 15. The target was tin, 5.84 g/cm^2, and the incident electron energy was 8.0 MeV.

Table 11

4 MeV on Sn

PHOTONS/MeV-STERADIAN-ELECTRON

E (MeV)	θ 0° (x 10^{-3})	10° (x 10^{-3})	20° (x 10^{-3})	30° (x 10^{-3})	40° (x 10^{-3})	50° (x 10^{-3})	60° (x 10^{-3})	70° (x 10^{-3})
0.5	156.0 ± 2.0	112.0 ± 3.0	75.4 ± 2.1	58.5 ± 1.6	50.7 ± 1.4	38.8 ± 1.1	35.4 ± 1.0	26.0 ± 0.7
1.0	72.0 ± 1.4	55.0 ± 2.0	35.3 ± 1.3	25.6 ± 0.9	20.6 ± 0.7	16.2 ± 0.6	13.9 ± 0.5	10.3 ± 0.4
1.5	44.3 ± 1.3	30.5 ± 1.6	19.4 ± 1.0	14.3 ± 0.7	11.1 ± 0.6	7.65 ± 0.40	6.73 ± 0.35	4.74 ± 0.25
2.0	29.8 ± 1.2	19.1 ± 1.4	11.3 ± 0.8	8.45 ± 0.60	6.45 ± 0.46	4.23 ± 0.30	3.43 ± 0.24	2.41 ± 0.17
2.5	18.4 ± 0.9	12.9 ± 1.0	7.0 ± 0.56	4.62 ± 0.37	3.42 ± 0.27	2.08 ± 0.17	1.60 ± 0.13	1.29 ± 0.10
3.0	10.8 ± 0.7	7.54 ± 0.75	4.24 ± 0.42	2.37 ± 0.24	1.59 ± 0.16	0.830 ± 0.083	0.698 ± 0.070	0.580 ± 0.058
3.5	4.05 ± 0.41	3.60 ± 0.70	1.93 ± 0.38	1.04 ± 0.20	0.474 ± 0.093	0.207 ± 0.040	0.194 ± 0.038	0.140 ± 0.027
3.75	1.46 ± 0.26	1.97 ± 0.41	0.992 ± 0.210	0.572 ± 0.120	0.187 ± 0.039	0.068 ± 0.014	0.0665 ± 0.014	0.0370 ± 0.008

Table 12

8 MeV on Sn

PHOTONS/MeV-STERADIAN-ELECTRON

E (MeV)	θ 0° (x 10^{-3})	10° (x 10^{-3})	20° (x 10^{-3})	30° (x 10^{-3})	40° (x 10^{-3})	50° (x 10^{-3})	60° (x 10^{-3})	70° (x 10^{-3})
1	241.0 ± 14.0	82.5 ± 2.1	66.2 ± 1.7	52.5 ± 1.4	38.8 ± 1.0	28.1 ± 0.7	22.3 ± 0.6	15.7 ± 0.4
2	110.0 ± 7.0	42.7 ± 1.2	27.9 ± 0.8	22.1 ± 0.6	16.1 ± 0.4	10.2 ± 0.3	7.60 ± 0.2	5.10 ± 0.14
3	67.5 ± 5.6	26.4 ± 1.1	15.0 ± 0.6	12.0 ± 0.5	8.95 ± 0.4	4.67 ± 0.19	3.44 ± 0.14	1.96 ± 0.08
4	43.0 ± 4.3	15.9 ± 1.0	8.65 ± 0.57	7.0 ± 0.45	5.05 ± 0.33	2.30 ± 0.15	1.61 ± 0.11	0.880 ± 0.058
5	27.7 ± 4.9	9.75 ± 0.73	5.03 ± 0.38	4.10 ± 0.31	2.76 ± 0.21	1.08 ± 0.08	0.715 ± 0.054	0.395 ± 0.029
6	19.3 ± 4.8	5.30 ± 0.69	2.93 ± 0.38	1.37 ± 0.18	1.41 ± 0.18	0.513 ± 0.067	0.320 ± 0.042	0.170 ± 0.022
7	12.3 ± 3.7	2.37 ± 0.38	1.42 ± 0.23	1.09 ± 0.18	0.600 ± 0.099	0.183 ± 0.030	0.128 ± 0.021	0.064 ± 0.011
7.5	7.40 ± 1.48	1.2 ± 0.24	0.780 ± 0.156	0.570 ± 0.114	0.300 ± 0.06	0.088 ± 0.018	0.062 ± 0.012	0.032 ± 0.06

Table 13

BREMSSTRAHLUNG YIELD FROM 4 AND 8 MeV ELECTRONS ON THICK Sn TARGETS

(5% total uncertainty on all measured values)

	0.365-4 MeV (3.29 g/cm^2)		0.56-8 MeV (5.84 g/cm^2)	
θ	Average Energy	MeV Sr. - Electron	Average Energy	MeV Sr. - Electron
0°	1.20	0.175	2.25	1.03
10°	1.20	0.127	2.18	0.382
20°	1.16	0.0783	2.09	0.238
30°	1.10	0.0554	2.03	0.159
40°	1.06	0.0418	1.96	0.110
50°	1.0	0.0294	1.87	0.0770
60°	1.0	0.0251	1.82	0.0560
70°	1.01	0.0194	1.72	0.0354

k that are due to photons of energy greater than E_k. y_k^c is obtained by multiplying the value of the unfolded spectrum in channel k by the detector efficiency Σ_k corresponding to E_k and subtracting the value from y_k. Since $y_k^p = y_k - y_k^c$, the photopeak contribution to the error is simply $\sigma_k = \sqrt{y_k^p}$. The error σ^c on y_k^c is derived from the fractional error on the "photopeak counts" above E_k to which the Compton tail and escape peaks belong. This is done utilizing the response matrix, $\underline{G}$. Since σ^c is typically much smaller than σ^p, especially at high energies, the overall uncertainties on $\underline{x}(E_k)$ could be obtained with good accuracy. The ratio y_k^p/y_k of "photopeak counts" to total counts in a given channel k was about 0.87. This method yields the largest possible uncertainty on each channel $x(E_i)$. Actually the fractional errors are smaller due to the correlating of adjacent channels over intervals of at least detector resolution width that is performed in the unfolding process. Consequently, to obtain a more realistic estimate the fractional errors on channel $x(E_k)$ is calculated as the combined uncertainty on the group of those channels $x(E_i)$ around $x(E_n)$ that fall within a detector resolution width.

To estimate errors which are associated with inaccuracies in the response matrix, a pulse-height distribution was unfolded with the Compton tail portion increased by 20 percent. This is considerably more than any fitting error for the response functions. The corresponding error on the spectral shape was less than the combined uncertainties due to counting statistics and detector-efficiency measurements (see Section 2.2.1).

The accuracy of the unfolding code was always checked by carrying out the refold of $\underline{x}(E)$ according to $\underline{y} = \underline{\underline{\sigma}} \cdot \underline{x}$ and small local corrections applied to $\underline{x}(E)$ where necessary.

This refold is accurate because it directly utilized the response matrix $\sigma(I, J)$, without any of the conditioning employed in the unfolding process. Thus, it is reasonably certain that the dominant error on the

spectrum arises from the detector-efficiency calibration except at high energy where $\underline{x}(E)$ is small and the statistical error is large. Consequently the dominant error on the integrated quantities results from the uncertainty in the efficiency calibration, which is about 3 percent. A conservative over-all error of 5 percent is assumed for the thick target data.

3.3 THIN TARGET BREMSSTRAHLUNG MEASUREMENTS

The thin target data from 4 and 8 MeV electrons on Au and Ag were unfolded in the same manner as the thick target data. At 0° they are compared to spectra calculated directly from the bremsstrahlung production cross sections by Schiff, used by Dickinson and Lent[2] as well as by Sauter, and tabulated by Koch and Motz.[14] At the other angles, the measured results are compared only to those calculated on the basis of the Sauter cross section.

Figures 47 through 58 and Tables 14 through 17 show the results for 4- and 8-MeV incident electron energy. The error bars on the measured spectra indicate the statistical uncertainties only. The uncertainty on the measured integrated values has increased to 15 percent from the 5 percent for the thick target measurements. This increase is almost entirely due to larger systematic errors that take into account the nonuniformity of the targets, the severe background problem, and the increased uncertainty in the current calibration.

For the 4-MeV case, only the 0° measurements are absolutely normalized, the others only allow a relative comparison between the measured and calculated results. A severe instability in the injector pulse gate which went unnoticed at first took place in the experiments at 3° and 6°. A last minute repetitive series of measurements was rendered meaningless due to severe beam focusing and stability problems. The measurements at 8 MeV, which were made earlier than the 4 MeV, are all absolutely normalized.

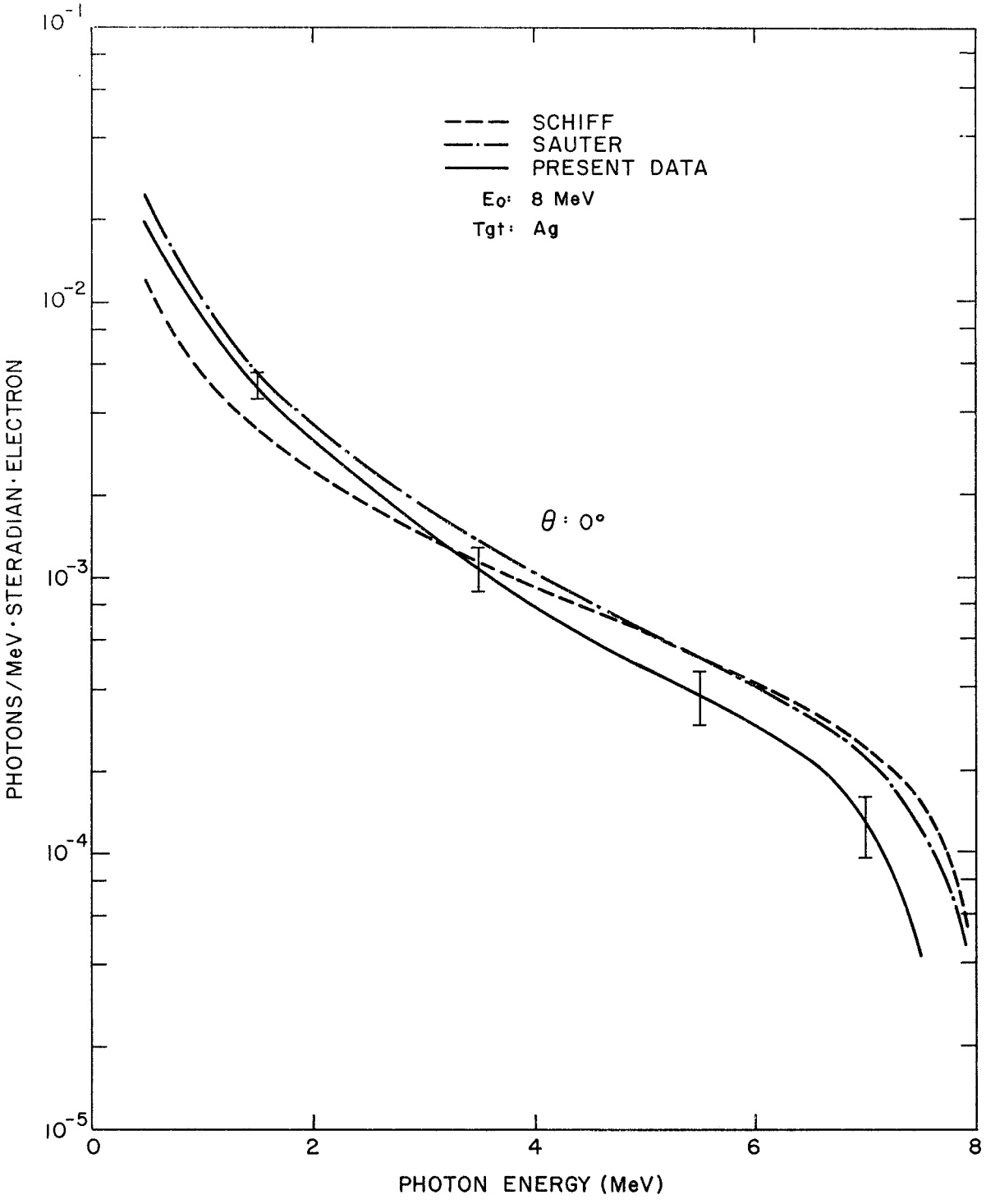

Fig. 47. Bremsstrahlung yield at 0^{o} from a 0.5 mg/cm^{2} thick target of silver for 8.0 MeV electrons

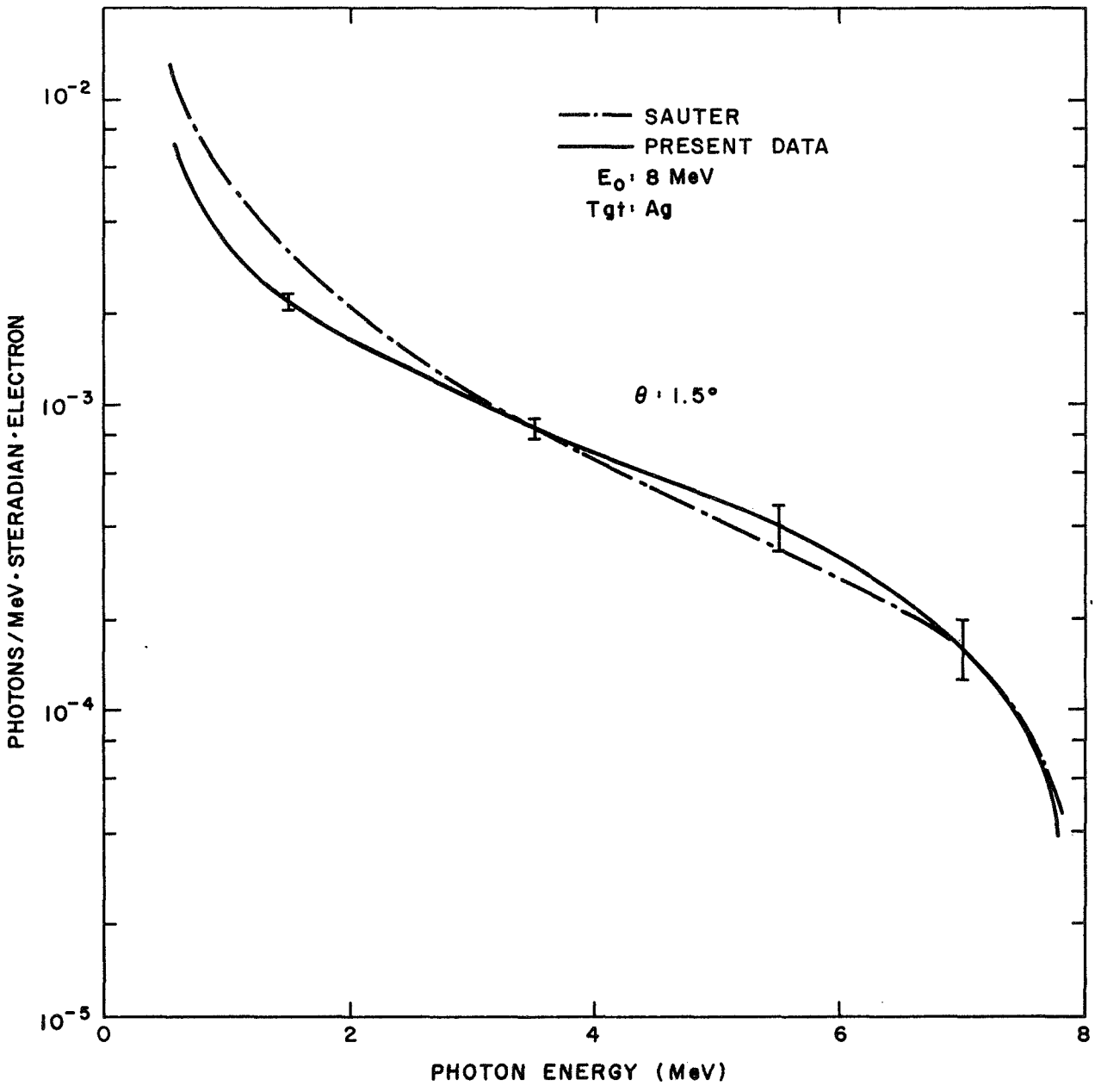

Fig. 48. Bremsstrahlung yield at 1.5^{o} from a 0.5 mg/cm^2 thick target of silver for 8.0 MeV electrons

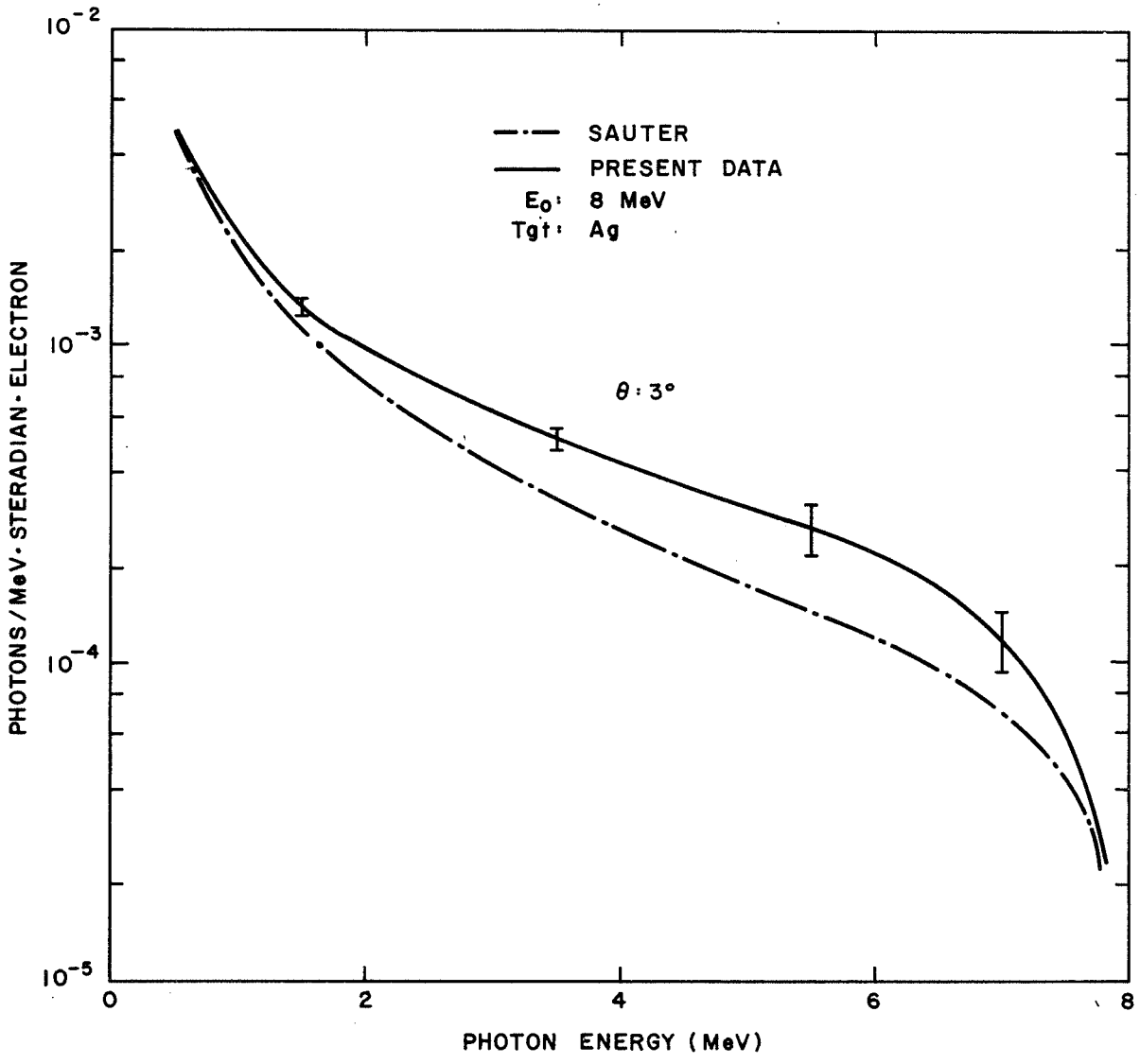

Fig. 49. Bremsstrahlung yield at 3^{o} from a 0.5 mg/cm^{2} thick target of silver for 8.0 MeV electrons

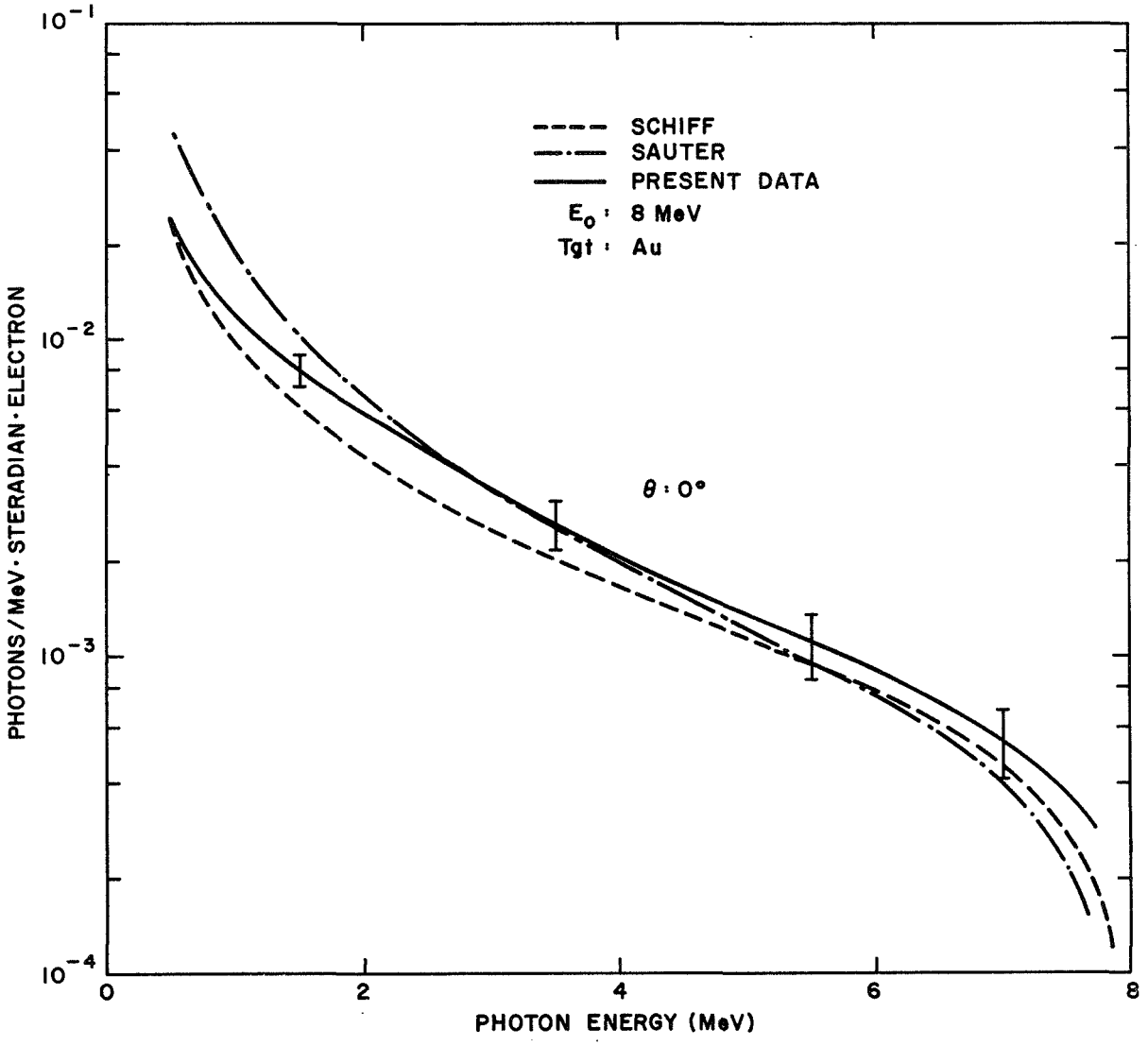

Fig. 50. Bremsstrahlung yield at 0^{o} from a 0.6 mg/cm^{2} thick target of gold for 8.0 MeV electrons

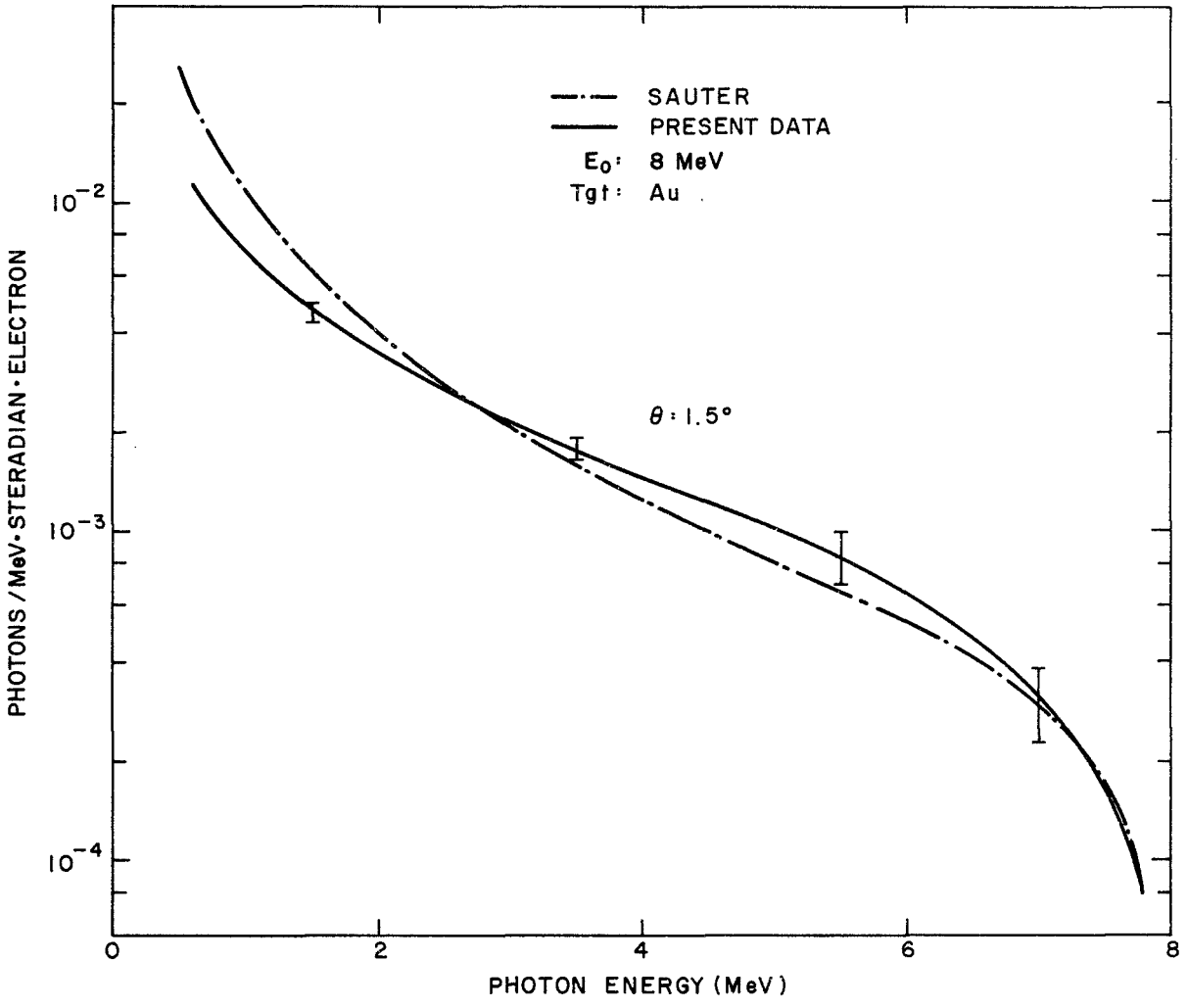

Fig. 51. Bremsstrahlung yield at 1.5° from a 0.6 mg/cm^2 thick target of gold for 8.0 MeV electrons

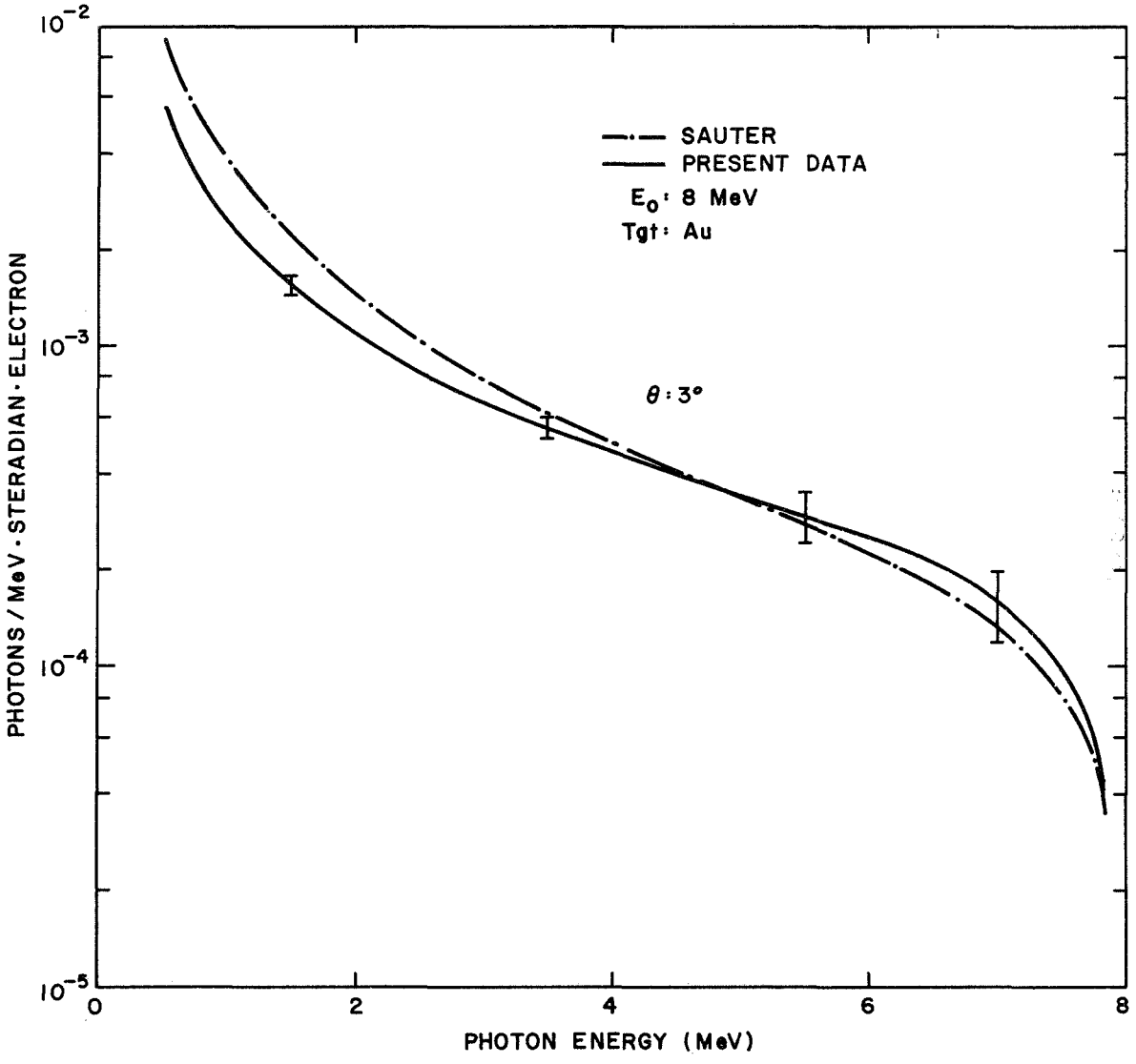

Fig. 52. Bremsstrahlung yield at 3^{o} from a 0.6 mg/cm^{2} thick target of gold for 8.0 MeV electrons

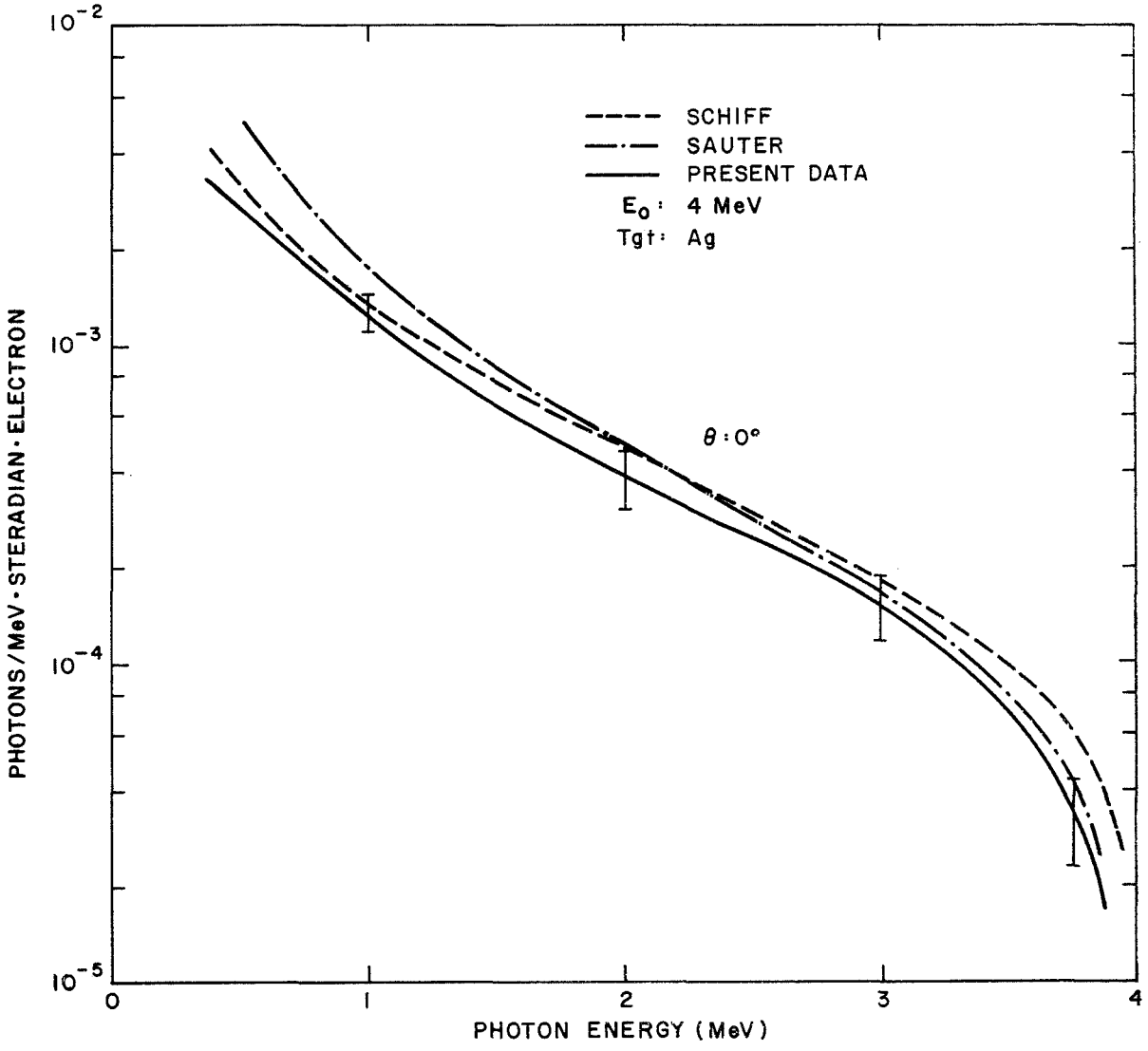

Fig. 53. Bremsstrahlung yield at 0^{o} from a 0.5 mg/cm^{2} thick target of silver for 4.0 MeV electrons

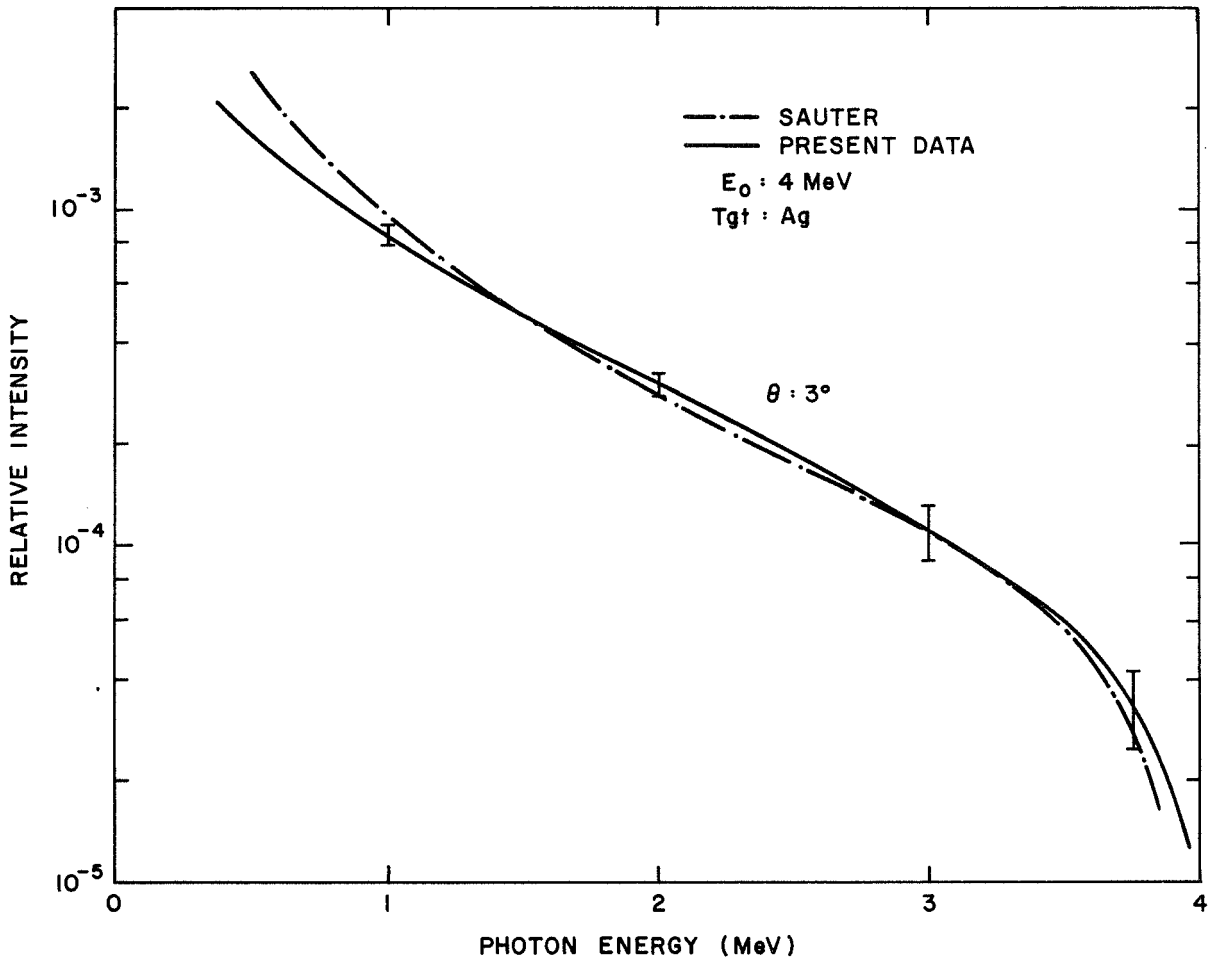

Fig. 54. Bremsstrahlung yield at 3^{o} from a 0.5 mg/cm^{2} thick target of silver for 4.0 MeV electrons

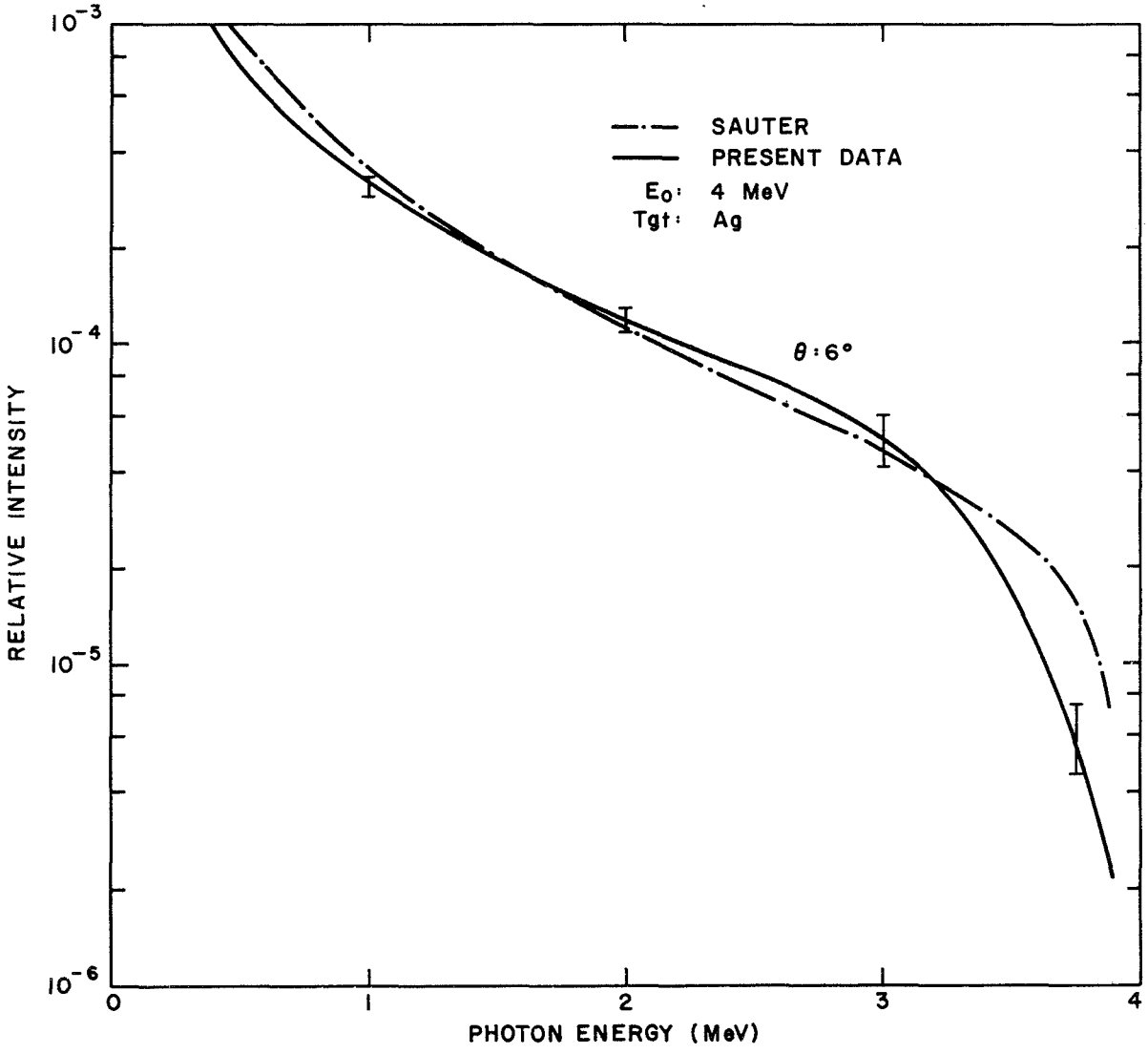

Fig. 55. Bremsstrahlung yield at 6^{o} from a 0.5 mg/cm^{2} thick target of silver for 4.0 MeV electrons

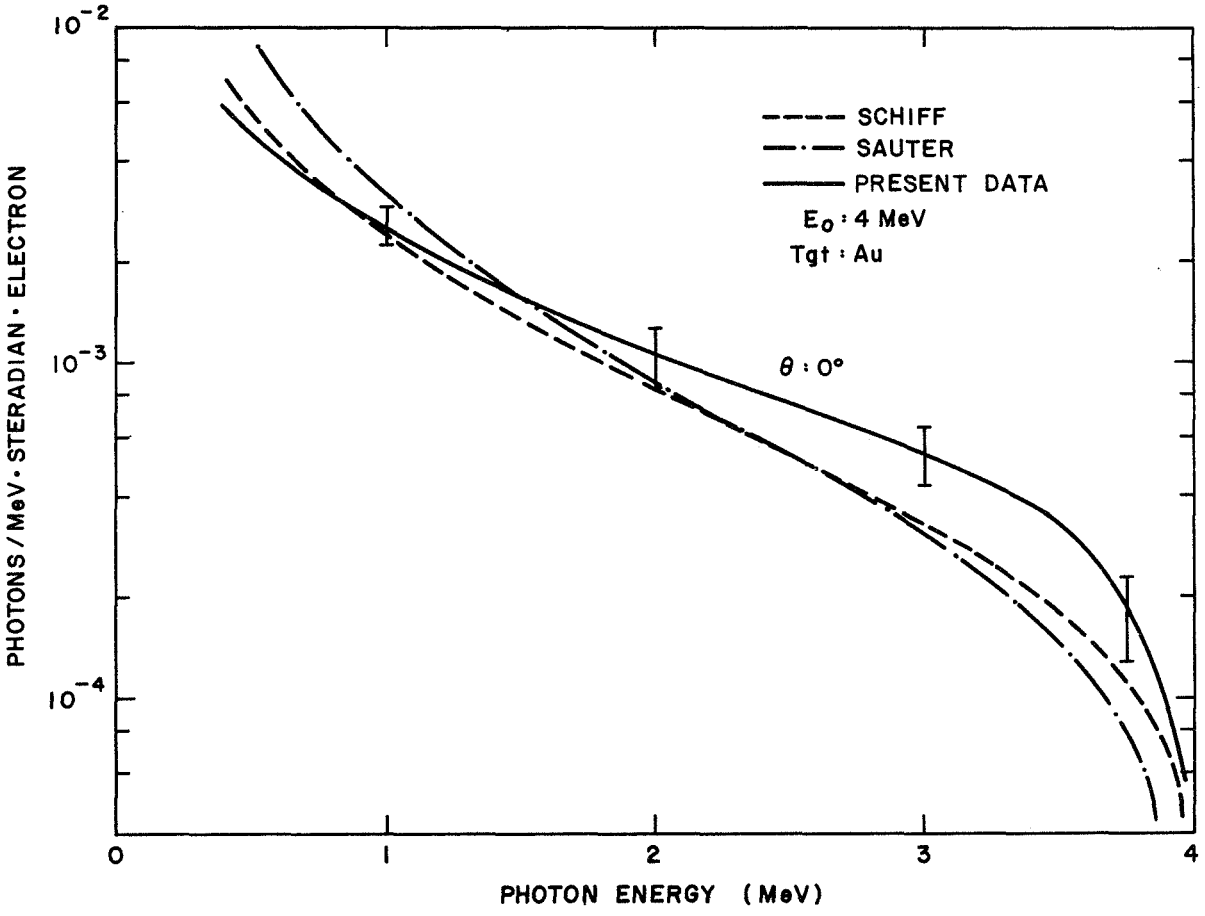

Fig. 56. Bremsstrahlung yield at 0° from a 0.6 mg/cm^2 thick target of gold for 4.0 MeV electrons

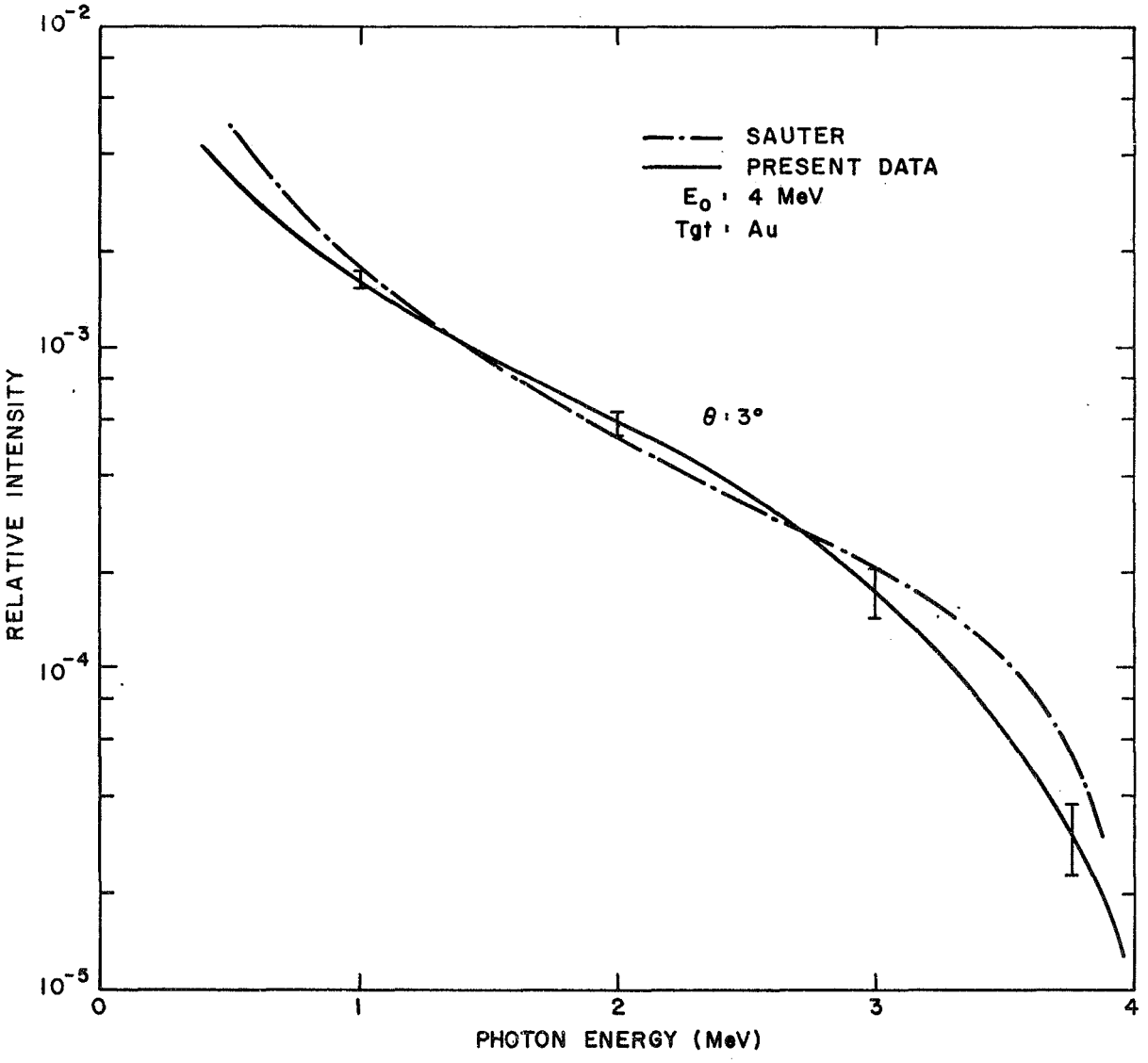

Fig. 57. Bremsstrahlung yield at 3^{o} from a 0.6 mg/cm^{2} thick target of gold for 4.0 MeV electrons

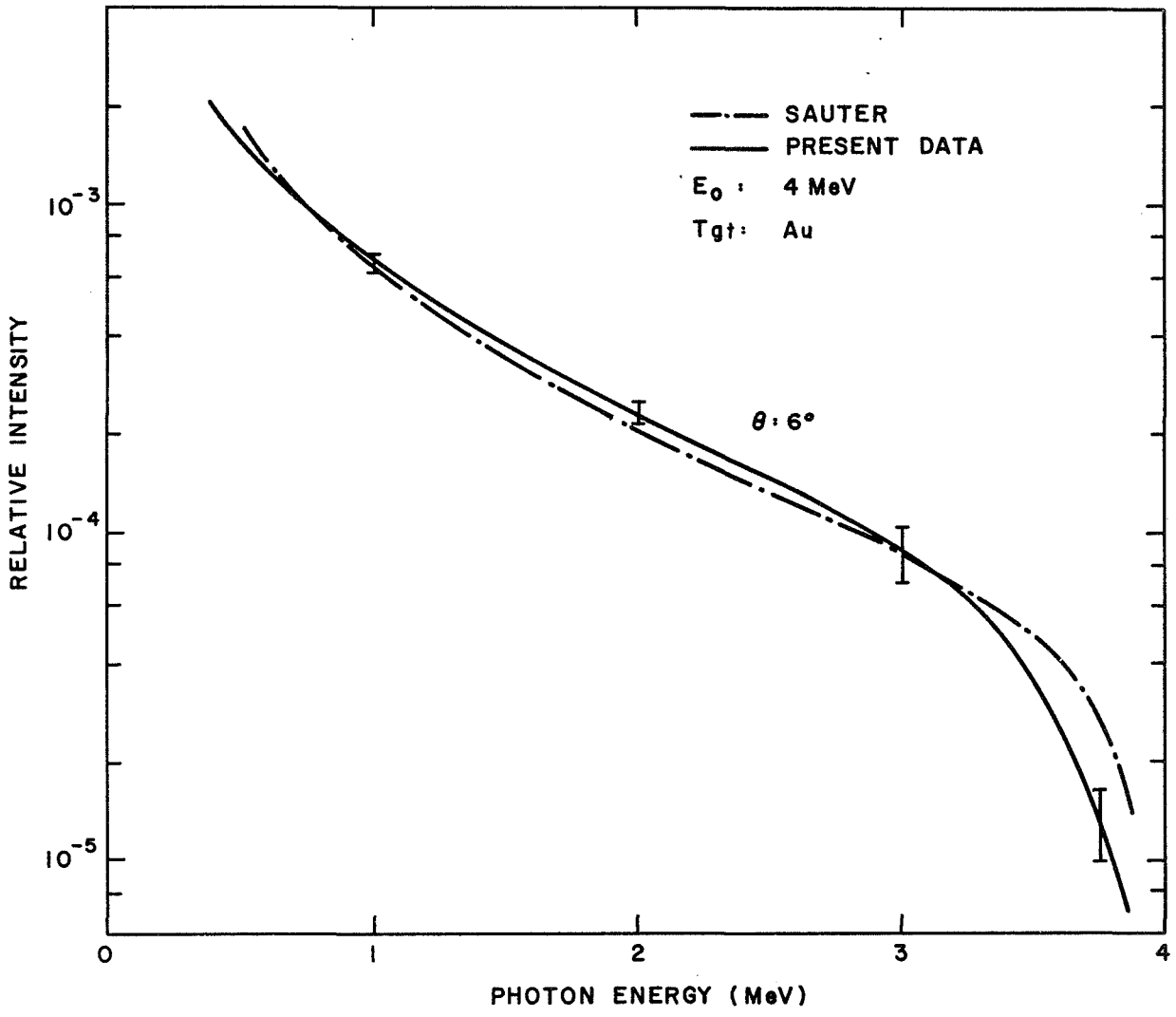

Fig. 58. Bremsstrahlung yield at 6^{o} from a 0.6 mg/cm^{2} thick target of gold for 4.0 MeV electrons

Table 14

BREMSSTRAHLUNG YIELD FROM 8 MeV ON THIN Ag AND Au TARGETS[a]

(15% total uncertainty on all measured values)

	MeV/Sr-Electron		Average Energy		MeV/Sr-Electron			
					Sauter		Schiff	
θ	Ag	Au	Ag	Au	Ag	Au	Ag	Au
0^{o}	0.0274	0.0595	1.76	2.28	0.0267	0.0629	0.0263	0.0455
1.5^{o}	0.0177	0.0361	2.36	2.32	0.0164	0.0397		
3^{o}	0.0114	0.0247	2.39	2.40	0.0064	0.0158		

[a] 0.56 to 8 MeV

Table 15

BREMSSTRAHLUNG YIELD AT 0° FROM 4 MeV ELECTRONS ON THIN Ag AND Au TARGETS[a]

(15% total uncertainty on all measured values)

	MeV/Sr-Electron	Average Energy	MeV/Sr-Electron	
			Sauter	Schiff
Ag	0.00291	1.23	0.00253	0.00345
Au	0.00653	1.25	0.00596	0.00607

[a] 0.365 to 4 MeV, 0°

Table 16

BREMSSTRAHLUNG SPECTRA AT 0° FROM 4 MeV ELECTRONS ON THIN Ag AND Au TARGETS

(0°, 4 MeV)

	Photons/MeV-Steradian-Electron	
	Ag	Au
E (MeV)	($\times 10^{-5}$)	($\times 10^{-5}$)
1	127.0 ± 17.0	257.0 ± 33.0
2	38.6 ± 7.7	106.0 ± 21.0
3	15.3 ± 3.5	53.6 ± 10.7
3.75	3.34 ± 1.01	18.2 ± 4.6

Table 17

BREMSSTRAHLUNG SPECTRA FROM 8 MeV ELECTRONS
ON THIN Ag AND Au TARGETS

θ / E (MeV)	Photons/Steradian-Electron					
	Ag			Au		
	0^{o} ($\times 10^{-5}$)	1.5^{o} ($\times 10^{-5}$)	3.0^{o} ($\times 10^{-5}$)	0^{o} ($\times 10^{-5}$)	1.5^{o} ($\times 10^{-5}$)	3.0^{o} ($\times 10^{-5}$)
1.5	505.0 ± 56.0	219.0 ± 13.0	132.0 ± 8.0	802.0 ± 90.0	463.0 ± 28.0	156.0 ± 9.0
3.5	109.0 ± 19.0	84.5 ± 5.9	50.5 ± 4.0	263.0 ± 46.0	177.0 ± 14.0	56.2 ± 4.5
5.5	37.2 ± 8.2	40.0 ± 7.0	26.7 ± 4.8	109.0 ± 24.0	84.0 ± 15.1	29.7 ± 5.4
7.0	12.9 ± 3.2	16.2 ± 3.6	11.9 ± 2.4	54.4 ± 13.6	30.8 ± 7.7	16.0 ± 4.0

A shape comparison for both energies shows that the measured spectra are generally harder than those calculated as the basis of the Sauter cross section. However, the agreement is good with spectra calculated on the basis of the Schiff cross sections. This latter agreement might be due in part to the fact that in addition to utilizing the Schiff cross section the calculations took into account some scattering of the electrons in the target based on the code by Dickinson and Lent.[2] This seems reasonable in light of the fact that the thin targets utilized in the present experiment fall into the intermediate target group in the classification scheme given by Dickinson and Lent.[2] This group is characterized by plural scattering of the electrons in the target. On the other hand, the spectra calculated with the Schiff cross section are inherently harder than those using the Sauter compilation as shown by Koch and Motz.[14]

Table 14 indicates a hardening of the spectra with increasing angle for the 8-MeV case. Shape comparison of the 4-MeV spectra reveals only a very slight hardening. These results contrast with those for the thick targets where the spectra grow softer with increasing angle. In the latter case, there is a high probability for electrons in the target to be inelastically scattered through some angle before they generate bremsstrahlung. The larger the angle the more energy the electron will have lost before emitting bremsstrahlung.

As shown in Tables 14 and 15 the values for the integrated measured and calculated energies agree within the error bars except for the 3^{o}, 8 MeV on Ag, and Au cases where the values based on the Sauter cross section are too low and at 0^{o}, 8 MeV on Au where the value based on the Schiff cross section is too low.

Considering only Coulomb forces and no screening the acceleration of the electron is proportional to the Z of the nucleus. The intensity and therefore the yield is proportional to the square of the acceleration and thus to Z^2. This ratio should equal 2.83 when comparing Au and Ag. The

ratios of corresponding measured yields for Au and Ag are all equal, within systematic uncertainties, to a constant value of 2.2, independent of energy or angle. One would expect the measured ratios to be lower than 2.83 since the targets were thick enough to cause plural scattering of the electrons before emission of radiation, as mentioned above.

4. AN EMPIRICALLY DERIVED ELECTRON ENERGY AND ANGULAR DISTRIBUTION FORMULA

As has been pointed out in Section 1 several calculational techniques which are referenced to basic cross section data have been tried and proved successful in treating the electron transport problem for thick materials. Monte Carlo techniques employed by ETRAN 15,[1] as an example, have proved very successful, as shown by the comparisons with experimental data in this report. However, these calculations have not been made for a wide range of materials, energies, and thicknesses, and the codes developed to perform the calculations are not generally available; even if they were, they are expensive to run. Many situations do not warrant the accuracy nor the expense associated with the Monte Carlo calculations but require accuracies better than, for example, a factor of 2. Since a great deal of data has been acquired in this program it would seem reasonable to abstract this data in the form of a formula which should prove useful at least for the many situations that do not warrant a high degree of accuracy. The approach taken here is to derive a formula which yields the distribution in energy and angle for electrons emerging from a slab of material upon which a beam of monoenergetic electrons of a specified energy is incident normal to the slab's surface. A reasonable assumption as to the form of this distribution function is that it can be expressed as the product of three functions.

$$F(E_o, E, Z, t, \theta) = f(t, E_o, Z) \cdot Y(t, E_o, Z, E) \cdot \Phi(t, E_o, Z, \theta) \quad , \quad (22)$$

where E_o is the incident electron energy, E the exit energy, t the slab thickness, Z the atomic number of the target material, and θ is the angle measured with respect to the beam axis. The function $f(t, E_o, Z)$ is the

fraction transmitted through a slab of thickness t. Recently Ebert, et al., have made transmission measurements for various target materials in the energy range of 4 to 12 MeV.[9] They fit their transmission data with the following expression:

$$f(t, E_o, Z) = \exp\left[-\left(\frac{At}{Rex}\right)^B\right] , \tag{23}$$

where

$$B = \left\{\frac{837\ E_o}{Z\left[1 + 0.000075\ ZE_o^{\ 2}\right]}\right\}^{\frac{1}{4}} \tag{24}$$

$$A = \left(1 - \frac{1}{B}\right)^{\left(\frac{1}{B} - 1\right)}$$

$$Rex = 0.565\left(\frac{125}{Z+112}\right) E_o - 0.423\left(\frac{175}{Z+162}\right) .$$

In the above, Rex is the extrapolated range and is given in units of (g/cm^2).

The function, $Y(t, E_o, Z, E)$, gives the energy distribution of the exiting electrons. In Section 3.1 it is evident that the Landau function gives an excellent fit to the shape of the energy distributions. The fits to the data shape were obtained by adjusting only two parameters, E_{mp} and S_w in the following approximation to the Landau function.

$$Y = \sum_{k=1}^{4} C_k \exp\left[\frac{\frac{1.4}{S_w}\left(\frac{E}{E_o} - E_{mp}\right) + \lambda_k}{\gamma_k}\right] \tag{25}$$

where the values of the constants are given in Table 3. Data from the earlier work in this program on Be, Al, and Au, as well as the present

work on Sn, has permitted the formulation of the following expressions for S_w and E_{mp}.

$$E_{mp} = 1 - t/R_o \ , \tag{26}$$

where R_o is the range of an electron calculated by the continuous slowing down approximation (c. s. d. a.). A useful expression for R_o has been found from the calculations of Berger and Seltzer.[4]

$$R_o(E_o, Z) = E_o\left(\frac{0.3A}{Z} - \frac{E_o - 4}{250}\left[1 + \left(\frac{Z}{10} - 1\right) - 0.06\left(\frac{Z}{10} - 1\right)\left(\frac{Z}{10} - 5\right)\right]\right) (g/cm^2) \tag{27}$$

where A is the gram-molecular-weight of the material. This expression for R_o is valid between 1 to 10 MeV with a 5 percent accuracy. The parameter S_w is given by

$$S_w = 0.033\sqrt{Z}\ t/R_o \tag{28}$$

The data shows a slight angular dependence of both E_{mp} and S_w; however, for simplicity this angular dependence has been ignored.

The angular dependent term ϕ is given by the Gaussian approximation[2] for target thicknesses where the rms scattering angle is less than about 40 degrees.

$$\phi = \frac{1}{\theta_{rms}\sqrt{\pi}}\, e^{-\frac{\theta^2}{\theta^2_{rms}}} \tag{29}$$

Defining θ^2_{rms} as

$$\theta_{rms} = Ct^{\frac{1}{2}} * \frac{E_o}{M_o C^2} \cdot \frac{180}{\pi} \text{ (deg)}$$

$$C^2 = \frac{0.6014\ \rho\ Z(Z+1)(B-1.2)}{A\beta^4}$$

$$B = \text{greater solution of } \frac{e^B}{B} = \frac{\Omega_B}{1.167} \tag{30}$$

$$\Omega_B = \frac{7835\ \rho\ Z^{\frac{1}{3}}(Z+1)t}{A\beta^2(1+3.33\ \gamma^2)}$$

$$\gamma = \frac{Z}{137\beta} \quad ,$$

where ρ is the density of target material, $M_o C^2$ is rest mass energy of electron, and $\beta = \frac{V}{C}$ of incident electron.

As the electrons penetrate into the target this Gaussian distribution widens until eventually the angular distribution no longer continues to widen with increasing depth. For Sn as shown by our data this occurs for some thickness between 0.2 to 0.5 range (c.s.d.a.). For the 0.5 range and greater there appears to be no increase in the width of the angular distribution. At this point the angular distribution can be fit rather closely by a distribution calculated by Bethe, et al., [15] which is of the form $(0.717 + \cos\theta)\cos\theta$. When θ_{rms} becomes greater than 40^o then ϕ is taken as

$$\phi = (0.717 + \cos\theta)\cos\theta \tag{31}$$

5. ACKNOWLEDGEMENT

The authors wish to express their gratitude to J. H. Derrickson, Space Sciences Laboratory, Marshall Space Flight Center, for the ETRAN 15 computations which appear in this report.

REFERENCES

1. M. J. Berger and S. M. Seltzer, "Electron and Photon Transport Programs," Notes on Program ETRAN-15, NBS Report 9837 (1968).

2. W. C. Dickinson and E. M. Lent, "Calculations of Forward Bremsstrahlung Spectra from Thick Targets," UCRL-50442 (June 1968).

3. R. E. Sund, R. B. Walton, N. J. Norris and M. H. MacGregor, Nucl. Instr. Meth. 27, 104 (1964).

4. M. J. Berger and S. M. Seltzer, "Table of Energy Losses and Ranges of Electrons and Positrons," NASA SP-3012 (1964).

5. S. E. Chappell, J. C. Humphreys, J. W. Motz, M. J. Berger and S. M. Seltzer, "Response of Silicon Transmission Detectors to Monoenergetic Electrons," Proceedings of the Eleventh Scintillation and Semiconductor Counter Symposium, February 29, 1968.

6. J. A. Lonergan, C. P. Jupiter and G. Merkel, "Electron Energy Straggling Measurements for Thick Targets of Be, Al and Au at 4.0 and 8.0 MeV," (accepted for publication in Journal of Applied Physics).

7. V. V. Verbinski, R. E. Sund, "Measurement of Prompt Gamma Rays from Thermal-Neutron Fission of ^{235}U and ^{239}Pu and from Spontaneous Fission of ^{252}Cf," DASA Report GA-9148, Gulf General Atomic Incorporated, December 13, 1968.

8. P. J. Ebert, A. F. Lanzon and E. M. Lent, "Transmission and Backscattering of 4.0 to 12.0 MeV Electrons," UCRL-71-462 (1968).

9. P. J. Ebert, A. F. Lauzon, and E. M. Lent, Phys. Rev. 183, 422 (1969).

10. L. Landau, J. Phys. (USSR) 8, 201 (1944).

11. Blunck and S. Leisengang, Z. Physik, 128 500 (1950).

12. Carl Young, LASL (private communication) as exchanged in connection with a recent program (Ref. 7).

13. B. C. Cook, Nucl. Instr. Meth. 24, 256 (1963).

14. H. W. Koch and J. W. Motz, Rev. Mod. Phys. 31, 920 (1959).

15. H. A. Bethe, M. E. Rose, and L. P. Smith, Proc. Amer. Phil. Soc. 78, 573 (1938).